PhD Dissertation

Institute of Physical Chemistry of the Polish Academy of Sciences
ul. Kasprzaka 44/52, 01-224 Warsaw, Poland

Structure and NMR and UV Spectra of Strained Cyclophanes with Small Bridges

Taye Beyene Demissie

Supervisor: Prof. Dr hab. Helena Dodziuk

This PhD dissertation was prepared within the International Doctoral Studies at the Institute of Physical Chemistry of the Polish Academy of Sciences in Warsaw, Poland

Project operated within the Foundation for Polish Science International PhD Projects Programme co-financed by the European Regional Development Fund, Operational Program Innovative Economy 2007-2013.

INNOVATIVE ECONOMY
NATIONAL COHESION STRATEGY

FNP
Foundation for Polish Science

EUROPEAN UNION
EUROPEAN REGIONAL DEVELOPMENT FUND

Warsaw, October 2013

Acknowledgments

In the name of the Father, and of the Son, and of the Holy Spirit! Amen.

First of all, I cordially acknowledge the Foundation for Polish Science for providing the financial support and the Institute of Physical Chemistry for all facilities I received during my study. The Center for Theoretical and Computational Chemistry (CTCC), UiT - The Arctic University of Norway, is also greatly acknowledged for hosting me during my stay in the center. Next, I would like to thank my supervisor Prof. Dr hab. Helena Dodziuk (Institute of Physical Chemistry, Polish Academy of Sciences) for her guidance and help during the preparation of this work and for all the social activities. My sincere thanks also goes to Prof. Kenneth Ruud (CTCC, UiT - The Arctic University of Norway) who has been helping me in doing the research presented in this PhD dissertation, as well as for playing a profound role in my study.

I would also like to take the opportunity to acknowledge the support I got from Prof. Dr hab. Sławomir Szymański and Prof. Dr hab. Jarosław Jaźwiński (Institute of Organic chemistry, Polish Academy of Sciences) for the NMR measurements and discussion of the results obtained, Dr Volha Vetokhina (Institute of Physical Chemistry, Polish Academy of Sciences) for the absorption and emission measurements and Prof. Dr hab. Jacek Waluk (Institute of Physical Chemistry, PAS) for the discussion of the absorption and emission results. The support from Prof. Henning Hopf (Institute of Organic Chemistry, Braunschweig University of Technology, Germany) in providing the reagents used in this work is also greatly appreciated.

Furthermore, I would specially like to thank Dr. Johan Isaksson and Prof. Annette Bayer (Department of Chemistry, UiT - The Arctic University of Norway) for allowing me to work with their research groups while I was in Tromsø. It was really great experience in further extending my knowledge in physical-organic chemistry. The support I got from Michal Repisky and Stanislav Komorovsky (CTCC, UiT - The Arctic University of Norway) were also great. Sincere thanks to all the CTCC members in Tromsø, especially Magnus Ringholm, for all social activities we had. The computer time grants I received from Warsaw University (ICM, G28-7) and NOTUR (grant no. nn4654k) through computer clusters at UiT - The Arctic University of Norway (*Stallo*), the University of Oslo (*Abel*), and Iceland (*Gardar*) are greatly acknowledged. Finally, heartfelt thanks to all my families, friends and colleagues for being good all the times.

Taye Beyene Demissie

To my father: በየነ ደምሴ ዳዲ

Abstract

The objectives of this PhD dissertation were (a) analysing the structures of different kinds of cyclophanes using density functional theory (DFT) and comparing with available experimental results, aiming for the understanding of the structural phenomena as well as determining the missing structural parameters for the known and hypothetical molecules, (b) carrying out DFT calculations of the NMR spectral parameters and comparing them with the literature and measured experimental results, and (c) calculating the absorption and emission wavelengths of the [*m.n*]paracyclophanes, with *m*, *n* = 2 – 4. It should be stressed that the calculations have been preceded by the measurement of NMR spectra and UV/Vis and emission spectra performed in the Institute of Organic Chemistry and Institute of Physical Chemistry, respectively. To achieve these objectives, the molecules considered were divided in to three sets.

The studies conducted on the first set of molecules, [2.2]paracyclophane and its derivatives, show that the B3LYP functional is not well suited for the geometry optimization of the paracyclophanes studied. The calculated NMR parameters were compared with the experimental values. The results of the calculations involving only protons were compared with very accurate chemical shifts and $^{2}J_{HH}$ and $^{3}J_{HH}$ coupling constants determined in IChO PAN and IChF PAN. The theoretical vicinal J_{HH} coupling constants in the aliphatic bridges using 6-311G(d,p), cc-pVTZ, or Huz-IV basis sets reproduce the experimental values with an approximate rms error of about 1.3 Hz, regardless of the basis set used.

The optimized geometries of the second set of molecules, cyclophanes with ethylene bridges (cyclophenes), showed that only ωB97X-D/6-311++G(2d,2p) and ωB97X-D/cc-pVQZ yielded values of the $C_{sp^3}C_{sp^3}$ bond lengths close to the experimental data. ωB97X-D provides better results for bond lengths but the $C_{sp^2}C_{sp^3}C_{sp^3}C_{sp^2}$ torsional angles are not satisfactorily reproduced. Contrary to the calculations of geometries, an agreement between the values of the NMR parameters obtained using ωB97X-D/cc-pVQZ and the experimental ones is the poorest. Taking into account that most of the results of the different calculations show the same qualitative trends, the structural and NMR properties of the hypothetical cyclophenes are assumed to be correctly represented by the calculated values.

For the third set of molecules [*m.n*]paracyclophanes, *m*, *n* = 2 – 4, the DFT calculations satisfactorily reproduced the experimental chemical shifts, coupling constants, and absorption and emission wavelengths. Inclusion of dispersion and long-range corrections to the functionals

improves the geometry optimizations, except for the $C_{sp2}C_{sp3}C_{sp3}C_{sp2}$ torsional angle of [2.2]paracyclophane. Also in this case, the results of the calculations of involving only protons were compared with very accurate chemical shifts and $^{2}J_{HH}$ and $^{3}J_{HH}$ coupling constants values determined in IChO PAN and IChF PAN.

Streszczenie

Celem niniejszej pracy była

(a) analiza struktury szeregu cyklofanów z wykorzystaniem teorii funkcjonałów gęstości (DFT) oraz porównanie uzyskanych wyników z dostępnymi danymi doświadczalnymi, w celu zrozumienia czynników wpływających na budowę tych cząsteczek oraz ich właściwości, jak również określenie brakujących parametrów strukturalnych dla znanych i hipotetycznych cząsteczek,

(b) przeprowadzenie obliczeń DFT parametrów spektralnych NMR i porównanie ich z istniejącymi wynikami doświadczalnymi, oraz

(c) obliczenie poziomów elektronowych [*n,m*]paracyklofanów z *m*, *n* = 2 - 4. Należy podkreślić, że obliczenia zostały poprzedzone pomiarami widm NMR i UV/vis oraz widm emisyjnych wykonanych w Instytucie Chemii Fizycznej PAN i Instytucie Chemii Organicznej. Aby osiągnąć te cele zbadano trzy grupy cząsteczek.

Badania pierwszej grupy związków, [2,2]paracyklofanu i jego pochodnych, pokazały, że funkcjonał B3LYP niezbyt nadaje się do optymalizacji geometrii badanych związków. Wyniki obliczeń parametrów NMR porównano z dostępnymi danymi doświadczalnymi. Należy podkreślić, że wyniki obliczeń dotyczące jedynie protonów można porównać z bardzo dokładnymi wartościami przesunięć chemicznych i stałych sprzężenia, które zostały zmierzone w IChO PAN i IChF PAN. Wartości teoretyczne wicynalnych stałych sprzężenia w mostkach alifatycznych obliczone dla funkcji baz 6-311G(d,p), cc-pVTZ lub HUZ-IV dobrze zgadzają się z wartościami doświadczalnymi z przybliżonym błędem rms ok. 1,3 Hz, niezależnie od stosowanych funkcji.

Obliczenia optymalnej geometrii dla drugiego zestawu cząsteczek - cyklofanów z mostkiem etylenowym (cyklofenów) - wykazały, że tylko stosując metody ωB97X-D/6-311++G(2d,2p) i ωB97X-D/cc-pVQZ uzyskano wartości długości wiązań $C_{sp3}C_{sp3}$ bliskie danym eksperymentalnym. Funkcjonał ωB97X-D daje lepsze wyniki dla długości wiązań, ale obliczone wartości kątów torsyjnych $C_{sp2}C_{sp3}C_{sp3}C_{sp2}$ nie są zadowalające. W przeciwieństwie do wyników obliczeń geometrii, najgorszą zgodność pomiędzy obliczonymi i doświadczalnymi wartościami parametrów NMR uzyskano stosując metodę ωB97X-D/cc-pVQZ. Biorąc pod uwagę, że stosując różne metody uzyskuje się takie same jakościowe trendy strukturalne i właściwości

NMR hipotetycznych cyklofenów, przyjęto, że obliczone wartości właściwie opisują te parametry dla hipotetycznych układów.

Dla trzeciego zestawu cząsteczek, [*m,n*]paracyklofanów z *m*, *n* = 2 - 4 obliczono wartości przesunięć chemicznych i stałych sprzężenia. Obliczenia DFT w zadowalający sposób odtwarzają eksperymentalne trendy parametrów geometrycznych i widm NMR oraz długości fal absorpcji i emisji. Uwzględnienie korekty dyspersji funkcjonałów poprawia optymalizację geometrii, z wyjątkiem kąta skręcenia $C_{sp2}C_{sp3}C_{sp3}C_{sp2}$ [2,2]paracyklofanu.

List of Publications

Related to the PhD Dissertation:

1. H. Dodziuk, T. B. Demissie, J. Jaźwiński, S. Szymański, M. Pietrzak, V. Vetokhina, H. Hopf, J. Waluk, K. Ruud, *Structure, NMR and Electronic Spectra of [m.n]Paracyclophanes with Varying Bridges Lengths (m, n = 2 – 4)*, *in preparation*, **2013**.
2. S. Szymański, H. Dodziuk, M. Pietrzak, J. Jaźwiński, T. B. Demissie and H. Hopf, *Dynamics of [n.3]paracyclophanes (n = 2– 4) as studied by NMR. Obtaining separate Arrhenius parameters for two dynamic processes in [4.3]paracyclophane*, *J. Phys. Org. Chem.* **2013**, 26, 596-600. (IF = 1.96)
3. H. Dodziuk, T. B. Demissie, K. Ruud, S. Szymański, J. Jaźwiński, and H. Hopf, *Structure and NMR spectra of cyclophanes with unsaturated bridges (cyclophenes), Magn. Reson. Chem.* **2012**, 50: 449–457. (IF = 1.44)
4. H. Dodziuk, S. Szymański, J. Jaźwiński, M. Ostrowski, T. B. Demissie, K. Ruud, P. Kuś, H. Hopf, and S.-T. Lin, *Structure and NMR Spectra of Some [2.2]Paracyclophanes. The Dilemma of [2.2]Paracyclophane Symmetry*, *J. Phys. Chem. A* **2011**, 115, 10638–10649. (IF = 2.95)

Other:

1. T. B. Demissie, M. Repisky, H. Liu, K. Ruud and P. M. Kozlowski, *Ground-State Spin Properties of Cob(II)alamin Complexes: Relativistic DFT Analysis of EPR Parameters*, *J. Chem. Theor. Comp., submitted,* **2013**.
2. T. B. Demissie, M. Repisky, S. Komorovsky, J. Isaksson, J.-. Svendsen, H. Dodziuk and K. Ruud, *Four-component relativistic chemical shift calculations of halogenated organic compounds, J. Phys. Org. Chem*. **2013**, 679–687. (IF = 1.96)
3. E. Malkin, S. Komorovsky, M. Repisky, T. B. Demissie, K. Ruud, *The Absolute Shielding Constants of Heavy Nuclei: Resolving the Enigma of the ^{119}Sn Absolute Shielding, J. Phys. Chem. Lett.* **2013**, 4 (3), 459–463. (IF = 6.21)
4. K. Ø. Hanssen, B. Schuler, A. J. Williams, T. B. Demissie, E. Hansen, J. H. Andersen, J. Svenson, K. Blinov, M. Repisky, F. Mohn, G. Meyer, J.-S. Svendsen, K. Ruud, M. Elyashberg, L. Gross, M.l Jaspars, J. Isaksson, *A Combined Atomic Force Microscopy and Computational Approach for the Structural Elucidation of Breitfussin A and B: Highly Modified Halogenated Dipeptides from Thuiaria breitfussi*, *Angew. Chem. Int. Ed*. **2012**, 51, 12238 –12241. (IF = 13.45)

Conferences and Presentations

Oral Presentations:

1. T. B. Demissie, H. Dodziuk, S. Szymański, J. Jaźwiński, K. Ruud, and H. Hopf, *Dynamic NMR Spectra and Accurate Chemical Shifts and Coupling Constants of [3.n]Paracyclophanes, n = 2 - 4*, Third International Symposium on Computational Sciences (ISCS2013), November 18 - 20, **2013**, Shanghai, China.
2. T. B. Demissie, M. Repisky and K. Ruud, *Four-component relativistic chemical shift calculations for the structural determination of Breitfussin A and B*, Annual Conference of the Computational Chemistry division of the Norwegian Chemical Society, Hamn in Senja, Norway, June 12 - 13, **2012**.

Poster Presentations:

1. T. B. Demissie, M. Repisky, A. Ghosh and K. Ruud, *Relativistic Effects on the Structural Properties of Fe-, Ru- and Os-Porphyrin Complexes*, NOTUR2012 Conference, UiT - The Arctic University of Norway, June 14 - 15, **2012**.
2. H. Dodziuk, S. Szymański, T. B. Demissie, J. Jaźwiński and H. Hopf, *Dynamic Nuclear Magnetic Resonance Spectra and Accurate Chemical Shifts and Coupling Constants of [2.3]Paracyclophane*, VIth Symposium on: NUCLEAR MAGNETIC RESONANCE SPECTRA IN CHEMISTRY, PHYSICS AND BIOLOGICAL SCIENCES, Institute of Organic Chemistry, Polish Academy of Sciences, Warsaw, Poland, September 22 - 24, **2010**.

Table of Contents

Acknowledgments i
Abstract ii
Streszczenie iv
List of Publications vi
Conferences and Presentations vii
Table of Contents viii

Chapter 1. Introduction 1
1.1. Definition of Cyclophanes 1
1.2. The Beginning of Cyclophane Chemistry 2
1.3. Properties of Cyclophanes 3
1.4. Why are Cyclophanes Worth Studying Today? 6
1.5. The Major Objectives of the Dissertation 7
1.6. Outline of the Dissertation 8

Chapter 2. Quantum Chemical Calculations of NMR Parameters 11
2.1. Introduction 11
2.2. The NMR Spin Hamiltonian 12
2.3. Spin Hamiltonian Parameters as Energy Derivatives 14
2.4. The Molecular Electronic Hamiltonian 17
2.5. Interaction Terms 19

Chapter 3. Density Functional Theory Based Methods 25
3.1. Introduction 25
3.2. The Hohenberg-Kohn Theorem 26
3.3. The Kohn-Sham Equations 27
3.4. The Exchange-Correlation Energy Functional 28
3.4.1. The Local-Density Approximation 28
3.4.2. Generalized Gradient Approximations 28

3.4.3. Hybrid Functionals 29
3.5. Time-Dependent Density Functional Theory 30
3.6. Basis Sets 31

Chapter 4. Experimental and Computational Methods 33
4.1. Experimental 33
4.1.1. Reagents 33
4.1.2. NMR Measurements 33
4.1.3. Analysis of NMR Spectra 34
4.1.4. Absorption and Emission Spectra Measurements 34
4.2. Computational Details 35
4.2.1. Computational Details of [2.2]Paracyclophane **7** and Its Derivatives **17**-**19** 35
4.2.2. Computational Details of Cyclophanes with Unsaturated Bridge(s) **9**, **20**-**28** 35
4.2.3. Computational Details of [*m.n*]Paracyclophanes (*m, n* = 2–4) **7**, **15**, **16**, and **30**-**32** ...36

Chapter 5. [2.2]Paracyclophane and its Derivatives 37
5.1. Introduction 37
5.2. Geometry of [2.2]Paracyclophane **7** 41
5.3. Geometry of the Derivatives of [2.2]Paracyclophane 44
5.4. ^{1}H Chemical Shifts 49
5.5. ^{13}C Chemical Shifts 52
5.6. Comparison of the Calculated Chemical Shifts of Model Systems with 7 54
5.7. $^{2}J_{HH}$ and $^{3}J_{HH}$ Coupling Constants 56
5.8. Temperature Effects on the J_{HH} Coupling Constants of the Bridges 60
5.9. $^{1}J_{CH}$ and $^{1}J_{CC}$ Coupling Constants 61
5.10. Conclusion 65

Chapter 6. Cyclophanes with Unsaturated Bridges (Cyclophenes) 66
6.1. Introduction 66
6.2. Geometry of **7**, **9**, **20** and **21** 68
6.3. Geometry of **22** – **24** and **29** 71

6.4. Geometry of **25** – **28** 74
6.5. NMR Parameters of **7**, **9**, **20** and **21** 76
6.6. NMR Parameters of Molecules **22** – **24** and **29** 83
6.7. NMR Parameters of Molecules **25** – **28** 89
6.8. Conclusion 94

Chapter 7. [*m.n*]Paracyclophanes (*m*, *n* = 2 – 4) with Varying Lengths of the Bridges 95
7.1. Introduction 95
7.2. Symmetry, Torsional Angles of the Bridges and Conformations 98
7.3. Separation Distances between the Aromatic Rings 101
7.4. Bond Lengths and Angles 103
7.5. ^{1}H Chemical Shifts 103
7.6. ^{13}C Chemical Shifts 111
7.7. $^{n}J_{HH}$ Coupling Constants, n = 2 – 3 112
7.8. $^{n}J_{CH}$ Coupling Constants, n = 2 – 3 114
7.9. $^{n}J_{CC}$ Coupling Constants, n = 2 – 3 114
7.10. Absorption and Emission Spectra and Excited State Structures 115
7.10.1. Interring Separation, Ring Deformation and Twist Angle in the Excited State 115
7.10.2. Absorption Spectra 117
7.10.3. Emission Spectra 122
7.11. Conclusion 123

Chapter 8. Summary 125

References 128

Annex 136 (S1-S69)

Chapter 1
Introduction

1.1. Definition of Cyclophanes

Benzene and its aromatic derivatives are among the most important classes of compounds in the world of organic chemistry. Among these, cyclophanes are molecules formed from one aromatic part and a hydrocarbon chain connecting two carbon atoms of a ring **1** or from two or more aromatic rings connected by either saturated **2** or unsaturated chains **3**.[1-3] Atoms such as nitrogen and sulfur, in addition to the carbon and hydrogen atoms, may also be a part of a cyclophane system as is the case for heteraphanes **4a** with bridge heteroatom(s), heterophanes **4b** with ring heteroatom(s), and mixed hetero/heteraphanes **4c**. The word "phane" is used as the stem name for such ring compounds. Some representative structures are shown below, whereas the detailed classifications and definitions can be found in the monograph "*Modern Cyclophane Chemistry*" edited by R. Gleiter and H. Hopf.[2]

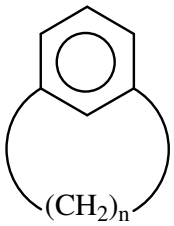

1

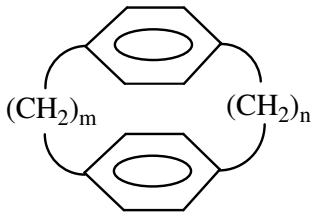

2

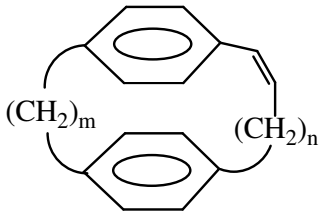

3

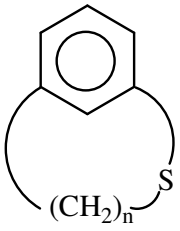

4a

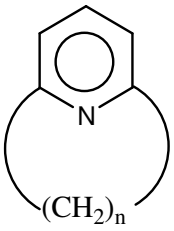

4b

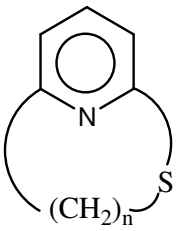

4c

1.2. The Beginning of Cyclophane Chemistry

Even though the actual structure was only realized more than 150 years after its discovery,[4,5] the first cyclophane prepared was [1.1.1]orthocyclophane **5** by Cannizzaro in 1854.[6] Pellegrin reported the synthesis of *trans*-[2.2]metacyclophane **6** in 1899.[7] In 1949 Brown and Farthing reported in a short communication the synthesis of [2.2]paracyclophane **7** from *para*-xylene **8** and its X-ray structural analysis.[8] Two years later Cram and Steinberg synthesized and reported the same cyclophane along with its higher homologues, [*m.n*]paracyclophanes **2**, which opened the era of cyclophane chemistry.[1] In addition to the molecules with saturated bridges, cyclophanes with unsaturated bridges, for example **9**, were also prepared.[1] Later on, numerous other cyclophanes have been synthesized. The most interesting of these was superphane **10** (first synthesized by Boekelheide in 1979)[9] which has six ethylene bridges connecting the two benzene rings.

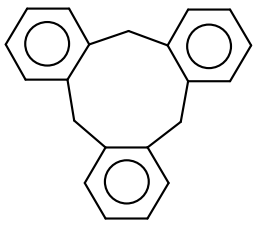

5

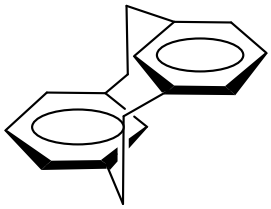

6

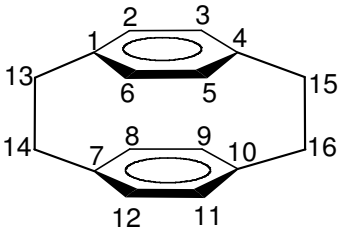

7

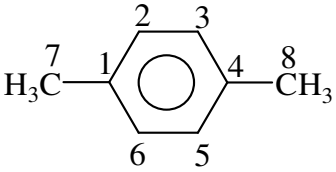

8

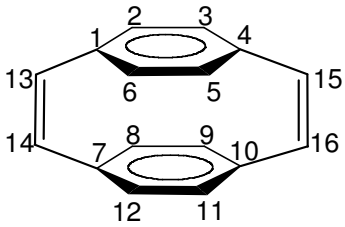

9

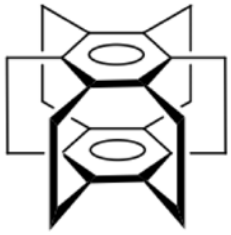

10

1.3. Properties of Cyclophanes

D. J. Cram[1] began his studies of [*m.n*]paracyclophanes, with *m, n* = 2, 3 because of the close distance between the π-electron clouds in molecules with small bridges. In these molecules, the aromatic rings are nonplanar and aromatic hydrogen atoms lie significantly out of the plane of the C1, C2, C3 and C4 carbon atoms of one benzene ring, bent toward the other benzene ring. These deformations from the ideal benzene geometry reflect the strong π-π electron repulsions between the two benzene rings resulting in an increased π-electron density on the outside faces of the rings. Such unusual structures departing from that in benzene are worth studying.

Substitution of hydrogen atoms of benzene by other substituents such as alkyl (for example dialkylbenzene **11**) leads to negligible changes to its ring planarity. Similarly, connecting two carbon atoms of a ring by a long alkyl chain (for example in [10]paracyclophane **12**) has also negligible effect on the ring planarity. However, shortening of the chain connecting two carbon atoms of a ring (for example in [8]paracyclophane **13**[10]) results in a nonplanar deformation of the ring. Similarly, in [6.6]paracyclophane **14** the rings are nearly planar,[11] whereas in **7** they are considerably deformed from planarity. For example, C1 and C4 of **7** are bent out of the plane of C2, C3, C5 and C6 toward the second ring by about 0.168 Å (14°) at 291 K.[12,13] In general, for paracyclophanes with shorter aliphatic chains, the aromatic rings are considerably deformed from planarity compared to the standard aromatic molecules making them interesting with respect to their structures and the influence of their nonplanar distortions on the properties of the cyclophanes.[2,3,14-20]

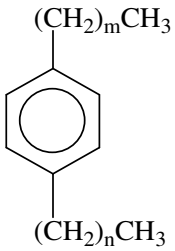

11

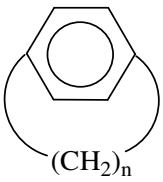

12, n = 10
13, n = 8

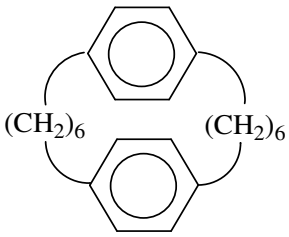

14

In a review paper by D. J. Cram and J. M. Cram[1] it was noted that the most important structural features of **7**, which also correlate with its unusual physical and chemical properties, are the stretched $C_{sp3}C_{sp3}$ bonds, the bent benzene rings, the abnormal bond angles, and in

particular the small distance between the two benzene rings. The shortest distance between the two benzene rings (C1…C7 and C4…C10) of **7** is 2.780 Å, which is not only considerably less than the separation distance between the stacked aromatic molecules but also less than the sum of two carbon atoms van der Waals radii, *ca*. 3.4 Å. Moreover, the distance between the corresponding carbon atoms of the two aromatic rings in **10** (2.620 Å)[9] is considerably shorter than that in **7**. Its $C_{sp2}C_{sp3}$ bonds are out of the planes of the aromatic rings by *ca*. 20°. The data on the symmetry of **7** are equivocal; it is not clear whether the molecule has an eclipsed D_{2h} or twisted D_2 equilibrium geometry. In the latter case the mutual twist of the benzene rings is combined with a twist around the C13C14 and C15C16 bridges. The X-ray structure of **7** reported by Brown[21] in 1953 and by Lonsdale *et al.*[12] in 1960 resulted in the latter structure with disorder. However, the latest reported X-ray data (2003) by Lyssenko *et al*.[20] measured at 100 K unequivocally favor the former structure with no twist and no disorder. The origin for these very different X-ray results for [2.2]paracyclophanes are the very low energy difference between the two conformers (0.2 kcal/mol as calculated by Grimme[22]) and even smaller, quite unreliable, value in Ref. 30 and the significant temperature dependence of the structural parameters. For instance, the $C_{sp3}C_{sp3}$ bridge bond length was found to be longer than 1.558 Å at 93 K,[12] 1.579 Å at 100 K,[20] and 1.630 Å[12] and 1.569 Å at 297 K.[23]

Computational studies on the structure of **7** have also been reported. The discussion of the results obtained in several computational studies[14,22,24-28] is blurred by the fact that in 2004[22] Grimme cited results that todate remain unpublished by Stalke measured at 19 K obtained for a different crystal structure (present below 50 K[29]) than that studied by Lyssenko *et al*.[20] The Grimme paper is then cited by theoreticians as the experimental one.[14,28] Walden and Glatzhofer[30] reported a twist angle of 3.9° using the hybrid Hartree-Fock/gradient-corrected DFT B3LYP/4-21G(d) method, whereas Henseler and Hohlneicher[26,27] obtained 21.8° using MP2/6-31G(d). Bachrach[14] also reported varying twist angles based on the functional applied; 18.5° using M06-2X, 9.9° using B97-D, and 15.4° using ωB97X-D. The results reported by Grimme[22] also showed that the calculated twist angle of **7** is dependent on the type of functional used; where only the B3LYP functional results for the C1C13C14C7 twist angle of the D_{2h} structure agree with the latest experimental result reported by Lyssenko *et al.*[20] Details of these issues are presented in the introductory parts of Chapters 5 and 7.

In addition to several calculations on [2.2]paracyclophanes[14,22,25-28,30,31] briefly discussed above, a few calculations for the structure of other cylophanes have also been reported.[14,15,28,32,33] The proton and carbon chemical shifts in **7** were calculated by Caramori *et al*.,[24] while Bifulco and Mangoni[34] analyzed ^{1}H-^{1}H scalar couplings across the two stacked aromatic rings in derivatives of **7**. A combined experimental and theoretical NMR study of **15** was also reported by Dodziuk *et al*.[15] Studies about the absorption of **7** have also been reported. Among these, Canuto and Zerner[35] analyzed the inter-ring separation of the lowest excited and ionized states of **7** on the basis of SCF (STO-3G) calculations. Shen and co-authors[36] studied the fluorescence excitation spectra of **7** in supersonic jets and carried out calculations allowing them to explain the extensive vibronic structure in the lowest-lying electronic transitions. Shirai *et al*.[28] also reported the excited-state optimized structures of **7** and **15** obtained from time-dependent density functional theory (TD-DFT). A combined experimental and computational study of UV/Vis and magnetic circular dichroism (MCD) of **7** together with other cyclophanes with small bridges reported by Dodziuk *et al*.[37] is also among the recent studies.

In solution paracyclophanes with n > 2 exhibit conformational flexibility. For example, [3.3]paracyclophane **15** exists in solution as a mixture of *trans*-**15** and *cis*-**15**. The analysis of its NMR spectra by Dodziuk *et al*.[15] indicates a *cis*:*trans* conformations ratio of 2:1 with the Arrhenius parameters E_A = 12.29 kcal/mol and $k_{ba0} = 9.6 \times 10^{12}$ s^{-1} for the conversion of *cis*-**15** to *trans*-**15**.[15] Interestingly, although the former conformer is more stable in solution, **15** crystallizes in the *trans* conformation,[17] favored by the crystal packing forces. **14** is also so flexible that not only can the bridges have different conformations but also one of the aromatic moieties can rotate, resulting in more conformers.

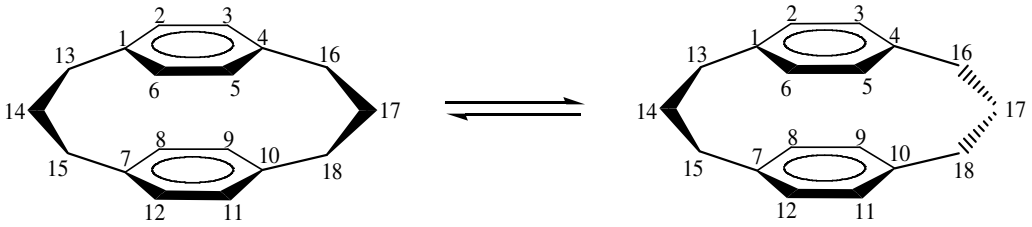

cis-**15** *trans*-**15**

The proximity of the rings and the structural abnormalities also change the spectroscopic parameters of the molecules. Among these, NMR chemical shifts and spin-spin coupling

constants as well as UV spectral parameters are very sensitive to the molecular structure. For instance, the complexes of **2** with tetracyanoethylene have different colors for different bridge lengths.[38] Depending on the *m*, *n* values, the complexes are yellow, purple, deep blue, orange and red for $m = n = 4$; $m = 3$, $n = 4$; $m = n = 3$; $m = 3$, $n = 2$ and $m = n = 2$, respectively. Another factor influencing the properties of [*m.n*]paracyclophanes for small $m \neq n$, which has not been studied in detail previously, is a nonparallel arrangement of the rings such as that in **16**.

Due to their interesting physical and chemical properties, cyclophanes have attracted the attention of both experimentalists and theoreticians. Detailed discussions of their interesting properties are included in the introductory parts of the chapters discussing the cyclophanes studied in this PhD dissertation.

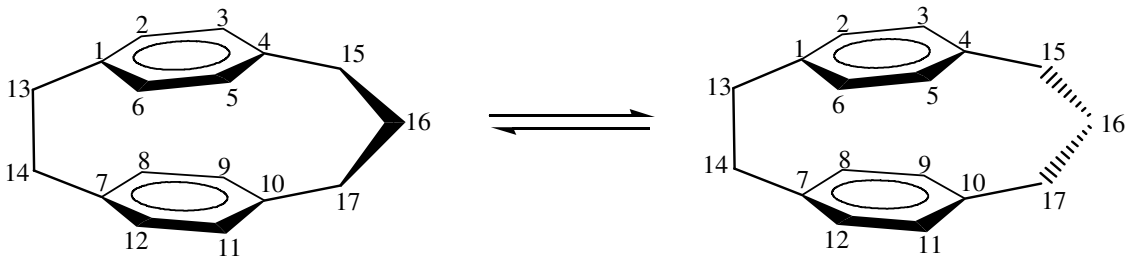

16a **16b**

1.4. Why are Cyclophanes Worth Studying Today?

Cyclophane chemistry is an old and well-established field. For more than sixty years, cyclophanes have been the subject of intense experimental and theoretical research.[39-43] The interest in their study is directly related to the close distance between the benzene rings which makes their π-electrons interact and causes the nonplanarity of the benzene ring(s) as discussed in the review paper by Cram and co-workers.[1] In addition; the structural, chemical and spectroscopic properties of the molecules as a consequence of the unusually deformed benzene ring(s) are also reasons for the broad interest in these compounds by researchers.[2] As already mentioned before, cyclophanes with nonplanar arrangement of benzene rings offer another possibility to study the interaction of their π-electron clouds, which has not been explored previously.

Nowadays, cyclophanes are used in materials and in several related areas such as asymmetric synthesis,[43] supramolecular chemistry,[44] polymer chemistry,[19,39,41,45,46] anti-bacterial efficacy,[47] inhibitors of HIV proteinase,[48] catalysis and sensors.[47-50] Due to these emerging prospective applications and their unusual structures, cyclophanes remain subjects of numerous studies.[4,14-16,28,37,46,51,52]

1.5. The Major Objectives of the Dissertation

The NMR measurements were carried out at the Institute of Organic Chemistry of the Polish Academy of Sciences by Prof. Dr hab. Sławomir Szymański, Prof. Dr hab. Jarosław Jaźwiński and by Dr Mariusz Pietrzak at the Institute of Physical Chemistry of the Polish Academy of Sciences. On the other hand, the UV/Vis experiments were carried out at the Institute of Physical Chemistry of the Polish Academy of Sciences in the group of Prof. Dr hab. Jacek Waluk. In addition to these experimental measurements, DFT calculations of NMR parameters were carried out within this PhD dissertation to achieve the following objectives:

1. Structural analysis

   As highlighted, cyclophanes with short bridges are structurally interesting due to their geometrical abnormalities. Comprehensive and detailed structural analysis of [*m.n*]paracyclophanes (*m*, *n* = 2 – 4) using density functional theory, DFT, combined with available experimental structures is rare and/or difficult to find in the literature. There are also open questions about the symmetry of **7**. Therefore, the first objective of this PhD dissertation was to study the geometry of [*m.n*]paracyclophanes (*m*, *n* = 2 – 4) as well as that of derivatives of **7** and its higher homologues with unsaturated bridges.

2. Variable temperature NMR studies

   Detailed NMR studies, especially calculated NMR parameters, of paracyclophanes with short bridges as well as of those with unsaturated bridges are also scarce in the literature.[15,51,53,54] Variable temperature NMR studies of cyclophanes, of which only one earlier study for **15** has previously been reported,[15] facilitate the understanding of the dynamic phenomena taking place in the bridges of paracyclophane. Hence, static and variable temperature NMR studies of [*m.n*]paracyclophanes with short bridges combined with DFT calculations was undertaken as the second major objective of the PhD study.

3. UV/Vis spectroscopic studies

   The UV/Vis study of [*m.n*]paracyclophanes (*m*, *n* = 2 – 4) using both experimental measurements and DFT calculations helps the understanding of the electronic interactions between the rings, manifested significantly by the different colors of their complexes with tetracyanoethylene[38] mentioned earlier, which therefore was set to be the third major objective of the PhD study.

4. Density functional theory (DFT) is a reliable standard tool for the theoretical treatment of the structures as well as NMR and UV/Vis absorption spectra of typical organic molecules. It simplifies the interpretation of the spectra and contributes to the understanding of the phenomena taking place during molecular motions. Here, cyclophanes with small bridges are used for testing the performance of different functionals when applied for the study of strained molecules with π-π electronic interactions. Therefore, analysis of the performance of some DFT methods for highly strained cyclophanes has been the fourth objective of this PhD dissertation.

1.6. Outline of the Dissertation

The dissertation is divided into eight chapters. In addition to Chapter 1 presenting introduction to the problems under study, Chapter 2 describes the quantum chemical treatment of NMR parameters. Chapter 3 briefly presents the density functional theory methods used in this PhD dissertation together with the calculations of electronic levels using time-dependent density functional theory allowing one to interpret UV/Vis spectra. Chapter 4 describes the experimental and computational methods applied in this PhD study. In Chapter 5, the results obtained for the structures, chemical shifts and spin-spin coupling constants of [2.2]paracyclophane **7** and its derivatives: phenyl-[2.2]paracyclophane **17**, benzene[2.2]paracyclophane **18**, and *trans*-[2.2]naphthalenophane **19** are presented. Chapter 6 presents the results obtained for the structural parameters, chemical shifts and spin-spin coupling constants of cyclophanes with small bridges with unsaturated bridge(s): [2.2]paracyclophan-13-ene **20**, [2.2]paracyclophan-13,15-diene **9**, 13-vinyl-[2.2]paracyclophan-13-ene **21**, [2.2.2](1,2,4)-cyclophan-15-ene **22**, [2.2.2](1,2,4)-cyclophan-17-ene **23**, [2.2.2](1,2,4)cyclophan-13-ene **24**, [2.2.2](1,2,4)cyclophan-13,15-diene **25**, [2.2.2](1,2,4)cyclophan-13,17-diene **26**, [2.2.2](1,2,4)cyclophan-15,17-diene **27**,

[2.2.2](1,2,4)cyclophan-13,15,17-triene **28**, and of the results for [2.2]paracyclophane **7** and [2.2.2](1,2,4)cyclophane **29** added for the sake of comparison. Chapter 7 describes the results obtained for the structural, NMR and UV/Vis spectroscopic studies of [*m.n*]paracyclophanes (*m*, *n* = 2 – 4) with varying lengths of the bridges: [2.2]paracyclophane **7**, [2.3]paracyclophane **16**, [2.4]paracyclophane **30**, [3.3]paracyclophane **15**, [3.4]paracyclophane **31**, and [4.4]paracyclophane **32**. Finally, Chapter 8 presents the summary and general conclusions of the findings in the study.

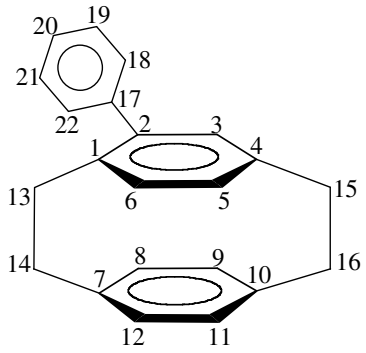

17

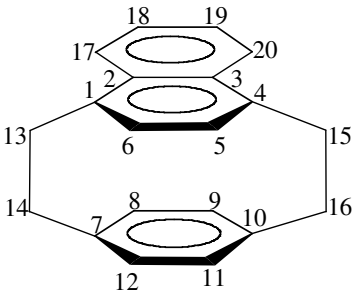

18

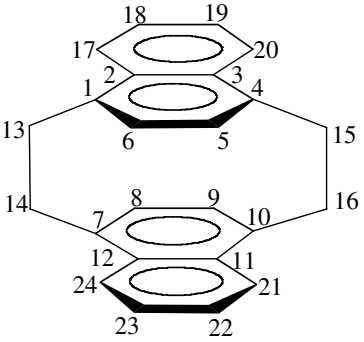

19

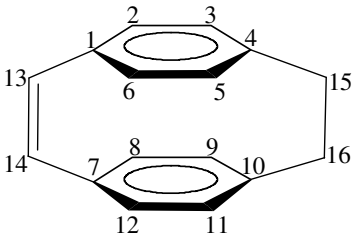

20

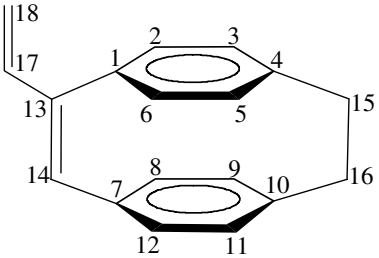

21

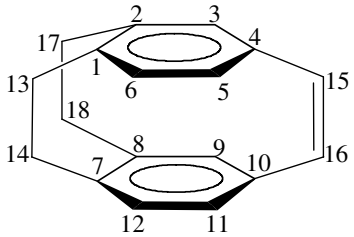

22

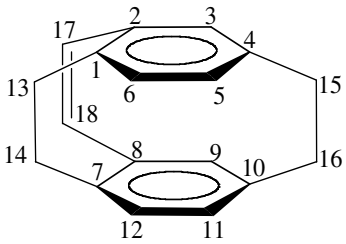

23

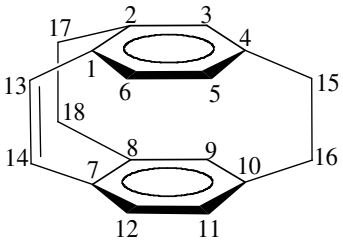

24

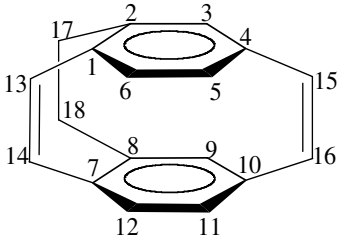

25

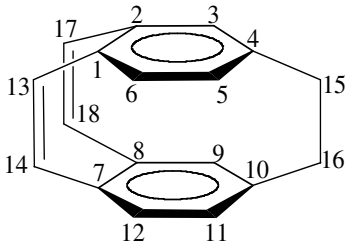

26

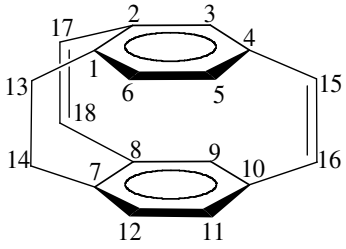

27

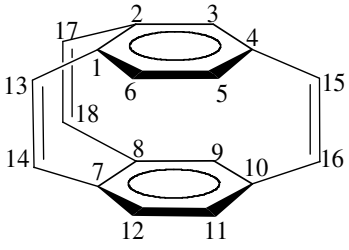

28

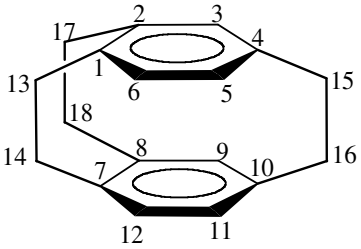

29

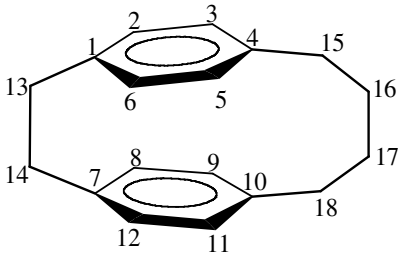

30

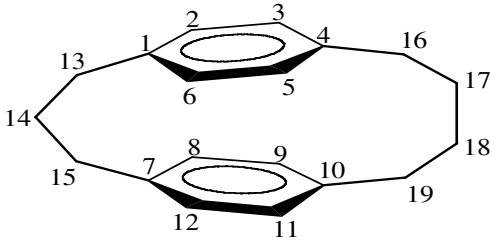

31

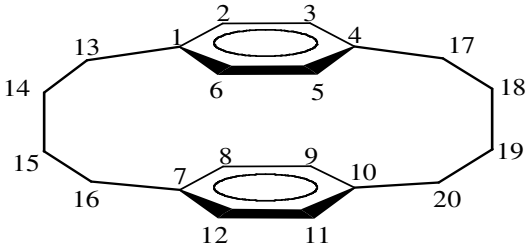

32

Chapter 2
Quantum Chemical Calculations of NMR Parameters

2.1. Introduction

Nuclear magnetic resonance (NMR) spectroscopy is the most commonly used technique to study the interaction of nuclei with electromagnetic radiation. It provides detailed information about the structure and properties of atoms or the molecules in which they are contained. The external applied magnetic field influences the electron density, decreasing or increasing the magnetic field experienced by a nucleus, which is known as shielding or deshielding of the nucleus. In practice, this measurement is reported as the chemical shift, which is the resonance frequency of a nucleus relative to a standard. For instance, tetramethylsilane (TMS) is used as a standard for ^{1}H and ^{13}C. The magnetic interactions between non-equivalent NMR-active nuclei, called spin-spin coupling, is another property of nuclei in the molecule. The interactions occurring when a molecular system is placed in an external magnetic field are schematically shown in Fig. 1, presenting the shielding of a nucleus and the electron-density-mediated spin-spin coupling of two nuclei. The quantum-chemical treatments of these two NMR parameters are discussed in the following sections.

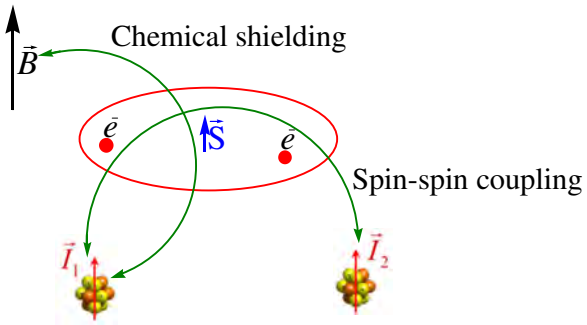

Fig. 1. Schematic representation of the phenomena taking place in NMR spectroscopy: chemical shielding and spin-spin coupling. Adapted from the courtesy of S. Komorovsky of CTCC, UiT - The Arctic University of Norway

2.2. The NMR Spin Hamiltonian

The nuclear spin operator, I_K, and the nuclear magnetic dipole moment, μ_K, are related through the equation:

$$\mu_K = \gamma_K \hbar I_K \quad \text{.....(1)}$$

where γ_K is the magnetogyric ratio, a constant characteristic of the particular nucleus of interest and *h* is Plank's constant. If the nucleus is placed in a magnetic field, the spin of an NMR active nucleus will be quantized with a small number of allowed orientations with respect to the applied magnetic field. Hence, the energy of the particular energy level (during the interaction of the nucleus with a magnetic field) is given by

$$E = -\mu_K.B = -\gamma_K \hbar I_K B \quad \text{.....(2)}$$

where *B* is the strength of the magnetic field at the nucleus. All isotopes which contain an odd number of protons and/or of neutrons have an intrinsic magnetic moment and angular momentum, in other words a nonzero spin which makes them NMR active. On the other hand, all other nuclei with even numbers of both protons and neutrons have a total spin of zero and they are NMR inactive. Hence, the most commonly studied nuclei in organic chemistry are those of ^{1}H and ^{13}C with the spin equal to 1/2. Therefore, the difference between their energy levels (the transition energy) can be obtained from:

$$\Delta E = \gamma_K \hbar B \quad \text{.....(3)}$$

In molecules, the electrons surrounding the nuclei modify the interaction of the magnetic moment of an NMR active nucleus with the applied magnetic field.[2,55] In experiment, these interactions are interpreted in terms of an effective NMR spin-Hamiltonian; the electrons do not appear explicitly and the nuclei are represented by their intrinsic spins and the associated magnetic moments. Hence, the total effective NMR spin-Hamiltonian is given by[55]

$$\hat{H}^{NMR} = -\sum_K \vec{B}^T(\vec{1}-\vec{\sigma}_K)\hbar\gamma_K\vec{I}_K + \frac{1}{2}\sum_{K\neq L}\hbar\gamma_K\vec{I}_K^T(\vec{D}_{KL} + \vec{K}_{KL})\hbar\gamma_L\vec{I}_L \quad (4)$$

where B is the applied external magnetic field, σ_K are the nuclear magnetic shielding tensors of nucleus K, D_{KL} are the classical dipolar interactions which describe the direct couplings of the nuclear magnetic dipole moments through space, K_{KL} is the reduced indirect nuclear spin-spin coupling tensor which describes the indirect couplings of the nuclear dipoles mediated by the surrounding electrons. For isotropic samples, the direct spin-spin coupling constants D_{KL} vanish, whereas the indirect coupling constants remain. Then, for a rotating molecule in an isotropic medium, the NMR spin-Hamiltonian simplifies to

$$\hat{H}_{iso}^{NMR} = -\sum_K \vec{B}^T(\vec{1}-\vec{\sigma}_K)\vec{\mu}_K + \frac{1}{2}\sum_{K\neq L}\vec{\mu}_K\vec{K}_{KL}\vec{\mu}_L \quad (5)$$

This spin Hamiltonian contains all the information needed for the representation of a high-resolution NMR spectrum.[55,56] The isotropic shielding constant and the reduced indirect nuclear spin-spin coupling constant are then expressed as traces of the corresponding tensors:

$$\sigma_K = \frac{1}{3}\{\sigma_{K,xx} + \sigma_{K,yy} + \sigma_{K,zz}\} \quad (6)$$

$$K_{KL} = \frac{1}{3}\{K_{KL,xx} + K_{KL,yy} + K_{KL,zz}\} \quad (7)$$

However, the NMR spin-Hamiltonian is usually expressed not in terms of the reduced indirect spin-spin coupling tensors K_{KL}, which are independent of the nuclear magnetogyric ratios, but rather in terms of the indirect spin-spin coupling tensors J_{KL}. The indirect spin-spin coupling constant is the most commonly used term and is related to the reduced indirect spin-spin coupling constant by

$$J_{KL} = h\frac{\gamma_K}{2\pi}\frac{\gamma_L}{2\pi}K_{KL} \quad \text{.....(8)}$$

In practice, chemical shifts are measured from the NMR spectra of the molecules relative to a standard, which is defined as the difference between the shielding constant of nucleus *K* of interest and the nucleus of a standard reference molecule,

$$\delta_K = \sigma_K^{ref} - \sigma_K \quad \text{.....(9)}$$

2.3. Spin-Hamiltonian Parameters as Energy Derivatives

The NMR parameters can be expressed using perturbation theory. If a perturbation x modifies the molecular electronic system, then the total molecular energy can be expressed as[55,57]

$$E(x) = E^{(0)} + E^{(1)}x + \frac{1}{2}x^T E^{(2)}x + \ldots \quad \text{.....(10)}$$

assuming a small perturbation x. The coefficients of this energy expansion are characteristics of the molecular system and are called molecular properties. For time-independent static perturbations, these molecular properties can be calculated as energy derivatives:

$$E^{(1)} = \left.\frac{\partial E}{\partial x}\right|_{x=0}, \quad E^{(2)} = \left.\frac{\partial^2 E}{\partial x^2}\right|_{x=0} \quad \text{.....(11)}$$

In the case of an unperturbed system, the electronic energy is given as $E(x) = \langle O | H | O \rangle$. In non-degenerate time-independent perturbation theory[58,59] the first- and second-order molecular properties are expressed by the following equations, where the derivatives are taken at $x = 0$:

$$\frac{\partial E(x)}{\partial x_i} = \left\langle 0 \left| \frac{\partial H}{\partial x_i} \right| 0 \right\rangle \quad \text{.....(12)}$$

where the first-order property is the expectation value of the first-order Hamiltonian (the Hellmann-Feynman theorem). For the second-order molecular property:

$$\frac{\partial^2 E(x)}{\partial x_i \partial x_j} = \left\langle 0 \left| \frac{\partial^2 H}{\partial x_i \partial x_j} \right| 0 \right\rangle - 2\sum \frac{\left\langle 0 \left| \frac{\partial H}{\partial x_i} \right| n \right\rangle \left\langle n \left| \frac{\partial H}{\partial x_j} \right| 0 \right\rangle}{E_n - E_0} \quad \text{.....(13)}$$

which also contains a sum-over-states term having contributions from each excited state. For magnetic properties, the expectation-value contribution to the second-order property is known as the diamagnetic part and the sum-over-states contribution is referred to as the paramagnetic part.[55,57]

In the presence of an external magnetic field and nuclear magnetic moments, the electronic energy is represented as

$$E(B,\mu) = E_0 + E^{(10)}B + \sum_K E_K^{(01)}\mu_K + \frac{1}{2}B^T E^{(20)}B + \sum_K B^T E_K^{(11)}\mu_K + \frac{1}{2}\sum_{K\neq L}\mu_K^T E_{KL}^{(02)}\mu_L \quad \text{.....(14)}$$

The corresponding energy derivatives are then given as

$$E^{(10)} = \left.\frac{\partial E(\mu_K, B)}{\partial B}\right|_{\mu_{K=0}, B=0} \quad \text{.....(15)}$$

$$E_K^{(01)} = \left.\frac{\partial E(\mu_K, B)}{\partial \mu_K}\right|_{\mu_{K=0}, B=0} \quad \text{.....(16)}$$

$$E^{(20)} = \left.\frac{\partial^2 E(\mu_K, B)}{\partial B^2}\right|_{\mu_{K=0}, B=0} \quad \text{.....(17)}$$

$$E_K^{(11)} = \left.\frac{\partial^2 E(\mu_K, B)}{\partial B \partial \mu_K}\right|_{\mu_{K=0}, B=0} \quad \text{.....(18)}$$

$$E_{KL}^{(02)} = \left.\frac{\partial^2 E(\mu, B)}{\partial \mu_K \partial \mu_L}\right|_{\mu_{K=0}, \mu_{L=0}, B=0} \quad \text{.....(19)}$$

The two first-order terms vanish for closed-shell systems (*vide infra*), whereas those higher than second-order terms often are neglected due to the smallness of the perturbations. The comparison between the NMR spin-Hamiltonian given in equation (4) and the energy expressed in the presence of an external magnetic field and nuclear magnetic moments in equation (14) shows that the $E^{(11)}$ term is related to the nuclear shielding tensor and the $E^{(02)}$ term with the spin-spin coupling tensor:[55]

$$\sigma_K = \left.\frac{\partial^2 E(\mu_K, B)}{\partial \mu_K \partial B}\right|_{\mu_{K=0}, B=0} \quad \text{.....(20)}$$

When the direct Zeeman interaction between the nucleus and the magnetic field is added, the shielding tensor can be written as

$$\left.\frac{\partial^2 E(\mu_K, B)}{\partial \mu_K \partial B}\right|_{\mu_{K=0}, B=0} = \sigma_K - 1 \quad \text{.....(21)}$$

The reduced indirect spin-spin coupling constant of nuclei *K* and *L* can be written as the second derivative of the total electronic energy of the molecular system with respect to the magnetic moments of nuclei *K* and *L*:[55,57]

$$K_{KL} = \left.\frac{\partial^2 E(\mu_K,\mu_L)}{\partial\mu_K\partial\mu_L}\right|_{M_K=0,M_L=0} \quad \text{.....(22)}$$

2.4. The Molecular Electronic Hamiltonian

The determination of the dependence of the electronic Hamiltonian on the magnetic induction *B* and the nuclear magnetic moments, μ_K, is important in order to arrive at the explicit expressions for the nuclear shielding and spin-spin coupling constants.[55] The perturbations that in this case interact with the electrons arise from: (a) the orbital motion of the electrons and (b) the permanent magnetic moments of the electrons

$$\mu_i = -g\mu_B s_i = -s_i \quad \text{.....(23)}$$

where the electron g-factor is equal to 2.0023 and the Bohr magneton (in atomic units) is defined by

$$\mu_B = \frac{e\hbar}{2m_e} = \frac{1}{2} \quad \text{.....(24)}$$

In the presence of these magnetic perturbations, the non-relativistic molecular electronic Hamiltonian may be written in atomic units as[55]

$$\hat{H}(B,\mu) = \frac{1}{2}\sum_i \pi_i^2 - \sum_i \mu_i.B^{tot}(r_i) - \sum_{iK}\frac{Z_K}{r_{iK}} + \frac{1}{2}\sum_{i\neq j}\frac{1}{r_{ij}} + \frac{1}{2}\sum_{K\neq L}\frac{Z_K Z_L}{R_{KL}}$$
$$- \sum_K \mu_K.B^{tot}(R_K) + \sum_{K>L}\mu_K^T D_{KL}\mu_L \quad \text{.....(25)}$$

The operator for the kinetic momentum is given by

$$\pi_i = -i\nabla_i + A^{tot}(r_i) \quad \text{.....(26)}$$

where $A^{tot}(\mathrm{r_i})$ is the vector potential at the position of electron *i*, constructed in such a way that its curl reproduces the magnetic induction $B^{tot}(\mathrm{r_i})$ arising from the external field and the NMR active nuclei:

$$B^{tot}(r_i) = \nabla_i \times A^{tot}(r_i) \quad \text{.....(27)}$$

In the presence of a static magnetic field *B* and nuclear moment μ_K, the vector potential and the magnetic induction may each be decomposed into separate contributions from the external field and from each nucleus:

$$A^{tot}(r_i) = A_0(r_i) + \sum_K A_K(r_i) \quad \text{.....(28)}$$

$$B^{tot}(r_i) = B + \sum_K B_K(r_i) \quad \text{.....(29)}$$

The vector potential $A_O(\mathrm{ri})$ for a homogeneous external magnetic field represented by a constant magnetic-induction vector *B* is written as

$$A_O(r_i) = \frac{1}{2} B \times r_{iO} \quad \text{.....(30)}$$

where the subscript *O* indicates that the vector potential vanishes at the origin of the vector potential O, known as the gauge origin. The vector potential associated with the nucleus is written as

$$A_K(r_i) = \alpha^2 \frac{\mu_K \times r_{iK}}{r_{iK}^3} \quad \text{.....(31)}$$

where α is the fine structure constant (equals 1/137). Unlike for the external vector potential $A_O(\mathrm{r_i})$, there is a preferred gauge origin (the position of the nucleus) for the nuclear vector potential $A_K(\mathrm{r_i})$.

2.5. Interaction Terms

The first-order interaction terms appear in the paramagnetic contributions to shielding and spin-spin coupling constant, whereas the second-order interaction terms are the diamagnetic terms. These properties can be derived from the derivative of the Hamiltonian with respect to the magnetic induction *B* at zero field and zero magnetic moments as[55,57]

$$\frac{\partial H}{\partial B} = h_B^{orb} + h_B^{spn} \text{.....(32)}$$

The first term couples the external field to the orbital motion of the electron by means of the orbital angular-momentum operator which can be written as

$$h_B^{orb} = \frac{1}{2}\sum_i l_{io} = -\frac{1}{2}\sum_i \mathrm{ir}_{io} \times \nabla_i \quad \text{.....(33)}$$

The second term couples the external field to the spin angular-momentum operator and can be written as

$$h_B^{spn} = -\sum_i m_i = \sum_i s_i \quad \text{.....(34)}$$

On the other hand, differentiating the Hamiltonian with respect to the magnetic moments at zero field and zero magnetic moments yields:

$$\frac{\partial H}{\partial M_K} = h_K^{PSO} + h_K^{SD} + h_K^{FC} \quad \text{.....(35)}$$

In this case there are three distinct interactions, one involving the orbital motion of the electron and the other two involving the electron spin. Accordingly, the paramagnetic spin-orbit (PSO) operator or the orbital hyperfine operator, which couples the nuclear magnetic moments to the orbital motions, is written as

$$h_K^{PSO} = \alpha^2 \sum_i \frac{l_{iK}}{r_{iK}^3} \quad \text{.....(36)}$$

The spin-dipolar (SD) and the Fermi-contact (FC) operators (involving the interaction of the electrons), which both couple the nuclear magnetic moments to the spin of the electron, are given by

$$h_K^{SD} = \alpha^2 \sum_i \frac{r_{iK}^2 m_i - 3(m_i . r_{iK}) r_{iK}}{r_{iK}^5} \quad \text{.....(37)}$$

$$h_K^{FC} = -\frac{8\pi\alpha^2}{3}\sum_i \delta(r_{iK})m_i \quad \text{.....(38)}$$

where α is the fine structure constant and δ is the Dirac delta function centered at the specific nucleus. The SD operator represents the classical interaction between two magnetic dipoles multiplied by a nuclear magnetic moment. The FC operator represents the direct interaction of the dipole moment of the electron with the source of the nuclear magnetic field and contributes only when the electron is at the nucleus. The global effect for closed-shell states with a total spin of zero is given by[55]

$$\frac{\partial H}{\partial B}|0\rangle = h_B^{orb}|0\rangle <---- \text{imaginary singlet}$$
$$+ h_B^{spn}|0\rangle <---- \text{vanishes} \quad \text{.....(39)}$$

and for the hyperfine interactions, which is a combination of imaginary singlet and triplet wave functions

$$\frac{\partial H}{\partial M_K}|0\rangle = h_K^{PSO}|0\rangle <---- \text{imaginary singlet}$$
$$+ h_K^{SD}|0\rangle <---- \text{real triplet}$$
$$+ h_K^{FC}|0\rangle <---- \text{real triplet} \quad \text{.....(40)}$$

The first-order terms for closed-shell systems, which represent the permanent magnetic moment of the molecule and the hyperfine coupling tensors of the nuclei, vanish because of the absence of real singlet components.

$$\mu_{mol} = -\left\langle 0\left|\frac{\partial H}{\partial B}\right|0\right\rangle = 0 \quad \text{.....(41)}$$

$$A_K = \left\langle 0\left|\frac{\partial H}{\partial M_K}\right|0\right\rangle = 0 \quad \text{.....(42)}$$

Once the first-order terms vanish, then the total electronic energy reduces to

$$E(B,\mu) = E_0 + \frac{1}{2}B^T E^{(20)} B + \sum_K B^T E_K^{(11)} \mu_K + \frac{1}{2}\sum_{K\neq L} \mu_K^T E_{KL}^{(02)} \mu_L \quad \text{.....(43)}$$

The $E^{(20)}$ tensor represents the molecular magnetizability and doesn't appear in the NMR spin-Hamiltonian for a rotating molecule in an isotropic medium. Thus from equations (13) and (18) we have

$$E_K^{(11)} = \left.\frac{\partial^2 E(B,\mu)}{\partial B \partial \mu_K}\right|_{B=0,\mu=0} = \left\langle 0\left|\frac{\partial^2 H}{\partial B \partial \mu_K}\right|0\right\rangle - 2\sum \frac{\left\langle 0\left|\frac{\partial H}{\partial B}\right|n\right\rangle\left\langle n\left|\frac{\partial H}{\partial \mu_K}\right|0\right\rangle}{E_n - E_0} \quad \text{.....(44)}$$

where,

$$\frac{\partial^2 H}{\partial B \partial \mu_K} = -1 + h_{BK}^{dia} = -1 + \frac{\alpha^2}{2} \sum_i \frac{(r_{io}.r_{iK})1 - r_{iK} r_{io}^T}{r_{iK}^3} \quad \text{.....(45)}$$

And also for the other part of the Hamiltonian in equation (25),

$$\frac{\partial^2 H}{\partial \mu_K \partial \mu_L} = D_{KL} + h_{KL}^{DSO} = D_{KL} + \frac{\alpha^4}{2} \sum_i \frac{(r_{iK}.r_{iL})1 - r_{iK} r_{iL}^T}{r_{iK}^3 r_{iL}^3} \quad \text{.....(46)}$$

Substituting these expressions in to the general expression for second-order energy correction, equation (14), gives Ramsey's expressions[60,61] for the nuclear shielding tensor

$$\sigma_K = \left\langle 0 \middle| \mathrm{h}_{BK}^{dia} \middle| 0 \right\rangle - 2 \sum_{n_s \neq 0} \frac{\left\langle 0 \middle| \mathrm{h}_B^{orb} \middle| n_s \right\rangle \left\langle n_s \middle| (\mathrm{h}_K^{PSO})^T \middle| 0 \right\rangle}{E_{n_s} - E_0} \quad \text{.....(47)}$$

And for the reduced indirect spin-spin coupling tensor,

$$K_{KL} = \left\langle 0 \middle| \mathrm{h}_{KL}^{DSO} \middle| 0 \right\rangle - 2 \sum_{n_s \neq 0} \frac{\left\langle 0 \middle| \mathrm{h}_K^{PSO} \middle| n_s \right\rangle \left\langle n_s \middle| (\mathrm{h}_L^{PSO})^T \middle| 0 \right\rangle}{E_{n_s} - E_0}$$
$$- 2 \sum_{n_T} \frac{\left\langle 0 \middle| \mathrm{h}_K^{FC} + \mathrm{h}_K^{SD} \middle| n_T \right\rangle \left\langle n_T \middle| (\mathrm{h}_L^{FC})^T + (\mathrm{h}_L^{SD})^T \middle| 0 \right\rangle}{E_{n_T} - E_0} \quad \text{.....(48)}$$

where the operators (diamagnetic spin-orbit (h^{DSO}), paramagnetic spin-orbit (h^{PSO})) couple the nuclear magnetic moments to the orbital motion of the electrons (hyperfine operator); and the Fermi-contact (h^{FC}) and spin-dipole (h^{SD}) both couple the nuclear magnetic moments to the spin of the electron. The first summation is over all excited singlet states with energy E_{ns} and the second summation is over all triplet states with energy E_{nT}; the superscript T stands for the transposition of the vectors, n_s denotes singlet excited state and n_T a triplet excited state. The first term in the above equation is given by:

$$h_{KL}^{DSO} = \frac{\alpha^4}{2}\sum_i \frac{(r_{iK}r_{iL})I - r_{iK}r_{iL}^T}{r_{iK}^3, r_{iL}^3} \quad \text{.....(49)}$$

whereas the corresponding expressions for the operators in the second and third terms are given in equations (36) – (38). The reader of this PhD dissertation is referred to review papers[55,57,62] and a monograph[56] for a detailed analysis of the quantum chemical expression of the chemical shielding and spin-spin coupling constants.

Chapter 3
Density Functional Theory Based Methods

3.1. Introduction

In this chapter a short overview of the density functional theory (DFT) based computational methods used in this dissertation for the description of the molecular ground state properties is presented. The reader of this PhD dissertation is referred to recent review papers[63-67] as well as monographs and books[58,59,68-70] and references therein for a detailed analysis of the quantum chemical methods.

DFT seeks to calculate all the properties of atoms and molecules from the electron density.[69,70] DFT is a theory of electronic structure based on the electron density. Within the Born-Oppenheimer approximation;[71] which yields a wave function $\psi(\vec{r}_1, \vec{r}_2 ... \vec{r}_N)$ depending only on electrons and only parametrically on the nuclei, the time-independent electronic Schrödinger equation[72] is the starting point for a nonrelativistic quantum-mechanical description of the stationary molecular properties:

$$\hat{H}\psi(r_i, R_N) = \left[\hat{T} + \hat{V} + \hat{U}\right]\psi(r_i, R_N) = E\psi(r_i, R_N) \quad \text{.....(50)}$$

where $\hat{T}$ is the kinetic energy operator, $\hat{V}$ is some external potential (field) due to the nuclei and $\hat{U}$ is the two-electron operator describing the Coulomb interaction between electrons. The Hamiltonian operator described by position vectors r_i and R_N for an electron and the nucleus, respectively, is then given by

$$\hat{H} = -\frac{1}{2}\sum_i \nabla_i^2 + \sum_i V(r_i) + \sum_i \sum_{j<i} \left(\frac{1}{|r_i - r_j|} \right) \quad \text{.....(51)}$$

The calculations solving this equation directly are expensive or even impossible to carry out for large systems since the wave function is a function of 3*N* coordinates. Instead of describing the electronic structure of a molecule or atom using its wave function, its electron density ρ(r) is used in DFT. In DFT, the properties of a many-electron system can be determined by using a functional, *i. e.* a function of another function, which in this case is the spatially dependent electron density of the system.

3.2. The Hohenberg-Kohn Theorem

The theoretical foundation of DFT is based on the two Hohenberg–Kohn theorems.[73] According to the first theorem, the electron density uniquely determines the Hamiltonian operator and all the properties of a molecule in a ground electronic state are determined by the ground state electron density function ρ_0(x,y,z). The Hamiltonian is then specified by the external potential and the total number of electrons, *N,* which can be computed from the density by integrating over all space.[74]

$$E[\rho] = T[\rho] + V_{ne}[\rho] + V_{ee}[\rho] = \int \rho(r)v(r)dr + F_{HK}[\rho] \quad \text{.....(52)}$$

where $T[\rho]$ represents the kinetic energy, $V_{ne}[\rho]$ and $V_{ee}[\rho]$ the potential energy due to the nuclei and the electrons, respectively, $\rho(r)$ is the electron density, $v(r)$ is the external potential and

$$F_{HK}[\rho] = T[\rho] + V_{ee}[\rho] \quad \text{.....(53)}$$

is a universal functional of the electronic density, which does not depend on a specific system. The term $\int \rho(r)v(r\ )dr$ is the classical interaction of the electrons with the external potential $v(r)$.

The second Hohenberg-Kohn theorem[73] is the DFT variant of the variational principle stating that a trial electron density function will give energy higher than or equal to the true ground-state energy obtained from the true electron density function.[59,68,70,73]

$$E_0 \le E[\rho(r)] \equiv E_0 \le \langle \psi_{\min} | T + V | \psi_{\min} \rangle \quad \text{.....(54)}$$

where $\rho(r)$ is a trial electronic density and E_0 is the true ground state energy, corresponding to the true electronic density ρ_0.

3.3. The Kohn-Sham Equations

Unlike for non-interacting systems described by using orbitals, finding an accurate representation for the kinetic energy of an interacting system is difficult. To overcome this problem Kohn and Sham proposed the most convenient expression for the energy functional in 1965.[74] The Kohn-Sham (KS) approach attains the exact correspondence between the ground-state energy and the density of a system consisting of non-interacting fermions in which the "real" many body system is described by the Schrödinger equation.[72] The energy functional contains three terms: (a) the kinetic energy, (b) the nucleus-electron attraction potential energy, and (c) the electron-electron repulsion potential energy. Each term is a functional of the ground state electron density. The total ground state electronic energy of the real molecule is then written as[74]

$$E[\rho] = T[\rho] + V_{ne}[\rho] + V_{ee}[\rho] \quad (55)$$

The middle term, the classical electrostatic attraction potential energy, is given by

$$V_{ne} = \int \rho_0(r)\, v(r) dr \quad (56)$$

The KS equations are obtained by differentiating the energy with respect to the KS molecular orbitals. The electron density distribution is given as

$$\rho(r) = \sum_{i=1}^{2n} \left| \psi_i^{KS}(r) \right|^2 \quad (57)$$

where ψ^{KS} are the Kohn-Sham spatial orbitals. The KS equation is then given as[70]

$$\left[-\frac{1}{2}\nabla_i^2 - \sum_{\text{nuclei A}} \frac{Z_A}{r_{1A}} + \int \frac{\rho(r2)}{r_{12}} dr_2 + V_{XC}\right]\psi_i^{KS} = \varepsilon_i^{KS}\psi_i^{KS} \quad \text{.....(58)}$$

where the ε^{KS} are the KS energy levels and V_{XC} is the exchange-correlation potential which is a functional derivative of the exchange-correlation energy $E_{XC}[\rho(r)]$

$$V_{XC}(r) = \frac{\delta E_{XC}[\rho(r)]}{\delta\rho(r)} \text{.....(59)}$$

3.4. The Exchange-Correlation Energy Functional

3.4.1. The Local-Density Approximation

Various approximations have been suggested for the exchange-correlation energy, $E_{xc}[\rho]$. The simplest approximation is the local density approximation, LDA. The LDA is based on the assumption that at every point in the molecule the energy density has the value that would be given by a homogeneous electron gas (HEG) which had the same electron density ρ at that point.[59,68,69] The energy density is the energy (exchange plus correlation) per electron.

$$E_{xc}^{LDA}[\rho] = \int \rho(r)\varepsilon_{xc}[\rho(r)]dr \text{.....(60)}$$

where $\varepsilon_{xc}[\rho(r)]$ is the exchange and correlation energy per electron in a uniform electron gas of density $\rho(r)$. The exchange part of the LDA functional is given by,

$$E_x^{LDA}[\rho] = -\frac{3}{4}\left(\frac{3}{\pi}\right)^{1/3}\int \rho(r)^{4/3} dr \text{.....(61)}$$

3.4.2. Generalized Gradient Approximations

The functionals that are functions of both the local density, $\rho(r)$, and the gradient of the charge density, $\nabla\rho(r)$, are termed as generalized gradient approximations, GGA.

$$\left(\frac{\partial}{\partial x}+\frac{\partial}{\partial y}+\frac{\partial}{\partial z}\right)\rho(r) = \nabla\rho(r) \quad \text{.....(62)}$$

The exchange and correlation energies, both negative, is written as

$$E_{xc}^{GGA}(\rho) = E_X(\rho) + E_C(\rho) = \int dr\varepsilon_{xc}(\rho,|\nabla\rho|,\nabla^2\rho) \quad \text{.....(63)}$$

The absolute value of the exchange energy is much bigger than the correlation energy. Generalized gradient approximations generally lead to improved bond angles, bond lengths and energies. The most commonly used exchange energy functional is the B88 (Becke 1988) functional.[75] Examples of gradient-corrected correlation-energy functionals are the LYP[76] (Lee-Yang-Parr) and the P86[77] (Perdew 1986) functionals. A calculation performed with B88 for the exchange-energy functional and P86 for the correlation energy functional is termed as BP86.[59,68,69]

3.4.3. Hybrid Functionals

The admixture of a GGA functional with a fraction of exact exchange from Hartree-Fock is another approach to approximate the exchange-correlation energy functional, leading to what is referred to as hybrid functionals. Hybrid functionals incorporate a portion of exact exchange from Hartree-Fock theory with exchange and correlation from *ab initio* or empirical methods. A hybrid exchange-correlation functional is usually constructed as a linear combination of the Hartree-Fock exact exchange functional and any number of explicit exchange and correlation density functionals.[59,68,69] Generally, the hybrid functional can be written as

$$E_{xc} = aE_x^{HF} + bE_{xc}^{GGA} \quad \text{.....(64)}$$

The Hartree-Fock exchange term is given by,

$$E_x^{HF} = \frac{1}{2}\sum_{i,j}\iint \psi_i^*(r_1)\psi_j^*(r_1)\frac{1}{r_{12}}\psi_i(r_2)\psi_j(r_2)dr_1dr_2 \quad \text{.....(65)}$$

The coefficients *a* and *b* are determined by parameterization. Becke[78] adopted this approach and defined the parameters of the 3-parametre exchange functional. Later this hybrid exchange functional was combined with the Lee-Yang-Parr[76] functional by Stephens *et al.*[79] to get the commonly named B3LYP functional

$$E_{xc}^{B3LYP} = E_{xc}^{VWN} + 0.2(E_x^{HF} - E_x^{VWN}) + 0.72(E_x^{B88} - E_x^{VWN}) + 0.81(E_c^{LYP} - E_c^{VWN}) \quad \text{.....(66)}$$

3.5. Time-Dependent Density Functional Theory

In this section the time-dependent density functional theory, TD-DFT, used for the calculations of the UV/Vis absorption spectra is briefly described. TD-DFT extends the concept of stationary DFT to time-dependent systems. All physical observables for any interacting quantum many-particle system subject to a given time-dependent potential (such as electric or magnetic fields) are uniquely determined by the time-dependent (TD) density and the state of the system at an arbitrary and single instant in time. Its computational foundation is based on the Runge-Gross theorem,[80] the TD analogue of the Hohenberg-Kohn theorem.[81] The Runge-Gross theorem states that for a given initial wave function, there is a unique mapping between the TD external potential of a system and its TD density. The Hamiltonian is given as

$$\hat{H}(t) = \hat{T} + \hat{V}_{ext}(t) + \hat{U} \quad \text{.....(67)}$$

where $\hat{T}$ is the kinetic energy operator, $\hat{U}$ is the electron-electron interaction and $\hat{V}_{ext}$ is the external potential which defines the system along with the number of electrons. The explicit expression of the Runge-Gross equation is given by[80,82]

$$i\frac{\partial}{\partial t}\psi(\vec{r},t) = \left\{-\frac{1}{2}\nabla^2 - \sum_{m=1}\frac{Z_m}{\left|\vec{r}-\vec{R}\right|} + \int\frac{\rho(\vec{r},t)}{\left|\vec{r}-\vec{r}'\right|}d^3\vec{r}' + V_{XC}(\vec{r},t)\right\}\psi(\vec{r},t) \quad \text{.....(68)}$$

where the electron density, ground-state wave function and the exchange-correlation potential are given by the following three equations; respectively,

$$\rho(\vec{r},t) = \sum\left|\psi(\vec{r},t)\right|^2 \quad \text{.....(69)}$$

$$\psi(t=0) = \psi^0 \quad \text{.....(70)}$$

$$V_{XC}(\vec{r},t) = \frac{\delta E_{XC}(\vec{r},t)}{\delta\rho(\vec{r},t)} \quad \text{.....(71)}$$

TD-DFT is used to calculate the energies of excited states of molecular systems based on the linear response function, that is, by analysing how the electron density changes as the external potential changes. The external perturbation in this approach is small and it doesn't completely destroy the ground-state structure of the system.[80,82-85]

3.6. Basis Sets

A basis set is a set of functions used to create molecular orbitals, which are expanded as a linear combination of these functions with appropriately chosen coefficients. Electronic structure calculations of polyatomic molecules typically use the linear-combination-of-atomic-orbitals, LCAO, approximation[59]

$$\left|\psi_k\right\rangle = \sum_\mu c_\mu^k \left|\chi_\mu\right\rangle \quad \text{.....(69)}$$

where χ_μ is the basis set of the atomic orbitals. The most common LCAO basis functions employed presently in quantum chemistry are the Gaussian type orbitals, GTOs, centered on the atomic nuclei. In spherical coordinates, their form is expressed by[59,69]

$$\chi_\mu(r,\theta,\varphi) = Y_{lm}(\theta,\varphi)r^{n-1}e^{-\zeta r^2} \quad \text{.....(70)}$$

where Y_{lm} are the spherical harmonics; ζ is the so-called exponent of the GTO. GTOs are more popular, due to their convenient mathematical properties, than the physically more correct Slater-type orbitals, STO. The better physical behavior of STOs at $r = 0$ and at large r is simulated by working with a somewhat larger set of fixed linear combinations of primitive Gaussian functions χ_μ. These linear combinations lead to contracted Gaussian functions, CGTOs; each of them being specified by a set of exponents and another set of contraction coefficients that are not allowed to change during the calculation of the electronic properties. Depending on the number of CGTOs used per atomic shell, basis sets are referred to as single-ζ (1 CGTO), double-ζ (DZ, 2 CGTOs), triple-ζ (TZ, 3 CGTOs), etc. The flexibility of a basis set is improved by adding functions of higher angular momentum that correspond to the occupied orbitals in the ground state of a particular atom. These are called the polarization functions and are p-type functions for H and He, d-type functions for the second-row atoms, *etc*. This provides additional flexibility needed within the basis set, effectively allowing molecular orbitals to be more asymmetric about the nucleus. This is important when considering accurate representations of bonding between atoms, since the presence of the bonded atom makes the energetic environment of the electrons spherically asymmetric. For example, d-type functions can be added to a basis set with valence p orbitals, and f-functions to a basis set with d-type orbitals. Diffuse functions are those with very small exponents; they allow the charge distribution to be accurately described also in the outer regions of the electron density. The diffuse functions more accurately represent the "tail" portion of the atomic orbitals, which are far from the atomic nuclei.[58,59,68-70]

Chapter 4
Experimental and Computational Methods

In this chapter, the computational and experimental methods used for the study of the molecules considered in the PhD study are presented.

4.1. Experimental

4.1.1. Reagents

[2.2]Paracyclophane, **7**, 99% purity was purchased from Alfa Aesar. The syntheses of [2.2]paracyclophan-13,15-diene **9**,[86] [3.3]paracyclophane **15**,[17,87] [2.3]paracyclophane **16**,[88] phenyl-[2.2]paracyclophane **17**,[89] benzene[2.2]paracyclophane **18**,[90] *trans*-[2.2]naphthalenophane **19**,[90] [2.2]paracyclophan-13-ene **20**,[86] 13-vinyl-[2.2]paracyclophan-13-ene **21**,[91] [2.2.2](1,2,4)cyclophan-15-ene **22**,[92] [2.2.2](1,2,4)cyclophan-17-ene **23**,[93] [2.2.2](1,2,4)cyclophane **29**,[94] [2.4]paracyclophane **30**,[95] [3.4]paracyclophane **31**[88] and [4.4]paracyclophane **32**[42] have been reported earlier. **9**, **15** - **23**, **30** - **32** were provided by Prof. H. Hopf from Institute of Organic Chemistry, Technical University of Braunschweig, Braunschweig, Germany.

4.1.2. NMR Measurements

All room temperature NMR experiments were performed in $CDCl_3$ solutions on either a Bruker DRX-500 MHz or Varian 600 MHz spectrometer using the XWINNMR and VNMRJ acquisition and processing programs, respectively. The 5 mm triple broadband inverse probe equipped with a z-gradient coil was used for ^{1}H and ^{13}C measurements. All ^{13}C, ^{1}H and 2D correlation experiments were carried out using the inverse gradient technique and pulse sequences with adiabatic pulses (^{13}C and ^{1}H gHSQCAD and g-HMBCAD Varan's pulse sequences). Signal assignments were carried out by means of one-dimensional nuclear

Overhauser effect (NOE),[96] correlation spectroscopy (COSY)[97] and (^{13}C,^{1}H)-heteronuclear single-quantum correlation (HSQC)[98] and heteronuclear multiple-bond correlation (HMBC)[99] experiments. Variable-temperature ^{1}H NMR spectra were recorded on a Bruker Avance II 300 MHz spectrometer equipped with a broadband inverse probehead and a BVT 3200 temperature control unit. The reported temperatures were carefully calibrated using methanol chemical shift thermometer.[100] For the chemical shifts tetramethylsilane (TMS) is used as a reference. The values of chemical shifts are given in parts per million (ppm) and those of coupling constants in hertz (Hz).

4.1.3. Analysis of NMR Spectra

^{13}C chemical shifts, and proton-carbon and carbon-carbon coupling constants were read from spectra. To determine the exact values of the proton chemical shifts and proton-proton coupling constants from NMR spectra, the spectra were analyzed numerically using a FORTRAN program developed and used by Prof. Dr hab. Sławomir Szymański which performs iterative least-squares fits to the experimental line shapes.[15] The J_{HH} coupling constant values in the aromatic bridges were either evaluated on the basis of the line-shape fits or, in cases where the resonances of the aromatic protons were singlets, read from splittings in the ^{13}C satellites. With these two parameters included in the optimized set, the fitting algorithm did not converge. Except for the geminal couplings all the above mentioned J_{HH} values could be extracted from room-temperature spectra with very high accuracy, generally 0.01 Hz, using the home-written program developed and used by Prof. Dr hab. Sławomir Szymański, based on the conventional Liouville space approach,[101] which performs iterative line shape fits.

4.1.4. Absorption and Emission Spectra Measurements

All the absorption spectra of the [*m.n*]paracyclophanes, (*m*, *n* = 2 – 4), were measured in *n*-hexane (Aldrich, spectral quality) at 293 K on a Shimadzu UV-3100 spectrophotometer equipped with variable-temperature chambers, allowing temperature controls between 88 K and 333 K, with accuracy of ±1 K in the laboratory of Prof. Dr hab. Jacek Waluk. The excitation spectra were recorded on an Edinburgh FS 900 CDT fluorometer and corrected for the sensitivity of the instrument. Excitation spectra were measured for optical densities not exceeding 0.1 in the maxima of absorption bands in order to avoid nonlinear effects.

4.2. Computational Details

The quantum chemical calculations were performed using either Gaussian quantum chemistry program package[102] at the local supercomputer cluster (*Stallo*) installed at UiT - the Arctic University of Norway, and at the Interdisciplinary Centre for Mathematical and Computational Modeling (ICM) at Warsaw University, Poland, or the Dalton quantum chemistry program package[103] at the University of Tromsø. Additional calculations were also performed at the supercomputer cluster (*Abel*) installed at the University of Oslo, Norway.

4.2.1. Computational Details of [2.2]Paracyclophane 7 and Its Derivatives 17 - 19

The molecules were optimized using Becke's 3-parameter hybrid exchange functional[75] and the Lee-Yang-Parr correlation functional,[76] commonly referred to as B3LYP.[79] The correlation-consistent polarized valence double-zeta and triple-zeta basis sets of Dunning[104] (cc-pVTZ), 6-311G(d,p)[105] and Huz-IV[106] basis sets were used for the geometry optimization, using the first-order geometry optimization methods of Bakken and Helgaker.[107] The calculations of the shielding constants and spin-spin couplings constants were done applying the B3LYP functional, using the 6-311G(d,p), cc-pVTZ and Huzinaga-IV basis set. The latter one was suggested by Kutzelnigg and Schindler[108] based on the atomic basis sets of Huzinaga[106] In order to ensure gauge origin independence of the calculated shielding constants London atomic orbitals[109] were used in all calculations.

4.2.2. Computational Details of Cyclophanes with Unsaturated Bridge(s) 9, 20 - 28

The molecules were optimized using Becke's 3-parameter hybrid exchange functional[75] and the Lee-Yang-Parr correlation functional,[76] commonly referred to as B3LYP.[79] The correlation-consistent polarized valence double-zeta and triple-zeta basis sets of Dunning[104] (cc-pVTZ), 6-311G(d,p)[105] and Huz-IV[106] basis sets were used for the geometry optimization, using the first-order geometry optimization methods of Bakken and Helgaker.[107] The calculations of the shielding constants and spin-spin couplings constants were done applying the B3LYP functional, using the 6-311G(d,p), cc-pVTZ and Huzinaga-IV basis sets. The latter one was suggested by Kutzelnigg and Schindler[108] based on the atomic basis sets of Huzinaga[106] using the implementations of Ruud *et al.*[110] and Vahtras *et al.*[111] London atomic orbitals[109] were used to

ensure gauge origin independence of the calculated shielding constants. Tetramethylsilane (TMS) was used as a reference for the calculations of ^{1}H and ^{13}C chemical shifts.

4.2.3. Computational Details of [m.n]Paracyclophanes (m, n = 2 – 4) 7, 15, 16, and 30 - 32

The molecules were optimized using Becke's three-parameter hybrid exchange functional[75] and the Lee-Yang-Parr correlation functional[76] commonly referred to as B3LYP[79] and the Head-Gordon and coworkers long-range corrected functional which includes damped atom-atom dispersion corrections, ωB97X-D.[112] The augmented correlation-consistent polarized valence triple-ζ basis set of Dunning optimized for spin-spin coupling constants and shielding calculations, referred to as ccJ-pVTZ,[113] and the basis set suggested for NMR parameter calculations by Schindler and Kutzelnigg based on the atomic basis sets of Huzinaga, Huz-IV,[106] were used. London atomic orbitals were used to ensure gauge origin independence of the calculated shielding constants. For the TD-DFT electronic property calculations the CAM-B3LYP[114] and ωB97X-D[112] functionals together with augmented correlation-consistent polarized valence triple-ζ basis set of Dunning (aug-cc-pVTZ)[104,115] were used. Each optimized structure was confirmed by frequency calculations to be the real minimum without any imaginary vibrational frequencies on the potential energy surface. Similar to the experimental measurements, TMS was used as reference for the chemical shift calculations. For the TMS NMR calculations ccJ-pVTZ basis set was used for carbon and hydrogen atoms whereas cc-pVTZ basis set was used for silicon because of the unavailability of the former basis set.

Chapter 5
[2.2]Paracyclophane and its Derivatives

5.1. Introduction

As briefly addressed in Chapter 1, highly strained cyclophanes with small bridges are characterized by a distorted structure compared to unstrained hydrocarbons.[2,116,117] These distortions are known to influence properties of the molecules.[53,54] For such distorted molecules, [2.2]paracyclophane **7** for example, the combined use of theoretical and experimental techniques are considered to be appropriate tools of study. **7** has been a topic of several previous experimental[1,13,20,31,41,43,51,118-122] and theoretical[14,20,22,24-27,30,51] studies due to its interesting properties discussed in Chapter 1. In particular, it is also an excellent model for the study of π-electron interactions between layered benzene rings.[1,18,22,123] The extent of distortion of the aromatic rings of **7** were reviewed by Cram *et al.*[1] The strain energy of **7** is 30.1 kcal/mol[124] whereas its heat of formation is 58.8 ± 0.8 kcal/mol.[125] The computations dealing with its structural distortions,[20,22,26,27,30] ring currents in the molecule,[126] through-bond, through-space[24] and transannular interactions[20] have been reported. Normal vibrations[24] and the importance of electron correlation effects for the π-π interactions in cyclophanes[22] using both *ab initio* and DFT methods have also been analyzed.

As pointed out in Chapter 1, there has been a vivid discussion whether **7** has an eclipsed D_{2h} or twisted D_2 equilibrium geometry (where in the latter case the mutual twist of the benzene rings is combined with a twist around the C13C14 and C15C16 bridges), in spite of the fact that the published experimental X-ray data by Lyssenko *et al.*[20] measured at 100 K, where no disorder occurs, unequivocally favor the former structure. On the other hand, based on analysis of IR spectra, Walden and Glatzhofer[30] concluded that a small twist (characterized by $C_{sp2}C_{sp3}C_{sp3}C_{sp2}$ torsional angle ϕ of 3.9°, defined in Fig. 2) with a barrier of 1 cal/mol, which is certainly within the limits of error, is present. The X-ray results by Stalke measured at 19 K, unpublished but cited by Grimme,[127] yielded a twist angle of 12.6° for another crystalline phase than that present at room temperature. Unfortunately, in the paper by Grimme,[22] citing the latter

results, there was no discussion of the results by the Lyssenko group[20] and Grimme's paper was sometimes cited as experimental one.[14,28]

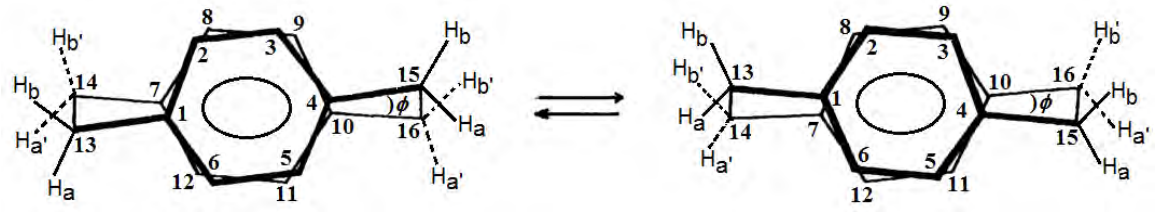

Fig. 2. The definition of the twist dihedral angle (ϕ) and twisting-rocking mode of **7**

Walden and Glanzhofer[30] calculated the structure and normal vibrations of **7** using the hybrid Hartree-Fock/gradient corrected DFT B3LYP/4-21G(d) method and obtained a twist angle ϕ of 3.9°, in good agreement with the experimental "half twist angle" value of 3.2° reported by Hope *et al.*[23] It is noteworthy that the "half twist angle" obtained by Hope *et al.*[23] is close to the result obtained by Lyssenko *et al.*,[20] even though the molecule in the former work has D_2 symmetry while it has D_{2h} symmetry in the latter work. The "half twist angle" in the Hope *et al.*[23] work was defined as the twist angle of each aromatic ring in opposite directions around the common normal, which gives a full twist angle of 6.4°.[128] Henseler and Hohlneicher,[26] using MP2/6-31G(d), obtained a very large ϕ value equal to 21.8°. They incorrectly stated that in the paper by Hope and coworkers[23] the value of the torsional angle has not been reported even though the "half twist angle" value of 3.2° was given in that paper.

In a combined experimental and computational (HF, MP2, B3LYP with 6-31G(d) basis set) study, Lyssenko *et al.*[20] found the eclipsed structure (ϕ = 0°) as the minimum structure with a considerable anisotropy of twist vibrations even at 100 K. The experimental results of **7** by Lyssenko *et al.*[20] have often been neglected in most of the theoretical studies. However, it should be noted that comparison of experimental and computed geometries is often very difficult since the latter refer to an isolated molecule in the gas phase while the former are usually measured in the solid state. The argument given by Lyssenko *et al.*,[20] in favor of the low force constant for the twist on the basis of an inspection of the Cambridge structural database (CSD) of the derivatives of **7**, does not seem valid since a substitution on either aromatic ring or on the bridge

introduces steric strain that would force a twist. The claim by Lyssenko *et al.*[20] that there are no through-space interactions between the rings in **7** also seems questionable.

On the basis of B3LYP/6-31G** calculations of the structure of **7**, Pelloni and coworkers[126] obtained a slightly twisted structure but they carried out the calculations of magnetic properties for the ideal D_{2h} structure since they found the results to be independent of such a simplifying assumption. With regard to the energy differences between the two structures, the results obtained from spin-component-scaled Moller-Plesset second-order perturbation theory (SCS-MP2) computations using the cc-pVTZ basis set by Grimme[22] indicated that the lowest energy structure has D_2 symmetry with C1C13C14C7 twist angle of 17.6°, where the barrier to the interconversion between the two (equivalent) twisted isomers is as low as 0.2 kcal/mol (depicted in Fig. 3).

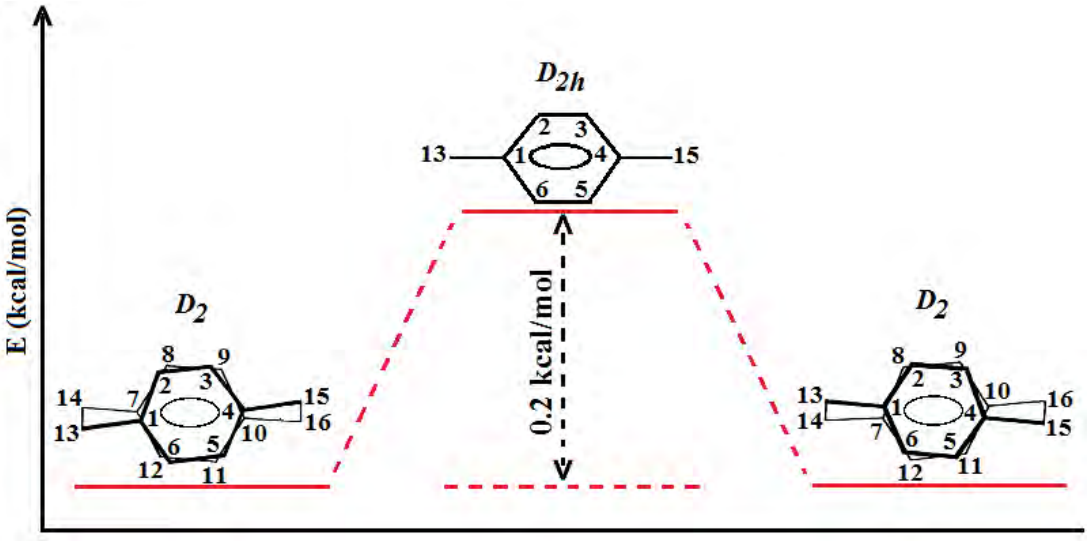

Fig. 3. The barrier to the interconversion between the two conformers of **7**. In the D_{2h} structure the two benzene rings as well as the bridges are eclipsed

The theoretical methods give results either for the structure with D_2 or D_{2h} symmetry for **7** based on the type of functional used. For instance, the hybrid functional B3LYP gives D_{2h} geometry[14,16] whereas dispersion corrected pure functionals (for example ωB97X-D, B97-D) give D_2 structure,[14,22,24] with value of ϕ ranging from 10° to 15°. More specifically, uncorrected

functionals (*e.g.* B3LYP) overestimate the interring separation distance as well as the $C_{sp3}C_{sp3}$ bond lengths of **7** due to their over-repulsive character in the van der Waals distance regime. MP2 underestimates these interactions.[129-131] On the other hand, when dispersion correction is introduced to the functional, the results show a better correlation with the experimental bond lengths, since they adequately describe the dispersive interactions. However, when compared to the experimental twist angle[20,23] of **7**, the larger than 10° value of the angle obtained from the calculations seems unreliable. This behavior of the functionals has been reported by Grimme *et al.*[25] stressing that the inclusion of dispersion correction to the functionals improve the geometry optimization results. Grimme's[22] previous study also demonstrated that the ϕ value of **7** is dependent on the method applied. Except for the DFT-B3LYP result yielding a zero twist angle correlating with the experimental result,[20] all other values were larger than 10° (17.6°, 18.7° and 10.7° using SCS-MP2, MP2 and DFT-PBE, respectively) while the inspection of the Cambridge Database for **7** and its derivatives yielded mostly $\phi \leq 3°$. Caramori and coworkers[24] also found that the dihedral angles of the ethano-bridges are very dependent on the model. Their geometry optimizations using the cc-pVDZ basis set for all methods, as well as MP2/6-31G(d;0.25) calculation have yielded twisted D_2 structures while B3LYP have resulted in a close agreement to the eclipsed D_{2h} conformer.

DFT calculations for **7** using B3LYP, M06-2X, B97-D and ωB97X-D functionals were also reported by Bachrach.[14] The author compared the results obtained from different functionals with the literature values aiming to find which functional describes the geometry, in particular the C1C13C14C7 twist angle, the best. Unfortunately, Bachrach does not cite the "half twist angle" value of 3.2° as the experimental aromatic ring twist angle value reported by Hope *et al.*,[23] but rather a much larger angle of 12.6°. It should be stressed that the 12.6° cited by Bachrach[14] is the deformation angle (C2C1C6C5) of the aromatic rings reported by Hope *et al.*[23] Interestingly, only one of the functionals used by Bachrach gives a value for the $C_{sp2}C_{sp3}C_{sp3}C_{sp2}$ torsional angle of *ca.* 10°, some of them yielding values as large as 18°.

Despite the many studies advocating a large twist angle, we believe that the zero value of the angle determined by Lyssenko *et al.*[20] in 2003 or the small values less than 6° to be the most reliable. The very low energy differences of 0.2 kcal/mol between the D_{2h} and D_2 structures calculated by Grimme[22] at the SCS-MP2/cc-pVTZ level and that of 1 cal/mol reported by Walden and Glatzhofer[30] on the basis of DFT calculations using a small 4-31G(d) basis set

indicate that an experimental solution to the problem of the eclipsed D_{2h} or twisted D_2 equilibrium geometry of **7** is not trivial. In addition, some of the bond lengths of **7** are also temperature dependent. For instance the $C_{sp3}C_{sp3}$ bridge bond length was found to be longer, 1.558[12] at 93 K and 1.579 at 100 K,[20] and 1.630[12] and 1.569[23] at 297 K. The X-ray analysis of **17** is reported by Kuś *et al*.,[89] whereas that of **18** and **19** by Cram *et al*.[90] Kamya and Muchall carried out DFT calculations for ten substituted [2.2]paracyclophanes and three [3.3]paracyclophanes and analyzed their geometries and electronic structures.[132] The latter authors stated that some shortcomings are shown by B3LYP in reproducing the experimental geometries compared to PBE0 and BH&H functionals.

With regard to NMR spectra of cyclophanes, three comprehensive reviews by Ernst[53,54,133] take the major part. In these reviews the static proton spectra of **7**, **15**, **18** and **19** and of cyclophane derivatives are discussed. Pechlivanidis *et al*.[88] reported the synthetic routes of [*m.n*]paracyclophanes (*m*, *n* = 2 - 4) together with a few proton chemical shifts from the static spectra. Recently a solid state NMR analysis of **7** has also been reported by Halling *et al*.[51] The proton and carbon chemical shifts in **7** were calculated by Caramori *et al.*,[24] while Bifulco and Mangoni[34] analyzed ^1H-^1H scalar couplings across the two stacked aromatic rings in derivatives of **7**. Despite the fact that experimental and calcualted NMR spectra of **7** have been reported, limited NMR data for [2.2]paracyclophanes are given in synthetic works and the data on the coupling constants are scarce. It should be stressed that, except **7**, the rest of the molecules got very little attention in the experimental and theoretical studies; *e.g.* NMR data are only given in synthetic works for identification purposes. Therefore, NMR spectra of all compounds under study have been measured. In addition, the NMR spectra for **7**, **17**, **18** and **19** were measured with a focus on the vicinal J_{HH} coupling constants within the aliphatic bridges and the possible temperature dependences of the spectra. As stated above, DFT calculations of the structures and NMR parameters are very important to address the dilemma related to the symmetry of **7** as well as to shed further light on solving the problem. The DFT analysis of the structural parameters and NMR spectra of **17**, **18** and **19** are investigated for the first time.

5.2. Geometry of [2.2]Paracyclophane 7

As discussed in section 5.1, the room-temperature experimental X-ray results of **7** exhibit disorder and depend significantly on temperature. The compound has also a low barrier to

twisting around the $C_{sp3}C_{sp3}$ bond,[20,22] as shown in Fig. 2. Selected calculated and experimental structural parameters of **7** are collected in Table 1. The representation of the optimized geometry using the B3LYP functional is shown in Fig. 4.

Table 1. Selected bond lengths (in Å), bond angles and torsional angles (in degrees) in **7**, calculated using the B3LYP functional and different basis sets, and the corresponding experimental results

	cc-pVDZ	cc-pVTZ	Huz-IV	Exp.,[20] D_{2h}	Exp.,[23] D_2
			Bonds lengths		
C1C2	1.404	1.397	1.397	1.400	1.386 (1.394)
C1C13	1.515	1.510	1.509	1.508	1.511 (1.514)
C2C3	1.397	1.389	1.389	1.392	1.387 (1.394)
C13C14	1.612	1.612	1.611	1.579	1.591 (1.569)
			Bond angles		
HC13H	106.8	106.9	106.9	109.0	-
C1C2C3	120.7	120.7	120.8	120.7	120.7
C1C13C14	113.6	113.7	113.7	113.6	113.7
C2C1C6	116.8	116.8	116.7	117.0	117.0
C2C1C13	121.0	120.9	121.0	120.9	120.8
C4C1C13	156.4	156.2	156.2	156.4	167.4
			Torsional angles		
C1C13C14C7	0.0	-0.4	-0.4	0.0	6.4[a]
C2C3C4C5	14.9	15.2	15.2	14.4	12.6

[a] half twist angle of 3.2° is given in the original paper by Hope *et al.*[23]

Most calculated bond lengths are larger than the corresponding experimental data, but the values computed using the B3LYP functional with the cc-pVTZ basis set are closest to the experimental results by Lyssenko *et al.*[20] The calculated C13C14 bond length, $C_{sp3}C_{sp3}$, is too long as compared to the experimental results of Lyssenko *et al.*[20] However, all the results suggest a significant lengthening of the bond lengths, largely overestimated by all methods. In agreement

with these findings, this lengthening is much smaller for the $C_{sp2}C_{sp3}$ bonds than for the $C_{sp3}C_{sp3}$ bond. For all methods used, the calculated C1C2 bond is slightly longer than the C2C3 one. This trend agrees with the results of the Lyssenko group measured at 100 K in 2003[20] but not with those obtained at room temperature by Hope *et al*. in 1970.[23]

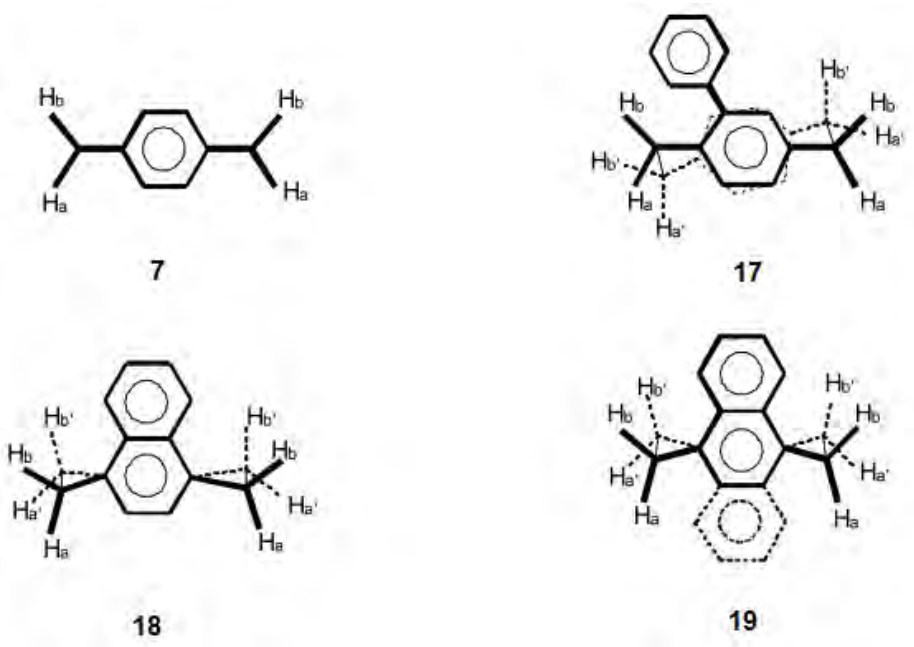

Fig. 4. Representation of the optimized structures of the ethano bridges in **7**, **17**, **18** and **19**, optimized using B3LYP/Huz-IV

Except the determination of the C4C1C13 bond angle by Hope *et al*.[23] and the X-ray determined (and thus quite inaccurate) HC13H bond angle value of Lyssenko *et al*.,[20] there is a very satisfactory agreement between all the experimental and calculated values for the bond angles. The same agreements are also obtained for the dihedral angles. The computed values of the C2C3C4C5 angle describing the nonplanarity of the aromatic rings, are very close to each other indicating that this deformation angle does not significantly depend on the bridge twisting. The calculated twist angle, C1C13C14C7 dihedral angle describing the mutual twist of the aromatic rings, does not exceed 1.2°. If these results describe the real situation in solution, the D_{2h} symmetry can safely be assumed for **7**, in agreement with the structure determined by Lyssenko *et al*.[20] Previously reported computed values gave a value greater than 10° for this twist

angle, for instance those reported by Grimme.[22] However, taking into account that the MP2 calculations are known to overestimate nonbonding repulsions, the $C_{sp2}C_{sp3}C_{sp3}C_{sp2}$ torsional angles should not be larger than *ca*. 6° and probably even smaller. As highlighted in Chapter 1 and the above introduction, it should be stressed that the large experimental value of Stalke,[127] which was only cited,[22] has not been published yet. Such a high experimental value of the angle has furthermore not been reported by any other group for any [2.2]paracyclophane derivatives. This discrepancy can be due to the phase transition at 50 K.[134] As discussed in the Introduction, the recent calculations by Bachrach[14] using functionals other than B3LYP yielded much larger values for the $C_{sp2}C_{sp3}C_{sp3}C_{sp2}$ torsional angle, in disagreement with all published experimental observations.[127]

5.3. Geometry of the Derivatives of [2.2]Paracyclophane

The X-ray analysis of phenyl-[2.2]paracyclophane **17** has been published,[89] but no calculations for this molecule have been reported. In view of the possibility of an internal rotation around the C2C17 bond of **17** in solution and in the gas phase (to which the calculations refer), there is a possibility of two rotational isomers with C1C2C17C18 torsional angles adopting values of *ca.* 48° and 134°, shown in Fig. 5. However, the calculated energy difference of 2.2 kcal/mol between these isomers corresponds to an approximately 98% prevalence of the former rotamer. Thus, only the data for this conformer will be compared to the experimental results. On the other hand, there are no experimental results of the geometry of benzene[2.2]paracyclophane **18**, only the structure of the complex with $GaBr_4$ found in the literature.[135] For that of *trans*-[2.2]naphthalenophane there is one experimental study.[136] However, in this case the existence of two independent molecules in the unit cell makes a comparison of the experimental structural parameters with the calculated values difficult.

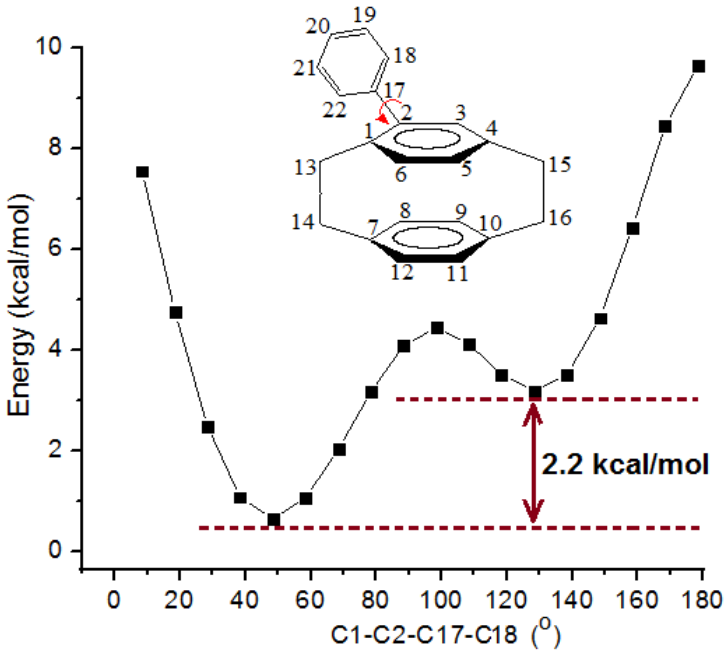

Fig. 5. Potential energy surface of **17** calculated using B3LYP/6-311G(d,p). Total electronic energy (kcal/mol) versus the C1C2C17C18 torsional angle (degrees)

Selected bond lengths and angles calculated using B3LYP/cc-pVTZ for cyclophanes **17**, **18** and **19** and the corresponding experimental values (for **17** and **19**) are collected in Table 2. The calculated values for the inter-ring bridge bonds are large, but they reproduce the observed lengthening of the bonds. The experimental (*vs.* calculated using B3LYP /cc-pVTZ) values of C13C14 and C15C16 bond lengths are 1.579 Å[3] and 1.591 Å[20] (*calc*. 1.611 Å) for **7**; 1.548 Å[89] and 1.581 Å[89] (*calc*.1.608 Å) for **17**; (*calc*. 1.612 Å) for **18**; and 1.569 Å[136] and 1.574 Å[136] (*calc*. 1.599 Å) for **19**. For most saturated bridge bonds the lengthening is overestimated by about 0.03 Å using the calculations, although the excess reaches 0.06 Å for the bridge close to the phenyl substituent in **17**. The differences between the calculated and experimental values of the $C_{sp2}C_{sp3}$ and $C_{sp2}C_{sp2}$ bond lengths are in most cases less than 0.01 Å. For molecules **7**, **17** and **19**, nonplanar boat structures of the cyclophane aromatic rings have been found both experimentally and by the calculations. Similarly, the calculated structure of **18** suggests a boat structure. The rings are characterized by C1C2C3C4 torsional angles close to zero with a maximum value of 2.1° (*calc*.) and 1.6° (*exp*.) obtained for phenyl-[2.2]paracyclophane **17**.

The experimental values for the torsional angles are also reproduced satisfactorily by the calculations except the C1C13C14C7 and C3C2C17C18 angles in **17**. It should be noted that the experimental value for the latter angle can depend considerably on the crystal forces, while the calculated angle was obtained for the isolated molecule in gas phase. All trends in the experimental values for the bond angles are very accurately reproduced by the calculations. In most cases the differences are smaller than 0.5^{o} and in very few cases they exceed 1^{o}. The C2C1C6, C3C4C5, C8C7C12 and C9C10C11 as well as the C18C17C22 and the symmetrical angles in **18** and **19** are squeezed to the value of *ca.* 117^{o}, whereas other angles in the aromatic rings are slightly expanded. The considerable tilt of the substituents out of the corresponding aromatic cyclophane ring plane is well reproduced by the calculations (the calculated value of 156.9^{o} of the C1C4C15 angle, while the corresponding experimental result of 157.9^{o} is considerably less than the *ca.* 180^{o} expected for the planar structure, for example in *para*-xylene **8**). On the other hand, the small tilt of the phenyl substituent of **17** represented by the C2C17C20 and C5C2C17 angles is also satisfactorily reproduced by the calculations.

There is a reasonable agreement between the calculated and experimental values for the torsional angles except for the C1C2C17C22 and C1C13C14C7 angles for **17** (Table 3). The origin of this discrepancy is not clear. Several factors could influence the geometry of this highly strained molecule in the isolated and crystalline state. For example, the X-ray value for the distance between H13b and H18 atoms (the aliphatic protons in front and behind the drawing plane are labeled a and b, respectively) is 2.281 Å, less than the sum of the van der Waals radii for hydrogen atoms.

Table 2. Selected bond lengths (in Å) of **17** - **19**, calculated using B3LYP/cc-pVTZ, and the corresponding available experimental results. For **19**, because of the existence of two independent molecules in a unit cell, two experimental values are given. Δ is the difference between the calculated and experimental bond lengths in Å.

	17			**18**		**19**	
	Calc.	Exp.[89]	Δ	Calc.	Calc.	Exp.[136]	Δ
				$C_{sp3}C_{sp3}$			
C13C14	1.608	1.548	-0.060	1.612	1.599	1.569, (1.574)	-0.030, (-0.025)
C15C16	1.605	1.581	-0.024	1.612	1.599	1.569, (1.574)	-0.025, (-0.025)
				$C_{sp2}C_{sp3}$			
C1C13	1.516	1.512	-0.004	1.511	1.512	1.505, (1.509)	-0.007, (-0.003)
C4C15	1.510	1.512	-0.002	1.511	1.512	1.506, (1.520)	-0.006, (0.008)
C7C14	1.510	1.510	0.000	1.509	1.512	1.506, (1.520)	-0.006, (0.008)
C10C16	1.509	1.504	-0.005	1.509	1.512	1.505, (1.509)	-0.007, (-0.003)
				$C_{sp2}C_{sp2}$			
C1C2	1.412	1.411	-0.001	1.418	1.432	1.437, (1.423)	-0.005, (0.007)
C1C6	1.395	1.390	-0.005	1.416	1.372	1.364, (1.359)	0.006, (-0.013)
C2C3	1.398	1.398	0.000	1.423	1.435	1.424, (1.423)	-0.011, (-0.012)
C2C17	1.485	1.487	-0.002	1.413	1.413	1.409, (1.416)	-0.004, (0.003)
C3C4	1.395	1.387	-0.008	1.418	1.432	1.427, (1.428)	-0.005, (-0.004)
C4C5	1.393	1.390	-0.003	1.416	1.372	1.362, (1.369)	-0.010, (-0.003)
C5C6	1.387	1.381	-0.006	1.410	1.409	1.406, (1.406)	-0.003, (-0.003)
C7C8	1.397	1.391	-0.006	1.418	1.372	1.359, (1.362)	-0.013, (-0.010)
C7C12	1.396	1.386	-0.010	1.419	1.432	1.423, (1.427)	-0.005, (-0.006)
C8C9	1.388	1.376	-0.012	1.422	1.409	1.369, (1.364)	-0.040, (-0.045)
C9C10	1.396	1.389	-0.007	1.418	1.413	1.423, (1.362)	0.010, (-0.051)
C10C11	1.396	1.389	-0.007	1.419	1.432	1.428, (1.437)	-0.004, (0.005)
C11C12	1.389	1.383	-0.006	1.389	1.413	1.423, (1.424)	0.010, (0.011)
C17C18	1.399	1.397	-0.002	1.394	1.373	1.364, (1.357)	-0.009, (-0.016)
C18C19	1.389	1.384	-0.005	1.405	1.405	1.389, (1.394)	-0.016, (-0.009)
C19C20	1.389	1.375	-0.014	1.394	1.373	1.355, (1.362)	-0.018, (-0.011)
C20C21	1.390	1.385	-0.005	-	-	-	-
C21C22	1.388	1.382	-0.006	-	1.373	1.364, (1.364)	-0.007, (-0.007)

Table 3. Selected bond angles and torsional angles (in degrees) of **17** - **19** calculated using B3LYP/cc-pVTZ, and the corresponding available experimental results. For **19**, because of the existence of two independent molecules in a unit cell, two experimental values are given. Δ is the difference between the calculated and experimental bond and torsional angles in degrees.

	17			**18**	**19**		
	Calc.	Exp.[89]	Δ	Calc.	Calc.	Exp.[136]	Δ
				$C_{sp2}C_{sp2}C_{sp2}$			
C1C2C3	118.1	117.9	0.2	118.6	119.3	119.6, (119.0)	0.3, (-0.3)
C1C6C5	121.8	122.1	-0.3	119.8	121.3	121.2, (121.1)	-0.1, (0.2)
C2C1C6	117.0	117.4	-0.4	116.9	117.3	117.6, (117.7)	0.3, (0.4)
C2C3C4	122.6	122.7	-0.1	119.3	119.3	119.5, (120.2)	0.2, (0.9)
C3C4C5	116.6	117.0	-0.4	116.9	117.3	116.8, (117.6)	-0.5, (0.3)
C4C5C6	119.8	119.9	-0.1	119.8	121.3	120.2, (121.7)	-0.1, (0.3)
				$C_{sp2}C_{sp2}C_{sp3}$			
C1C4C15	156.9	157.9	-1.0	155.4	155.6	155.8, (156.5)	0.2, (-0.1)
C2C1C13	123.5	122.7	0.8	122.3	122.5	121.7, (121.4)	0.2, (-0.1)
C3C4C15	121.0	120.8	0.2	122.4	122.6	120.3, (120.5)	-0.3, (-0.1)
C4C1C13	154.1	154.7	-0.6	155.4	155.6	155.6, (155.0)	0.0, (-0.6)
C5C4C15	121.4	121.2	0.2	119.0	119.0	119.5, (119.1)	0.5, (0.1)
C6C1C13	117.9	118.2	0.3	119.4	119.0	120.5, (120.3)	1.5, (1.3)
				$C_{sp2}C_{sp3}C_{sp3}$			
C1C13C14	113.6	113.7	0.1	113.6	113.3	112.6, (113.0)	-1.3, (-0.3)
C4C15C16	113.5	113.1	-0.4	113.6	113.3	112.6, (112.2)	-0.7, (-1.1)
C7C14C13	113.7	114.1	0.4	113.2	113.3	112.2, (112.2)	-1.1, (-1.1)
				$C_{sp2}C_{sp2}C_{sp2}C_{sp2}$			
C2C1C6C5	15.6	13.0	2.6	12.7	16.3	14.8, (-14.5)	-1.5, (-1.8)
C2C3C4C5	14.6	13.1	1.5	16.4	16.0	14.2, (-14.5)	-1.8, (-1.5)
C3C2C1C6	-17.0	-14.8	-2.2	-16.4	-16.0	-15.6, (14.3)	-0.4, (-1.7)
				$C_{sp2}C_{sp3}C_{sp3}C_{sp2}$			
C1C13C14C7	-14.6	-2.0	-12.6	-10.7	-15.2	-15.7, (-17.5)	-0.5, (-2.3)
C4C15C16C10	-10.6	-7.6	-3.0	-10.7	-15.2	-16.0, (-17.0)	-0.8, (-1.8)

5.4. ^{1}H Chemical Shifts

The experimental ^{1}H NMR spectrum for the aliphatic protons of **7** is shown in Fig. 6, whereas the experimental and calculated (using B3LYP/6-311G(d,p), and B3LYP/Huz-IV) proton chemical shifts values are collected in Fig. 7. Except for H17 and H18 of **19**, the calculated values of the aromatic protons are larger than the experimental results, whereas no such regularity for the aliphatic protons exists. The experimental value of the aromatic proton signal at 7.046 ppm for *para*-xylene **8** (http://en.wikipedia.org/wiki/P-Xylene_(data_page)) is shifted upfield to 6.475 ppm for **7** and split for **17** (6.513 - 6.642 ppm). The simulation of the proton spectra of **7** shown in Fig. 6 enabled us to determine very accurate proton chemical shifts. The proton chemical shifts of the phenyl substituent are larger by almost 1 ppm than the corresponding values for the aromatic cyclophane signals. For molecules **18** and **19**, the influence of one ring current on the other ring signals is more diversified. The resonances of H9 in the two latter cyclophanes are shifted considerably upfield, to 5.506 and 5.756 ppm, whereas the change is smaller for the H6 proton in **18** (6.803 ppm). On the other hand, the signals of the naphthalene protons of the outer rings (H17 – H24) of **19** are shifted to 7.405 and 7.728 ppm, downfield relative to the corresponding *para*-xylene value given above. For the aliphatic proton signals, their chemical shifts are 3.072 ppm for **7**, whereas for *para*-xylene they absorb at about 2.296 ppm.

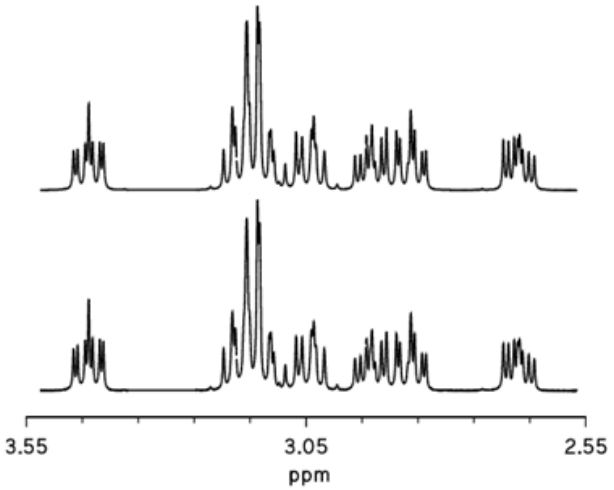

Fig. 6. Partial experimental ^{1}H NMR spectrum (500 MHz) at room temperature of the aliphatic protons in **7** (bottom) and the theoretical best fit spectrum (top)

For obvious reasons, the presence of the aromatic substituent in **17** slightly changes the protons signals on the bridge that are far from it, but it differentiates considerably between the proton signals of the closer ethylene bridge. In particular, the signal of H13b, closer to the phenyl substituent, has moved from 3.072 ppm in **7** to 3.438 ppm in **17**, while the chemical shifts of the signals of the other protons on the C13C14 bridge changed to the values of 2.671 - 3.174 ppm. In **17**, the chemical shift of the signal of the H13b proton closer to the outer aromatic ring is larger than that of the more distant H13a proton (3.438 *vs*. 2.933 ppm). The same behavior is observed in **18** and **19**. The variation of the chemical shifts for the H14 protons in **17** and **18** is much smaller and exhibits the opposite trend.

It should be emphasized that in almost all cases the calculated chemical shifts follow the experimental trends except for a few proton chemical shifts. For instance, comparison of the chemical shifts of H11 and H12 of **17** shows that, contrary to the B3LYP/6-311G(d,p) calculations which differ from the experimental data by 0.19 ppm, the B3LYP/Huz-IV ones give different trend than the experimental results (see Fig. 7). With few exceptions, for most of the protons signals (H13 for **7**; some for **17**; H12 for **18**; and H13, H21 and H22 for **19**), the calculated chemical shifts give smaller values compared to the corresponding experimental values..

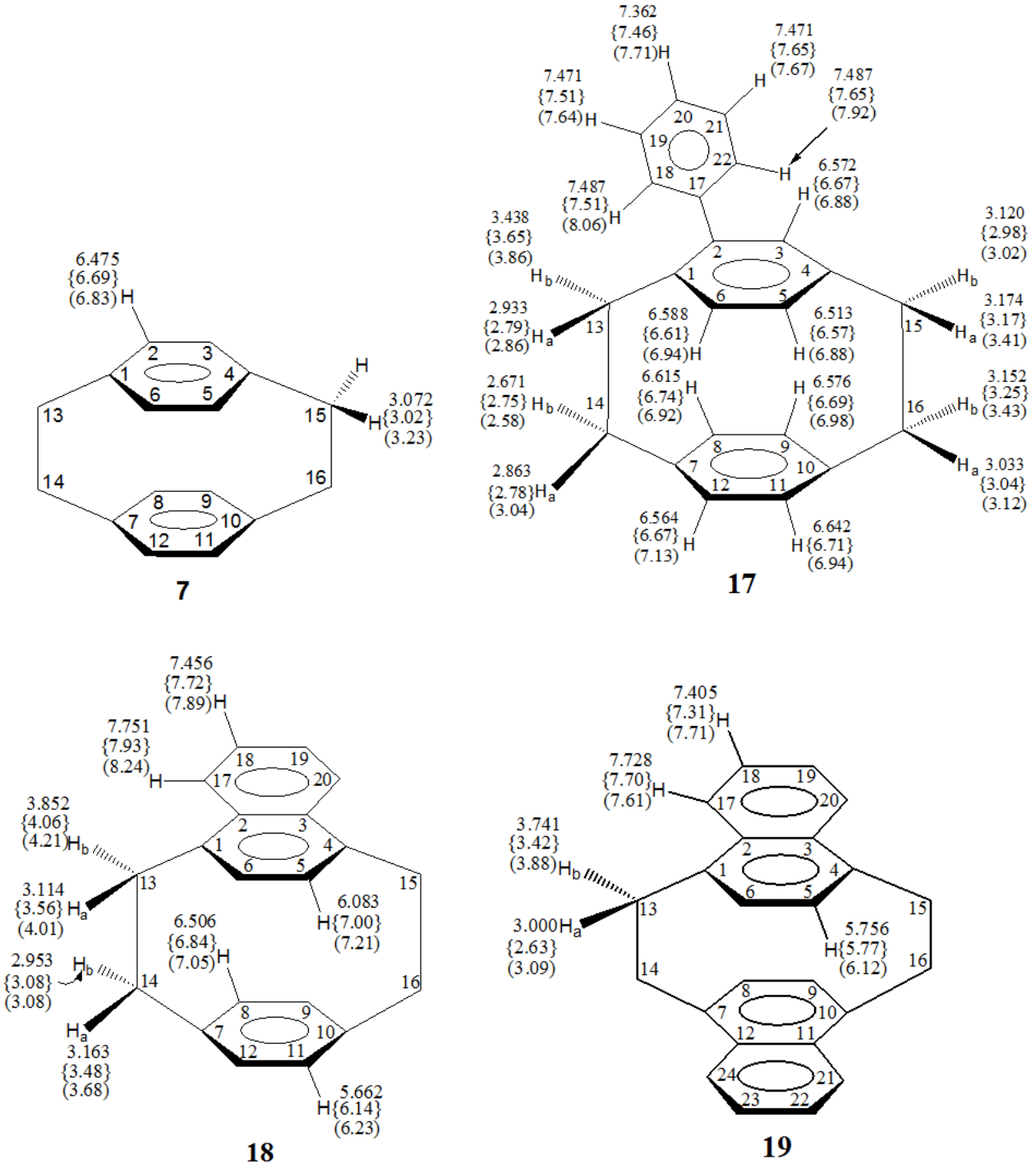

Fig. 7. ^{1}H chemical shifts (in ppm) for **7**, **17**, **18** and **19**; experimental values (this work) – no brackets, calculated using the B3LYP functional are denoted by curly brackets and parenthesis for 6-311G(d,p) and Huz-IV basis sets, respectively. In *para*-xylene the chemical shift of the methyl protons is 2.296 ppm, and of the aromatic ones is 7.046 ppm.

5.5. ^{13}C Chemical Shifts

The experimental and calculated values for the ^{13}C signal positions of **7**, **17** – **19** presented in Fig. 8 reveal that, except numerous very close aromatic signals of **17**, the chemical shifts follow roughly the same trends. Unlike the proton chemical shifts, the calculated values for the aliphatic carbon atoms are larger than those for the aromatic atoms, while no such relation for the aromatic signals could be found. The comparison of the signal positions of the parent [2.2]paracyclophane **7** with the corresponding atoms of *para*-xylene **8** values of 134.66 ppm, 128.97 ppm and 20.90 ppm (http://en.wikipedia.org/wiki/P-Xylene_(data_page)) reveals considerable differences due to both the nonplanar distortion of the aromatic rings and the small separation distance of the rings. The most interesting results are those obtained for **17** bearing an additional phenyl substituent. For this molecule the largest chemical shifts of over 140 ppm have been both measured and calculated for the C2 and C17 atoms forming the bridge between the cyclophane skeleton and the phenyl substituent. As expected, the second largest values have been obtained for the bridgehead, C1, C4, C7 and C10, carbon atoms. The three latter carbon atom positions of **17** were only slightly changed in comparison to the corresponding values for the parent compound **7**. However, in addition to a considerable change in the signal of the C2 carbon atom, the largest differences between **7** and **17** (all smaller than 3.2 ppm) due to the presence of the aromatic substituent at the C2 signal manifest themselves at the C6, C13, C14 and, at the C8 carbon signals. The positions of the signals for the other aromatic carbon atoms of the cyclophane skeleton in the two molecules are shifted by less than 1 ppm, as is also the case for the aliphatic signals of the C15 and C16 atoms situated at a larger distance from the substituent.

The presence of one or two additional aromatic rings in the cyclophane skeleton in **18** and **19**, respectively, causes considerable lowering of chemical shifts of all carbon atoms with the largest effect observed for C18, C17 and C11 of **18** (124.7 ppm, 125.2 ppm and 127.7 ppm, respectively), and practically the same lowering (to 124.6 ppm and 125.1 ppm) for C17 and C18 in **19**. Interestingly, a considerably lowered signal of the C5 atom in **18** was shifted from 130.5 ppm down to 127.3 ppm in **19**. Smaller shifts were found for the other aromatic carbon atoms. In comparison to **17**, the position of the C13 signal close to the aromatic substituent was decreased in **18** and **19**.

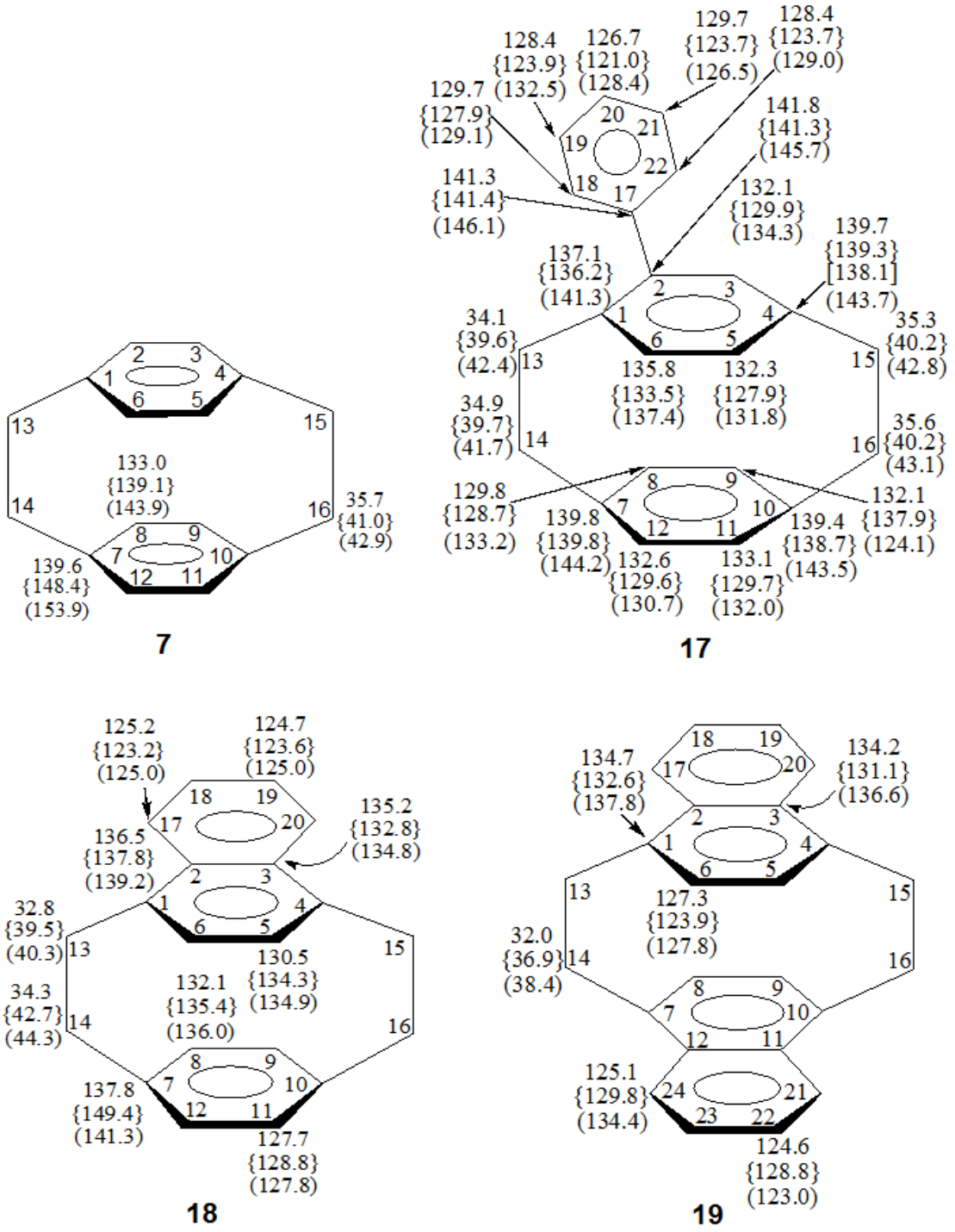

Fig. 8. ^{13}C chemical shifts (in ppm) for **7** and **17 - 19**; experimental values (this work) – no brackets, calculated using B3LYP functional are denoted by curly brackets and parenthesis for 6-311G(d,p) and Huz-IV basis sets, respectively.

Except for those chemical shift values where the differences are small, the chemical shifts calculated using the B3LYP functional together with the 6-311G(d,p) and Huz-IV basis sets roughly reproduce the trends in the experimental results. However, Huz-IV basis set yields the larger carbon chemical shift values compared of the two basis sets.

5.6. Comparison of the Calculated Chemical Shifts of Model Systems with 7

In order to analyze the influence of the aromatic ring distortion from planarity and that of the proximity of the aromatic rings in [2.2]paracyclophane on the proton and carbon chemical shifts, two series of model calculations have been carried out for the structures shown in Fig. 9. The induced chemical shifts in planar and boat-like benzene were calculated first, Table 4a. Then, the chemical shifts of the *para*-xylene dimer with distances between the aromatic rings of 3.0 Å and 4.0 Å were calculated, the results are listed in Table 4b. An inspection of these data reveals that the trends in carbon chemical shifts are correctly described by nonplanar distortions of the aromatic rings. For instance, the chemical shift of C1 in planar benzene is 133.8 ppm, whereas those of boat benzene and **7** are larger (140.6 and 139.6 ppm, respectively). The same is also true for the aliphatic carbon atoms; see for example the chemical shifts of C7 of **7** and dimer of **8** at a distance of 3.0 Å. However, the models applied are too crude to fully explain the behavior of the aromatic H2 proton chemical shifts. Moreover, the geometries of the models considered may not accurately represent the real molecular geometry.

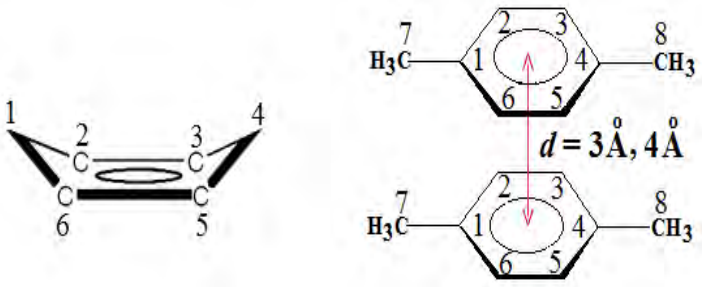

Fig. 9. Representation of the model molecules considered for comparison with **7**

Table 4a. The calculated chemical shifts ($\delta_{calc.}$, in ppm) using B3LYP/Huz-IV for planar benzene, boat benzene together with experimental values ($\delta_{exp.}$, in ppm) of planar *para*-xylene monomer **8** and **7** having boat-like aromatic rings.

	Benzene		**8**		**7**	
	planar	boat	planar		Boat-like	
	$\delta_{calc.}$	$\delta_{calc.}$	$\delta_{exp.}$	$\delta_{calc.}$	$\delta_{exp.}$	$\delta_{calc.}$
H2	7.520	7.970	7.046	7.011	6.475	6.830
H7a,[a] H13[b]	-	-	2.296[a]	2.059	3.072[b]	3.230
C1	133.8	140.6	134.7	144.3	139.6	153.9
C2	133.8	136.6	129.0	136.2	133.0	143.9
C7,[a] C13[b]	-	-	20.9[a]	21.4	35.7[b]	42.9

[a]refers to *p*-xylene **8** atom numbering, while [b]to the numbering of atoms in **7**.

Table 4b. The calculated chemical shifts ($\delta_{calc.}$, in ppm) using B3LYP/Huz-IV for *para*-xylene dimer models (with the distance (in Å) between the aromatic units *d*) together with experimental values ($\delta_{exp.}$, in ppm) of **7** and *para*-xylene monomer **8**.

	7		Dimer of **8**		**8**	
	d = 2.786 Å[c]		*d* = 3.0 Å	*d* = 4.0 Å		
	$\delta_{exp.}$	$\delta_{calc.}$	$\delta_{calc.}$	$\delta_{calc.}$	$\delta_{exp.}$	$\delta_{calc.}$
H2	6.475	6.830	8.790	5.830	7.046	7.011
H7a,[a] H13[b]	3.072[b]	3.230	2.290	1.870	2.296[a]	2.059
C1	139.6	153.9	170.6	145.9	134.7	144.3
C2	133.0	143.9	131.5	134.2	129.0	136.2
C7,[a] C13[b]	35.7[b]	42.9	37.8	24.6	20.9[a]	21.4

[a]refers to *p*-xylene **8** atom numbering, while [b]to the numbering of atoms in **7**. [c]Ref.[20]

5.7. $^2J_{HH}$ and $^3J_{HH}$ Coupling Constants

The $^2J_{HH}$ coupling constants listed Table 5 show that the results obtained for **7** and **17** using the B3LYP/Huz-IV calculations are close to the experimental values, whereas B3LYP/6-311G(d,p) gave better results for **18**, and close to the experiential values for **19** are obtained using both methods. The $^3J_{HH}$ values between the aromatic protons of **7**, **17** and **19**, listed in Table 6 together with the dihedral angles calculated at the B3LYP/cc-pVTZ level, are fairly well reproduced, with the exception of $^3J_{H5H6}$, $^3J_{H11H12}$ and $^3J_{H18H19}$ for **18**. For instance, the experimental result for $^3J_{H2H3}$ of **7** is 8.3 ± 0.1 Hz, and the corresponding calculated value using Huz-IV basis set is 8.0 Hz. On the other hand, only the experimental result for $^3J_{H8H9}$ of **18** is reproduced using the calculations, whereas the values for $^3J_{H5H6}$ and $^3J_{H11H12}$ are underestimated by about 2.7 Hz. The $^3J_{HH}$ values between the aliphatic protons involving a torsional angle close to zero value are also fairly well reproduced. For example, $^3J_{H13aH14a}$ of **7** is 10.65 ± 0.02 Hz, whereas the calculated value using Huz-IV basis set is 11.4 Hz. Similarly, $^3J_{H13aH14a}$ of **17** is 10.25 Hz and the corresponding calculated value is 10.2 Hz.

Table 5. Geminal $^2J_{HH}$ coupling constants (in Hz) between the aliphatic protons of **7**, **17**, **18** and **19**: experimental values, no brackets; and calculated values using B3LYP/6-311G(d,p), in curly brackets; and B3LYP/Huz-IV, in parenthesis.

	7		**17**		**18**		**19**	
	Exp.	Calc.	Exp.	Calc.	Exp.	Calc.	Exp.	Calc.
H13aH13b	-13.3[a]	{-11.9}	-13.68[a]	{-12.1}	-13.62[a]	{-13.1}	-13.57[a]	{-12.5}
	(-)13.1[b]	(-12.3)	(-)13.1[c]	(-12.5)		(-11.4)	(-)13.2[b]	(-12.6)
H14aH14b	-13.3[a]	{-11.9}	-13.30[a]	{-11.9}	-13.26[a]	{-11.3}	-13.57[a]	{-12.5}
	(-)13.1[b]	(-12.3)	(-)14.0[c]	(-12.3)		(-10.2)	(-)13.2[b]	(-12.6)
H15aH15b	-13.3[a]	{-11.9}	-13.26[a]	{-12.0}	-13.62[a]	{-13.1}	-13.57[a]	{-12.5}
	(-)13.1[b]	(-12.3)	(-)13.1[c]	(-12.4)		(-11.4)	(-)13.2[b]	(-12.6)
H16aH16b	-13.3[a]	{-11.9}	-13.35[a]	{-11.9}	-13.26[a]	{-11.4}	-13.57[a]	{-12.5}
	(-)13.1[b]	(-12.3)	(-)14.0[c]	(-12.4)		(-10.2)	(-)13.2[b]	(-12.6)

[a]This work. [b]Ernst *et al.*[137] [c]Kuś *et al.*[89]

The coupling constants in the aliphatic moieties between protons with a dihedral angle of ± 117° are significantly underestimated by all calculations. For example, the experimental result for $^3J_{H15aH16b}$ of **7** is 4.15 ± 0.02 Hz, whereas the calculated value using B3LYP/Huz-IV is 2.8 Hz. The corresponding experimental and calculated values for **17** are 3.56 Hz and 0.6 Hz. Similarly, the same $^3J_{H15aH16b}$ values for **18** are 6.24 Hz and 4.5 Hz. However, these coupling constants are fairly well reproduced for **19**. The results in Table 6 for the aromatic protons show that with two exceptions, the $^3J_{HH}$ values calculated using the Huz IV basis set reproduce the experimental values best, with a rms error of less than 0.4 Hz. For the 6-311G(d,p) basis set, the error is twice as large relative to the former basis set. The exceptions observed in terms of agreement with experiment involve coupling constants in the naphthalene moiety ($^3J_{H5H6}$ and $^3J_{H18H19}$) and in the aliphatic moiety ($^3J_{H13aH14b}$, $^3J_{H15aH16b}$) of **18**. The deviations of the calculated values from the experimental results exceed 2.5 Hz for the $^3J_{HH}$ in the aromatic part and around 2.0 Hz for the aliphatic parts regardless of the basis set used. Remarkably, the corresponding coupling constants of **19** are fairly well reproduced by the calculations. Since there are no practical differences between the naphthalene moieties in the optimized geometries of **18** and **19**, an inaccuracy in the geometry optimization for **18** seems not to be responsible for the discrepancy observed in the coupling constants.

In Table 7, the vicinal coupling constants in the aliphatic bridges are presented together with the theoretical values and the corresponding optimized dihedral angles. Regardless of the basis set used, the theoretical reproduction of the experimental values is rather poor, with a rms error of about 1.30 Hz for each basis set. Interestingly, for the theoretical dihedral angles the phenomenological Karplus equation[138] in its canonical parameterization by Haasnoot *et al.*[139] gives a better reproduction of the experimental values, with a rms error of 0.70 Hz only.

Table 6. $^3J_{HH}$ coupling constants (in Hz) between the aromatic protons of **7**, **17**, **18** and **19**: experimental values, no brackets; and calculated values using B3LYP/6-311G(d,p), in curly brackets; and B3LYP/Huz-IV, in parenthesis. The dihedral angles ϕ (in degrees) are calculated at the B3LYP/cc-pVTZ level.

	7			**17**			**18**			**19**		
	$^3J_{exp.}$[a]	$^3J_{calc.}$	$\phi_{calc.}$	$^3J_{exp.}$[a]	$^3J_{calc.}$	$\phi_{calc.}$	$^3J_{exp.}$[a]	$^3J_{calc.}$	$\phi_{calc.}$	$^3J_{exp.}$[a]	$^3J_{calc.}$	$\phi_{calc.}$
H2H3	8.3 ± 0.1	{7.0} (8.0)	0.0°	-	-	-	-	-	-	-	-	-
H5H6	8.3 ± 0.1	{7.0} (8.0)	0.0°	7.69	{6.9} (7.9)	0.6°	7.20	{4.3} (4.5)	0.0°	7.12	{6.8} (7.5)	0.0°
H8H9	8.3 ± 0.1	{7.0} (8.0)	0.0°	7.68	{7.2} (8.0)	0.6°	7.80	{8.0} (8.2)	0.0°	7.12	{6.8} (7.5)	0.0°
H11H12	8.3 ± 0.1	{7.0} (8.0)	0.0°	7.84	{7.0} (8.1)	0.6°	7.50	{4.6} (4.8)	0.0°	-	-	-
H17H18	-	-	-	-	-	-	8.32	{8.6} (9.1)	0.0°	8.36	{7.5} (8.5)	0.0°
H18H19	-	-	-	7.66	{6.9} (7.9)	-1.1°	6.83	{4.1} (4.3)	0.0°	6.84	{6.1} (7.1)	0.0°
H19H20	-	-	-	7.46	{6.4} (7.5)	-0.6°	8.32	{8.6} (9.1)	0.0°	8.36	{7.5} (8.5)	0.0°
H20H21	-	-	-	7.46	{6.5} (7.5)	-0.2°	-	-	-	-	-	
H21H22	-	-	-	7.66	{6.9} (7.9)	-0.5°	-	-	-	8.36	{7.5} (8.5)	0.0°

[a]This work

Table 7. $^3J_{HH}$ coupling constants (in Hz) between the aliphatic protons of **7**, **17**, **18** and **19**: experimental values, no brackets; and calculated values using B3LYP/6-311G(d,p), in curly brackets; and B3LYP/Huz-IV, in parenthesis. The dihedral angles $\phi_{calc.}$ (in degrees) are calculated using B3LYP/cc-pVTZ and the corresponding $\phi_{Karplus}$ values evaluated from Karplus equation.[56,138] $^3J_{Karplus}(\phi_{calc.})$ stands for $^3J_{HH}$ calculated from the optimized ϕ values, whereas $\phi_{Karplus}(^3J_{exp.})$ stands for the ϕ values calculated from the experimental $^3J_{HH}$ values using the Karplus equation.

	$^3J_{exp.}$	$^3J_{calc.}$	$^3J_{Karplus}$ ($\phi_{calc.}$)	$\phi_{calc.}$	$\phi_{Karplus}$ ($^3J_{exp.}$)
			7		
H13aH14a	10.65± 0.02[a]	{10.5}, (11.4)	11.04	0.0	11.0
H13aH14b	4.15 ± 0.02[a]	{2.1}, (2.6)	3.46	116.5	121.0
			17		
H13aH14a	10.25[a], 10.3[b]	{10.0}, (10.2)	10.42	13.8	16.0
H13aH14b	5.09[a], 4.7[b]	{5.3}, (6.4)	5.36	126.6	126.0
H13bH14a	3.79[a], 3.4[b]	{0.9}, (0.8)	1.51	-102.7	-118.0
H13bH14b	10.00[a], 10.0[b]	{9.7}, (10.6)	10.20	16.2	19.0
H15aH16a	10.69[a], 10.0[b]	{10.2}, (10.8)	10.49	13.0	11.0
H15aH16b	3.56[a], 3.4[b]	{0.8}, (0.6)	3.22	-115.1	-117.0
H15bH16a	4.59[a], 4.7 [b]	{4.3}, (5.5)	3.67	117.7	123.0
H15bH16b	10.63[a], 10.3[b]	{10.2}, (10.8)	10.49	13.0	12.0
			18		
H13aH14a	10.77[a]	{10.7}, (10.8)	10.62	11.4	12.0
H13aH14b	6.24[a]	{4.2}, (4.5)	5.65	128.0	131.0
H13bH14a	2.02[a]	{1.9}, (2.1)	1.60	-103.2	-106.0
H13bH14b	10.27[a]	{11.2}, (11.3)	10.47	13.3	16.0
			19		
H13aH14a	10.09[a]	{9.7}, (10.2)	9.78	20.0	18.0
H13aH14b	7.54[a]	{5.9}, (6.7)	7.09	135.0	138.0
H13bH14a	0.98[a]	{0.7}, (0.7)	0.96	-95.0	-96.0

[a]This work. [b]Ref.[89]

5.8. Temperature Effects on the J_{HH} Coupling Constants of the Bridges

As pointed out in the Introduction, in **7** there are low-frequency modes engaging the dihedral angles of the ethano-bridges. The amplitudes of the relevant motions could be rather large and would decrease with decreasing temperature. This, in turn, might be reflected in the changes of the $^3J_{HH}$ coupling constants in the bridges, due to the temperature-dependent vibrational corrections to these couplings. The measured variable-temperature NMR spectra in the range 230 - 326 K for **7**, **17**, **18** and **19** show dependence on the temperature, although these effects are generally small. Except for **19**, the values of the relevant couplings were extracted with high accuracy from fits to the spectra.

The most pronounced effect occurs for $^3J_{H13aH14b}$ in **18** whose values monotonically drop from 2.11 Hz at 326 K to 1.68 Hz at 230 K. In the same temperature interval, the values of $^3J_{H13bH14a}$ show the reverse trend with a total range of 0.23 Hz. The values of $^3J_{H13aH14a}$ and $^3J_{H13bH14b}$ also behave regularly, both decreasing with temperature by about 0.13 Hz in the interval explored. The geminal couplings $^3J_{H13aH13b}$ and $^3J_{H14aH14b}$ fluctuate in the interval of 0.04 Hz, which is less than three times the maximum standard errors delivered by the fitting program for each of these couplings (0.02 Hz in each case). In general, it was considered that a given coupling constant is temperature-independent if its total range of changes falls below three times its maximum standard error (which usually peaks at the lowest temperature investigated). In this sense, for the staggered arrangements (with the calculated torsional angles in the limits of 90^o – 135^o, Table 6) of all but two of the vicinal couplings ($^3J_{H13aH14b}$ and $^3J_{H15bH16a}$ in **17**) in the aliphatic bridges in **7**, **17** and **18** are temperature-dependent. In **19**, the situation is unclear because the total ranges of the change barely exceed the assumed thresholds. For the nearly-eclipsed positioning of the CH bonds (calculated torsional angles $\leq 20^o$), except for $^3J_{H13aH14a}$ in **19**, and $^3J_{H15aH16a}$ and $^3J_{H15bH16b}$ in **17**, all of the remaining vicinal couplings show a small but consistent reduction with increasing temperature, by 0.12 to 0.20 Hz in total. This must be considered to be a real effect considering the small values less than 0.02 Hz, of the standard errors obtained. Except for $^2J_{H16aH16b}$ in **17**, the geminal couplings in **17** - **19** are temperature-independent, as are the aromatic J_{HH} couplings in these compounds. The geminal $^2J_{HH}$ and aromatic $^3J_{HH}$ coupling constants in **7** could not be measured with sufficient accuracy to assess their temperature dependence.

The observed temperature dependences confirm unequivocally the existence of at least one low-frequency mode in **7**, **17** and **18** that affects the values of the vicinal J_{HH} couplings in the aliphatic bridges, leaving the remaining J_{HH} couplings insensitive to temperature. For the eclipsed arrangements, the Karplus curve has a local maximum of about 11 Hz. Therefore, a consistent drop with increasing temperature of the vicinal couplings for the (nearly) eclipsed pairs of CH bonds would mean a progressive opening of the corresponding dihedral angles. Such a behavior could be affected by the twisting-rocking mode shown in Fig. 2.

5.9. $^1J_{CH}$ and $^1J_{CC}$ Coupling Constants

The experimental and calculated (using B3LYP/6-311G(d,p) and B3LYP/Huz-IV) values of $^1J_{CH}$ and $^1J_{CC}$ coupling constants are presented in Figs. 10 and 11, respectively. The experimental results for the $^1J_{CH}$ values of the aromatic protons of the cyclophane skeleton (Fig. 10) are only slightly changed within the series of molecules. Small, but significant, differences between experimental and calculated values using the Huz-IV basis set of the aromatic $^1J_{CH}$ of less than *ca.* 6.0 Hz for $^1J_{C8H8}$, $^1J_{C9H9}$, $^1J_{C11H11}$, $^1J_{C12H12}$, $^1J_{C18H18}$ for **17**, *ca*. 4.0 Hz for the $^1J_{C17H17}$, $^1J_{C8H8}$, $^1J_{C9H9}$, $^1J_{C19H19}$ couplings for **18**, and *ca.* 5.0 Hz for the $^1J_{C17H17}$, $^1J_{C18H18}$ for **19** have been observed. For the experimental values of the coupling constants involving the aliphatic protons, there are only small changes of less than 3 Hz within the series **7**, **17**, **18** and **19**, with practically no difference between the $^1J_{C13H13}$ values for **7** and **19**. Small but significant differences have been observed between the spin-spin coupling constants involving C14 in **17** and **19**.

All calculated values of $^1J_{CH}$ are lower than the experimental ones. In most cases the values calculated using the Huz-IV basis set are the largest; the calculations with the other basis set do not show such a well-defined trend. With very few exceptions ($^1J_{C9H9}$ in **18** and $^1J_{C17H17}$ in **19**), the Huz-IV values reproduce the experimental data much better than the values calculated using the other basis set. For the aliphatic bonds, the 6-311G(d,p) basis set sometimes reproduces the experimental values better, but the differences between the Huz-IV and the latter basis set are small. This is in agreement with the known observation of spin-spin coupling constants being much more sensitive to the quality of the basis set used than are the nuclear shielding constants.[55]

No carbon-carbon coupling constants through one bond could be measured for **17** (see $^1J_{CC}$ in Fig. 11). Also for **18** and **19**, some constants could not be determined. Of the measured coupling constants of **18**, high values were measured for the $^1J_{C1C2}$, $^1J_{C1C6}$, $^1J_{C2C17}$ and $^1J_{C17C18}$ couplings.

Interestingly, in contrast to most observations of $^1J_{CH}$, the measured values are not always larger than the calculated ones. No significant differences of more than *ca.* 1 Hz in the calculated values of $^1J_{CC}$ coupling constants between **7** and **17** have been found. Somewhat surprisingly, the large values of *ca.* 78.8, 76.9 and 70.7 Hz of $^1J_{C9C10}$, $^1J_{C11C12}$ and $^1J_{C2C3}$, respectively, for **18** were calculated using the 6-311G(d,p) basis set, with considerably smaller value for the $^1J_{C9C10}$ coupling constant and larger values for the other coupling constants all obtained using Huz-IV. Interestingly, the calculated values of $^1J_{C2C3}$ for **19** were lower than 60 Hz. Similarly, the calculated values involving $^1J_{C5C6}$, $^1J_{C8C9}$ and $^1J_{C18C19}$ in **18** dropped below 50 Hz, while the corresponding values for **7** and **17** fall above 60 Hz.

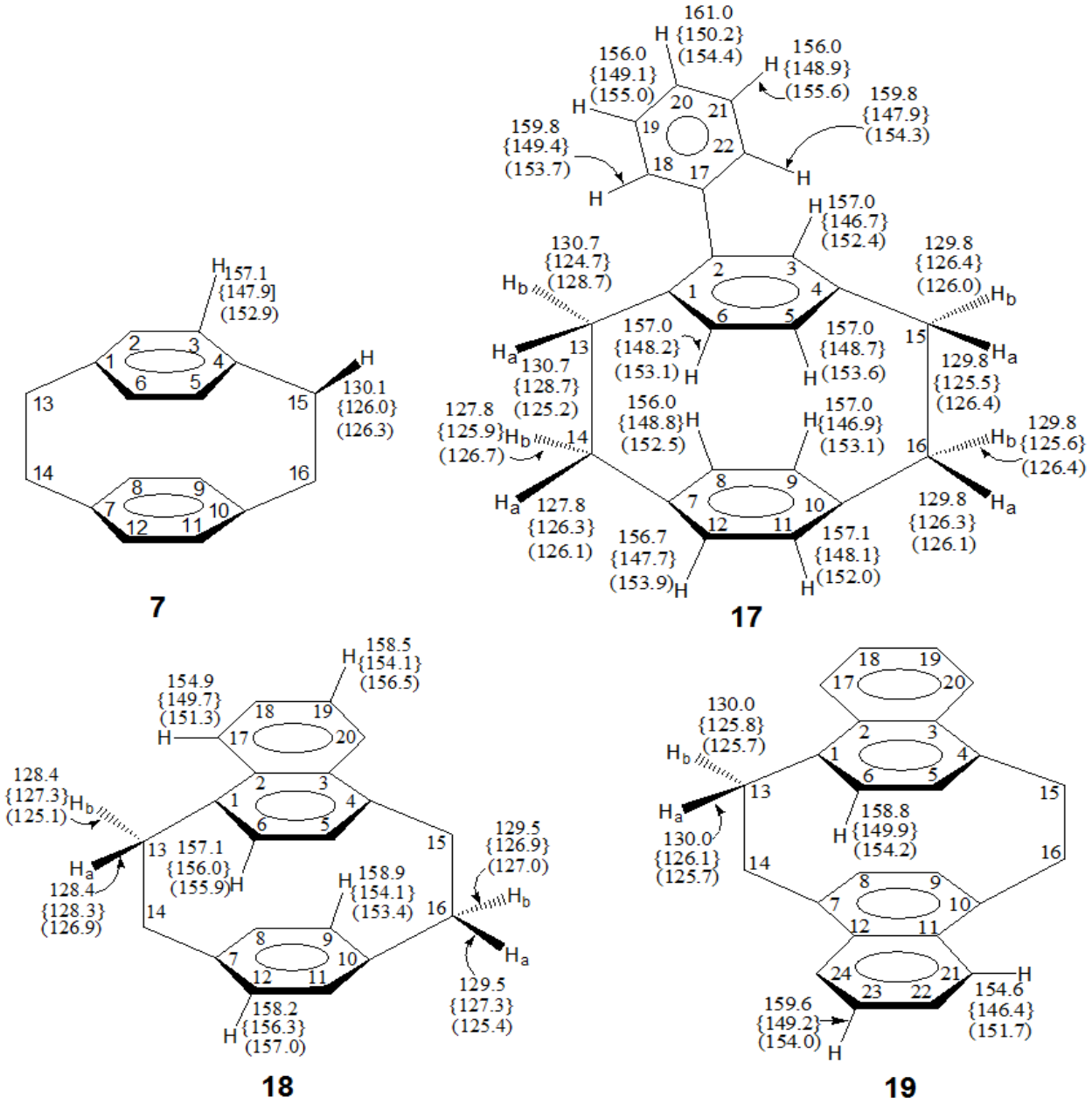

Fig. 10. $^{1}J_{CH}$ coupling constants (in Hz) for **7**, **17**, **18** and **19**; experimental values (this work) – no brackets, calculated using B3LYP functional are denoted by curly brackets and parenthesis for 6-311G(d,p) and Huz-IV basis sets, respectively.

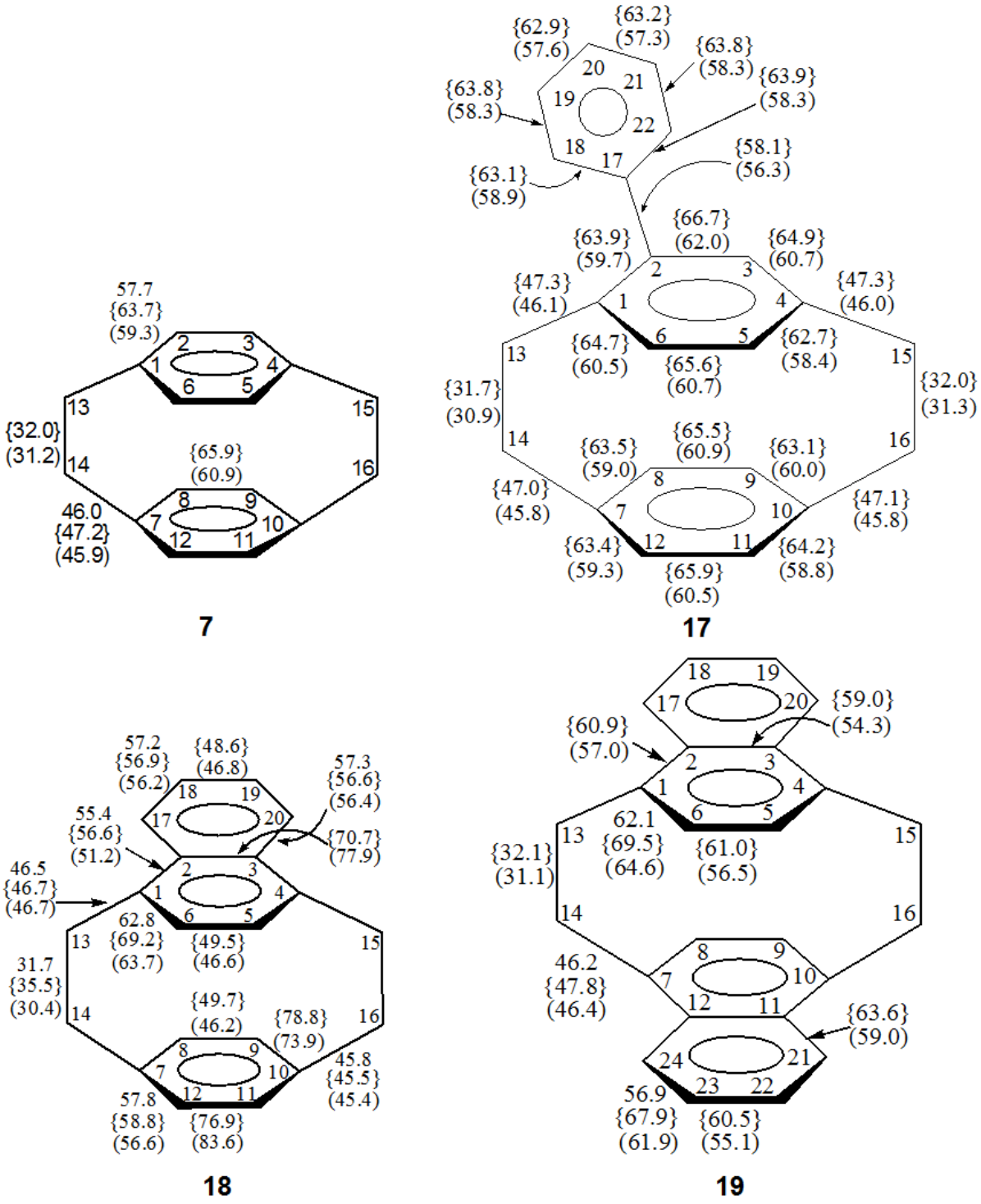

Fig. 11. $^{1}J_{CC}$ coupling constants (in Hz) for **7**, **17**, **18** and **19**; experimental values (this work) – no brackets, calculated using B3LYP functional are denoted by curly brackets and parenthesis for 6-311G(d,p) and Huz-IV basis sets, respectively.

5.10. Conclusion

The optimized structure of **7** using B3LYP functional resulted in D_{2h} symmetry that agrees with the low-temperature X-ray results reported by the Lyssenko group.[20] However, the twist angle obtained from the B3LYP optimized geometry is in strong disagreement with most published calculated results.[14,22] In view of the probable occurrence of a low-frequency mode in **7**, it is difficult to resolve whether the molecule has the D_{2h} eclipsed or D_2 twisted structure. The re-examination of the X-ray structure of **7** at different temperatures seems a basic solution for the vivid discussions in most of the theoretical works. The NMR calculations reveal that, in most cases, the 6-311G(d,p) basis set reproduces fairly well the proton chemical shifts. However, such a simple conclusion could not be drawn for the carbon chemical shifts. On the other hand, with regard to the coupling constants, Huz-IV gave the most accurate values compared to the former basis set with the exception for the values for $^1J_{C13H13a}$, $^1J_{C14H14}$a and $^1J_{C16H16a}$ of **17**. The carbon and aliphatic proton chemical shifts are influenced by nonplanar benzene ring distortions and the proximity of the rings. In **7**, **17** and **18**, the measured values for the vicinal coupling constants in the aliphatic bridges were found to be temperature dependent. This provides one argument for the occurrence of a low-frequency twisting/rocking mode in these compounds complicating the determination of the molecular geometry. Based on this observation and analysis, a comparison of the optimized geometries of these compounds with their X-ray structures may be misleading, since the crystal-packing forces might substantially modify the extent of the mutual twist of the molecular moieties.

Chapter 6
Cyclophanes with Unsaturated Bridges (Cyclophenes)

6.1. Introduction

As discussed in Chapters 1 and 5, the interfacial crowding of the two aromatic rings of **7** is one of the responsible factors for its unusual chemistry. If the two benzene rings are brought face to face with unsaturated bonds in the bridges, for instance like **9**[1,124] and **20**,[124] the interfacial crowding of the rings is even more intense.[140-143] Similarly, if the benzene rings are brought face to face with three ethyl bridges located at the 1, 3 and 5 positions as in **33**, the deformation of the rings becomes stronger than in **7**, which also cause the strong interfacial crowding of the aromatic rings. Moreover, the influence of unsaturated bridges roughly perpendicular to the plane of the aromatic rings on the physicochemical properties of cyclophanes is exciting in view of possible, although weak, interaction of π-electrons of the bridge(s) with those of the aromatic rings. Therefore, the cyclophanes with unsaturated bridge(s) are also an interesting class of organic molecules because of their unusual properties as was also the case for the molecules discussed in Chapter 5.

The shortest distance between the two benzene rings (C1…C7 and C4…C10) of **7** is 2.786 Å,[20] which is not only shorter than the separation distance between the stacked aromatic molecules but also than the sum of two carbon atoms van der Waals radius, 3.4 Å. The introduction of shorter unsaturated bridges is expected to decrease the distance between the aromatic rings in comparison to their saturated analogues. This has been observed in **9** which has a C1…C7 distance of 2.783 Å,[124] slightly decreased compared to **7** (2.786 Å).[20] In addition, incorporating a third bridge is also expected to further affect the separation distance between the aromatic rings. For instance, the shortest distance between the non-bonded carbon atoms of [2.2.2](1,3,5)cyclophane **33** is 2.790 Å,[144] while that of [2.2.2](1,3,5)cyclophan-13,15,17-triene **34** is 2.740 Å[140] (the distance between the non-bridging carbon atoms is 2.860 Å). These distances show that the two benzene rings are in a considerably stronger face-to-face crowding than in **7**. For [2.2]paracyclophan-13,15-diene **9** the shortest distance between the bridgehead

carbon atoms is 2.800 Å.[124] This short separation distance between the benzene rings causes lengthening of the bridge $C_{sp3}C_{sp3}$ bonds. For instance, C13C14 of **7** is 1.579 Å, whereas that of **33** is 1.600 Å.[144] The other consequence is the $C_{sp2}C_{sp2}$ double bond length of the unsaturated bridges, which is shorter than those of the aromatic ring bonds, 1.340 Å for the unsaturated bridge and 1.396 Å for the aromatic $C_{sp2}C_{sp2}$ bonds of **9**.[124,140]

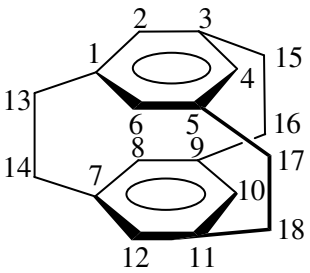

33

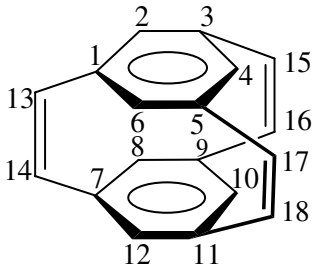

34

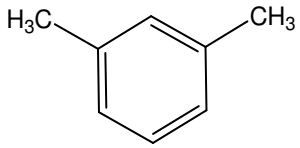

35

The unusually deformed aromatic rings cause the aromatic hydrogen atoms to be much closer to the center area between the rings and out of the average plane of the rings. Assuming planar benzene rings, the separation of the hydrogen atoms from the two aromatic rings would be expected to be about 3.010 Å. However, this is not the case for **34**, it is only 2.520 Å.[140] These types of structural abnormalities cause remarkable changes in the spectroscopic properties of the molecules. Among these, NMR is one of the sensitive tools for analyzing the structure of the molecules.

As is well known, ^{1}H NMR spectroscopy can give detailed information about the structure of molecules like cyclophanes; for example about unusual chemical shifts of protons lying above/below the plane of the aromatic rings. These kinds of unusual properties could be related to the number of ethylene bridges connecting the rings as well as the type of the bridge bonds. For example, the protons of *meta*-[2.2]cyclophane **6** experience strong shielding with a value of 4.26 ppm as compared to 1,3-dimethyl benzene **35** with a chemical shift of 7.02 ppm for the aromatic protons between the two methyl substituents. This is because the protons in **6** are situated much closer to the center of the opposite aromatic ring.

The synthesis of **9** was reported by Dewhirst *et al.*[145] along with other classically conjugated cyclophanes. X-ray data for the structure of **9** and **20** have been reported by de Meijere *et al.*[124] and those of **21** by Heilbronner *et al.*[146] Unfortunately, the experimental structural results for **20**

obtained by de Meijere *et al.*[124] yielded two independent molecules in a unit cell. One of these was disordered, and hence only the data of the second molecule was compared with those of the optimized geometries.

Dodziuk *et al.*[33] carried out computational and experimental studies of the NMR, electronic absorption and magnetic circular dichroism spectra[37] of **29** together with those of other related cyclophanes. Ionization potentials of **9**, **20** and **21**, determined by photoelectron spectroscopy, were reviewed by Heilbronner and Yang.[146] Their ultraviolet spectra were reported by Dewhirst and Cram[145] and the heats of formation of **9** and **20** were reported by de Meijere *et al.*[124] Chemical shifts and a few coupling constants of the known cyclophanes were reported together with their synthesis.[124,146] However, there are no calculations on cyclophanes with unsaturated bridges in the literature. In addition, literature and structural searches indicate that molecules **24** - **28** are hypothetical, whereas the other cyclophanes with unsaturated bridges are known. Hence, in this chapter the studies of cyclophanes with unsaturated bridges, **9** and **20** – **28**, are presented with **7** and **29** added for comparison. For the sake of simplicity, the results and discussion part is presented in three sub-sections, 6.2, 6.3, and 6.4 for the geometries, and 6.5, 6.6, and 6.7 for the NMR parameters.

6.2. Geometry of 7, 9, 20 and 21

The available experimental and calculated bond lengths are presented in Fig. 12. In Chapter 5, the details of the structural properties of **7** have already been discussed. However, for the sake of comparison, it is re-considered in this part of the PhD dissertation. For **7**, **9**, and **20** the bond lengths calculated using ωB97X-D/cc-pVQZ are in agreement with the available experimental results except for the $C_{sp^3}C_{sp^3}$ bond lengths and C1C13C14C7 torsional angle discussed in detail earlier. The bond lengths calculated using the ωB97X-D functional in **7** and **20** are considerably better than those obtained using B3LYP functional. However, they are still too large by more than 0.01 Å for **7**. The $C_{sp^2}C_{sp^2}$ bond lengths are reasonably well reproduced by the calculations. In most cases, the differences among the calculated and experimental values are too small to allow one for a definite statement on the quality of the functionals/basis sets used. It is also noted that there is a considerable error in the experimental and calculated $C_{sp^2}C_{sp^2}$ bridge bond lengths in **9** calculated at the B3LYP/6-311++G(2d,2p) level and those in **20** obtained at the ωB97X-

D/6-311++G(2d,2p) level. In spite of the similarity of the aromatic bond lengths in the molecules under scrutiny, in most cases the trends in bond lengths are reproduced by the calculations.

Almost all aromatic rings bond lengths and the $C_{sp2}C_{sp3}$ bridge bond lengths are close to the standard aromatic and $C_{sp2}C_{sp3}$ bond length values of 1.400 Å[147,148] and 1.510 Å,[147] respectively. The calculated value of the $C_{sp2}C_{sp2}$ single bond in **21** (C13C17) using B3LYP/6-311++G(2d,2p), 1.460 Å, is very close to the length of the central bond in butadiene.[147]

The distances between the corresponding atoms of the two aromatic rings of **7**, **9**, **20** and **21** are collected in Table 8. In agreement with expectations, the results indicate that the aromatic rings have a boat conformation with the respective bridgehead carbon atoms being closer to each other. Except for the C1…C7 distance calculated at the ωB97X-D/cc-pVQZ level, all calculated results are overestimated compared to the corresponding experimental values. The results calculated at the ωB97X-D/cc-pVQZ level are closer to the experimental ones than those calculated using the B3LYP functional. This could be due to the over-repulsive character of the functional in the van der Waals distance regime. This further resulted in a lengthening of the $C_{sp3}C_{sp3}$ bridge-bonds in **7**, **20** and **21**. There are also large differences between the calculated and experimental results for the $C_{sp3}C_{sp3}$ bond lengths, as well as between the calculated results themselves, which probably is also due to the overestimation of the repulsion between the aromatic rings by the B3LYP functional. However, the values calculated using ωB97X-D/cc-pVQZ are much closer to the experimental data than those obtained using the other method. This is due to the fact that the functional is dispersion corrected and describes well the dispersive interactions between the aromatic rings. As expected, both the calculated and experimental values show that the introduction of a double bond in **20** causes a decrease of the C1…C7 distance and an increase of the C5…C11 and C6…C12 distances while, somewhat surprisingly, the introduction of two unsaturated bonds in the two bridges of **9** yields values of the C1…C7 and C4…C10 distances closer to the value in the saturated molecule **7** (Table 8).

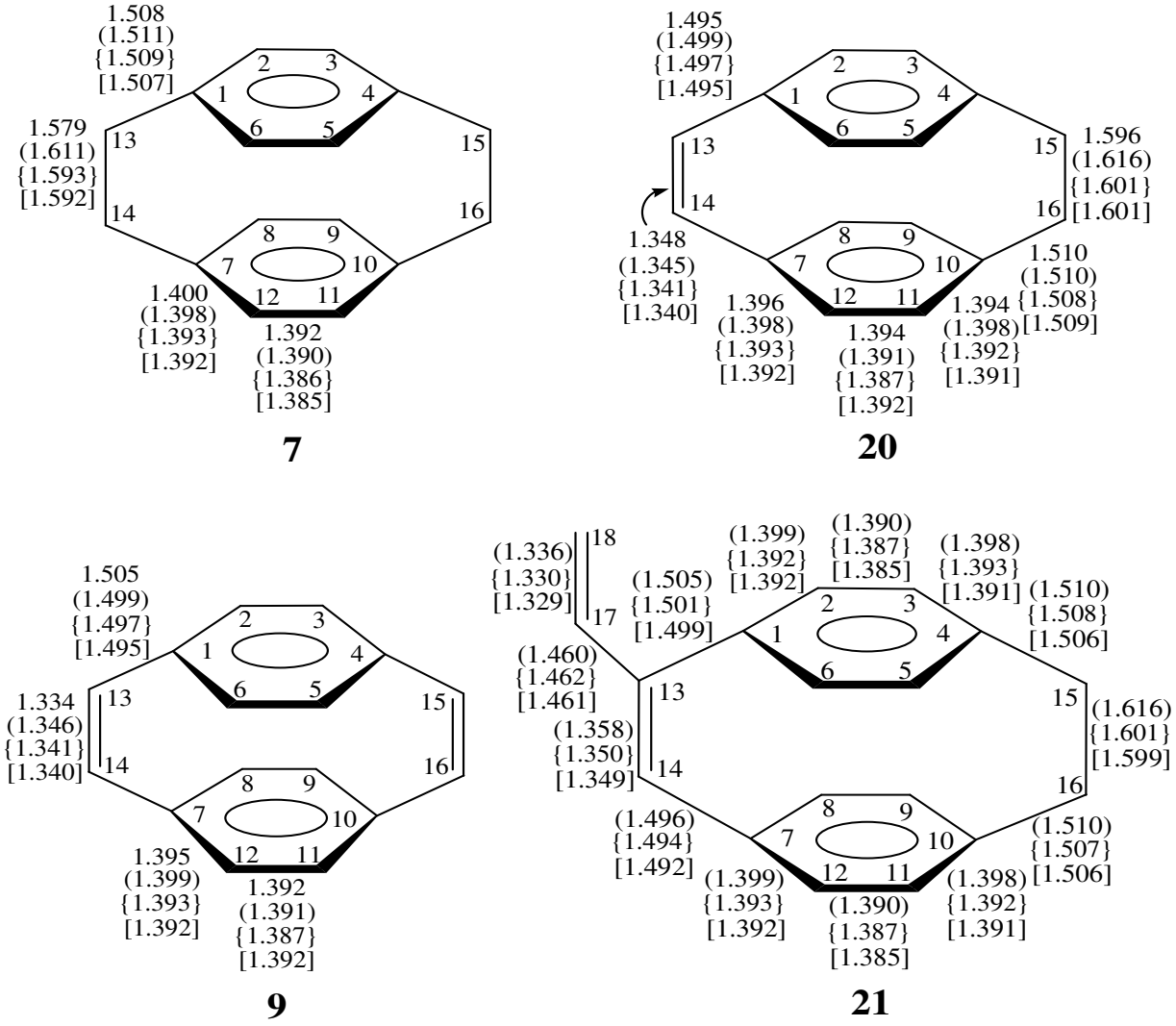

Fig. 12. Bond lengths (in Å): experimental values for **7**,[20] **9**,[124] **20**[124] with no brackets; and calculated values for **7**, **9**, **20** and **21** using B3LYP/6-311++G(2d,2p), in parenthesis; ωB97X-D/6-311++G(2d,2p), in curly brackets; and ωB97X-D/cc-pVQZ, in square brackets.

Table 8. Distances (in Å) between the non-bonded carbon atoms of the two aromatic rings in **7**, **9**, **20** and **21**: experimental values, with no brackets; and calculated values using B3LYP/6-311++G(2d,2p), in parenthesis; ωB97X-D/cc-pVQZ, in square brackets.

	7		**20**		**9**		**21**
	Exp.[20]	Calc.	Exp.[124]	Calc.	Exp.[124]	Calc.	Calc.
C1…C7	2.786	(2.828)	2.760	(2.809)	2.783	(2.833)	(2.798)
		[2.797]		[2.779]		[2.798]	[2.768]
C2…C8	3.099	(3.156)	3.100	(3.166)	3.101	(3.196)	(3.153)
		[3.113]		[3.115]		[3.143]	[3.108]
C3…C9	3.099	(3.156)	3.127	(3.187)	3.101	(3.196)	(3.179)
		[3.113]		[3.133]		[3.143]	[3.129]
C4…C10	2.786	(2.828)	2.811	(2.854)	2.783	(2.833)	(2.850)
		[2.797]		[2.815]		[2.798]	[2.812]

The bond and torsional angles are collected in Annex 1. Except for some bond angles **9** (where the differences between experimental and calculated values are less than 4°) and a few torsional angles, the available experimental values are reproduced very well, and none of the computational methods gave significantly better results than the others. The only significant exceptions are the zero degree calculated values of the C1C13C14C7 (and by symmetry C4C15C16C10) twist angle of **7** using the B3LYP functional. However, the ωB97X-D functional gave approximately -15° regardless of the choice of basis set even though the experimental value reported by Lyssenko *et al*. is 0°,[20] and by Hope *et al.* is 6.4°.[23,128]

6.3. Geometry of 22 – 24 and 29

The calculated and available experimental bond lengths are presented in Fig. 13. For **29** two independent molecules, **29a** or **29b**, in a unit cell yielded considerably different parameters. Hence, it is not clear whether **29a** or **29b** should be compared with the theoretical results for this molecule, which makes the comparisons difficult. With the exception of the C13C14 bond in one molecule of **29**, the calculated values of the saturated $C_{sp3}C_{sp3}$ bridge bonds are slightly longer, but comparable to the experimental values. These values of *ca*. 1.60 Å, larger than those in **7** and **20**, is the largest observed extensions of the $C_{sp3}C_{sp3}$ bond. The calculated $C_{sp2}C_{sp2}$ bridge bond lengths in **23** are very close to the standard double bond length,[147] while the bonds in **22** and **24**

are slightly extended. All calculated and available experimental $C_{sp2}C_{sp3}$ bond lengths have very similar values of *ca*. 1.51 Å, whereas the corresponding $C_{sp2}C_{sp2}$ bonds between a double bond and the aromatic ring are smaller, 1.495 - 1.498 Å.

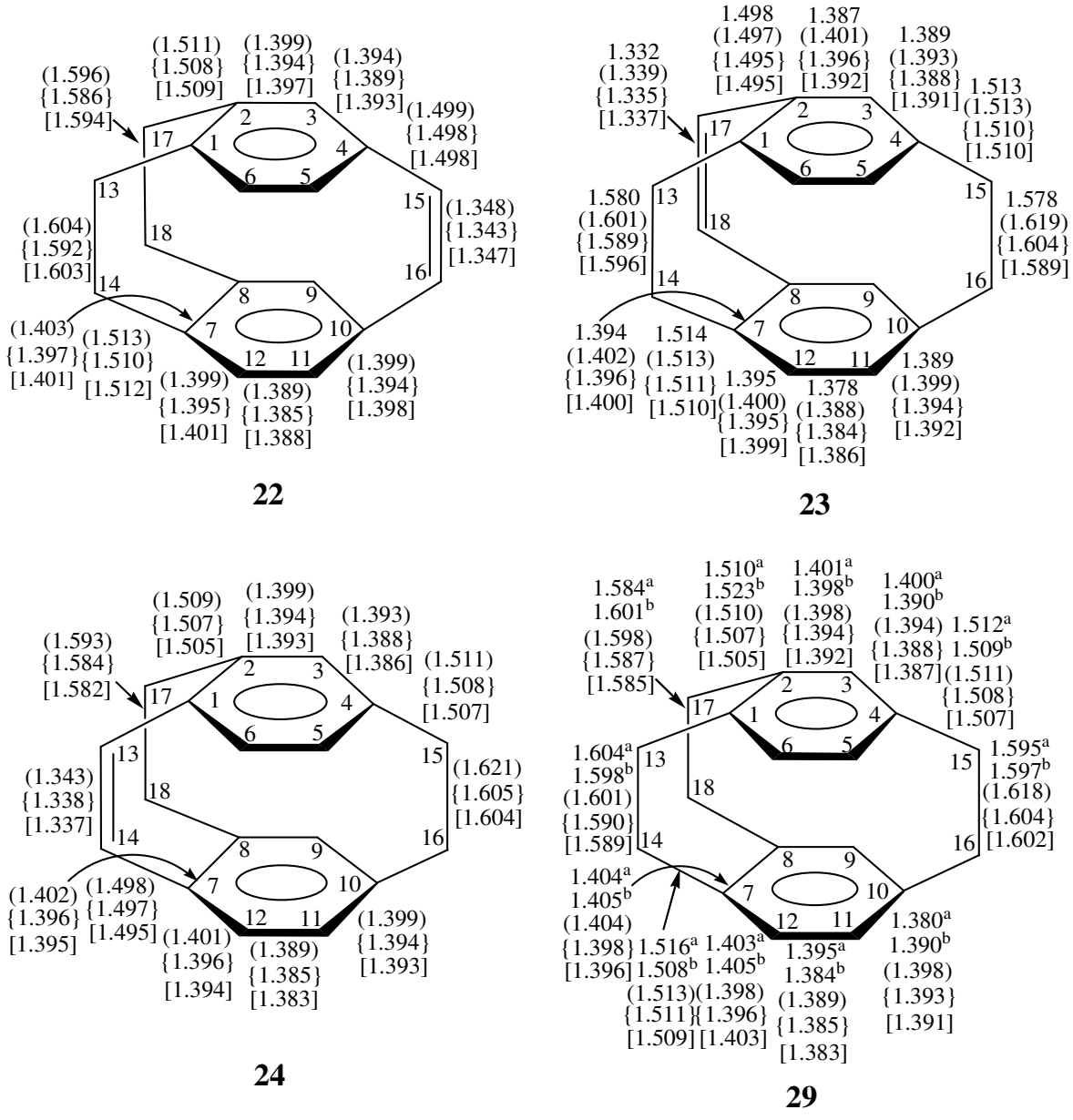

Fig. 13. Bond lengths (in Å) for **22** – **24** and **29**: experimental values for **23**[93] and **29**,[149] with no brackets; calculated using B3LYP/6-311++G(2d,2p), in parenthesis; ωB97X-D/6-

311++G(2d,2p), in curly brackets; and ωB97X-D/cc-pVQZ, in square brackets. (Since for **29** two molecules are present in the unit cell, two kinds of values are given and labeled as a and b).

The distances between the non-bonded carbon atoms between the two aromatic rings are listed in Table 9. Understandably, the C1…C7, C2…C8, C3…C9 and C4…C10 distances are considerably smaller than the sum of the van der Waals radius of the carbon atoms with the C1…C7 distance in **23** and **29** slightly shorter compared to that of **7**. All calculated values for **23** and **29** are larger than the available experimental results. Except for the C5…C11 and C6…C12 distances for which the calculated results are very poor, the differences between the calculated and experimental values are smaller than 0.06 Å. As found for the molecules discussed in section 6.2, the values obtained from the ωB97X-D/cc-pVQZ optimization are closer to the experimental results than those obtained from the other method.

Table 9. Distance (in Å) between the non-bonded carbon atoms of the two aromatic rings for **22** – **24** and **29** calculated using B3LYP/6-311++G(2d,2p), in parenthesis; ωB97X-D/cc-pVQZ, in square brackets; and experimental values, with no brackets.

	22	**23**		**24**		**29**	
	Calc.	Exp.[93]	Calc.	Calc.	Exp. **29a**[149]	Exp. **29b**[149]	Calc.
C1…C7	(2.792)	2.737	(2.788)	(2.761)	2.725	2.737	(2.765)
	[2.789]		[2.755]	[2.733]			[2.737]
C2…C8	(2.699)	2.657	(2.679)	(2.696)	2.668	2.661	(2.690)
	[2.695]		[2.664]	[2.677]			[2.668]
C3…C9	(2.842)	2.831	(2.870)	(2.875)	2.816	2.828	(2.862)
	[2.838]		[2.856]	[2.852]			[2.837]
C4…C10	(2.825)	2.807	(2.863)	(2.860)	2.801	2.796	(2.842)
	[2.823]		[2.854]	[2.821]			[2.806]
C5…C11	(3.435)	3.279	(3.416)	(3.425)	3.269	3.275	(3.377)
	[3.434]		[3.404]	[3.343]			[3.305]
C6…C12	(3.474)	3.325	(3.457)	(3.447)	3.303	3.314	(3.408)
	[3.473]		[3.356]	[3.367]			[3.339]

Note: There are two molecules of compound **29** (designated **29a** and **29b**) in the unit cell.

The available and calculated values of bond and torsional angles are collected in Annex 2. Inspection of the results shows that most of the experimental bond angles are reproduced with satisfactory accuracy by the calculations. The values obtained using ωB97X-D/cc-pVQZ are usually closer to the experimental results, although the differences with the other methods is not

large. However, this is not the case for some torsional angles involving bridges of **29**, in which the errors exceed 10^{o} for the C4C15C16C10 and, in one case, C3C4C15C16 angles; and exceed 5^{o} for the C1C13C14C7 and C2C17C18C8 torsional angles and is close to 5^{o} for C4C15C16C10 of **23**.

6.4. Geometry of 25 – 28

The calculated bond lengths are presented in Fig. 14. For these molecules, no experimental geometries have been reported. As expected, the calculated bond lengths exhibit a lengthening of the $C_{sp3}C_{sp3}$ bonds compared to the standard bond lengths, whereas the $C_{sp2}C_{sp3}$ bridge bonds are slightly longer than the $C_{sp2}C_{sp2}$ bonds. Also as expected and in agreement with the findings for the molecules discussed in sections 6.2 and 6.3, the distances between non-bonded atoms of the aromatic rings (Table 10) are larger when the atoms are not connected by a bridge. The C2…C8 distance is considerably shorter than the distance between the other bridgehead carbon atoms. Interestingly, the C5…C11 and C6…C12 distances are close to or larger than the sum of van der Waals radii of two carbon atoms. The C3…C9 distance is shorter than C5…C11 and C6…C12, making the average plane of the rings to be non-parallel. The values of distances calculated at the B3LYP/6-311++G(2d,2p) and ωB97X-D/cc-pVQZ levels differ sometimes by more than 0.1 Å, whereas the corresponding bond and torsional angles, listed in Annex 3, differ by less than 1^{o}.

Table 10. Distances (in Å) between non-bonded carbon atoms in **25** – **28** calculated using B3LYP/6-311++G(2d,2p), in parenthesis; ωB97X-D/6-311++G(2d,2p), in curly brackets, and ωB97X-D/cc-pVQZ, in square brackets.

	25	**26**	**27**	**28**
C1…C7	(2.789)	(2.779)	(2.814)	(2.810)
	{2.758}	{2.752}	{2.781}	{2.774}
	[2.755]	[2.749]	[2.777]	[2.771]
C2…C8	(2.701)	(2.679)	(2.688)	(2.683)
	{2.692}	{2.668}	{2.676}	{2.676}
	[2.687]	[2.663]	[2.672]	[2.671]
C3…C9	(2.845)	(2.892)	(2.849)	(2.859)
	{2.842}	{2.874}	{2.842}	{2.856}
	[2.838]	[2.869]	[2.838]	[2.852]
C4…C10	(2.844)	(2.887)	(2.846)	(2.873)
	{2.811}	{2.847}	{2.813}	{2.834}
	[2.808]	[2.844]	[2.809]	[2.830]
C5…C11	(3.509)	(3.484)	(3.476)	(3.578)
	{3.399}	{3.391}	{3.377}	{3.453}
	[3.396]	[3.387]	[3.374]	[3.448]
C6…C12	(3.538)	(3.522)	(3.526)	(3.623)
	{3.433}	{3.432}	{3.433}	{3.502}
	[3.430]	[3.429]	[3.429]	[3.499]

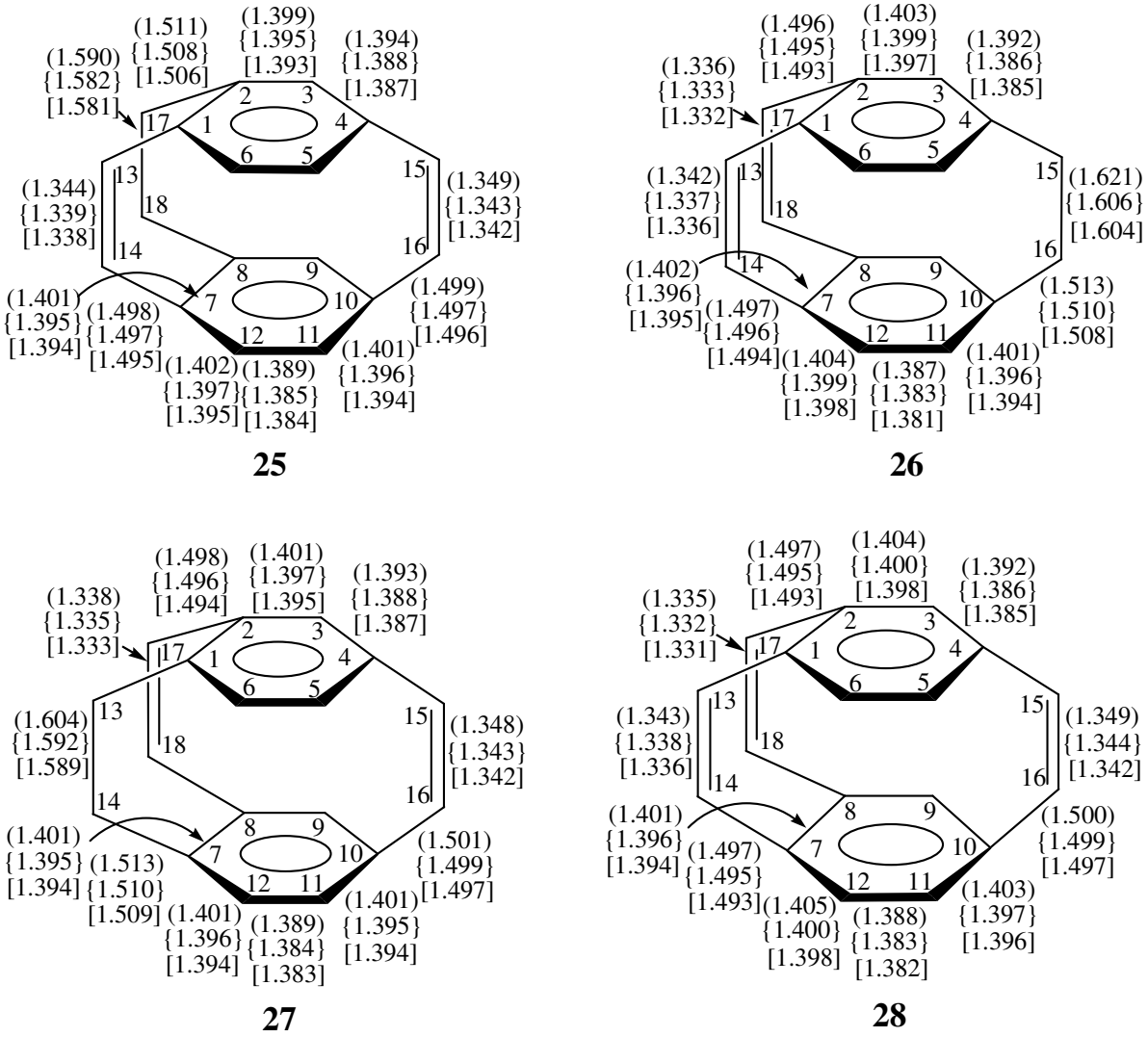

Fig. 14. Bond lengths (in Å) for **25** - **28**: calculated using B3LYP/6-311++G(2d,2p), in parenthesis; ωB97X-D/6-311++G(2d,2p), in curly brackets; and ωB97X-D/cc-pVQZ, in square brackets.

6.5. NMR Parameters of 7, 9, 20 and 21

The proton chemical shifts for the molecules under study are collected in Fig. 15. Except for small chemical shift differences, all the calculated values reproduce experimental trends, for instance see the results of **21**. Moreover, the experimental values for protons connected to C_{sp3} atoms are quite accurately reproduced by the calculations. On the other hand, the calculated

values for all other protons are usually overestimated by 0.2 - 0.5 Hz. With the exception of the chemical shift values of the methylene protons (H15 and H16) in **20** and **21**, the experimental and calculated values of the chemical shifts differ considerably. For example, the difference between the calculated and experimental values for the chemical shift of H13 in **9** is 0.4 - 0.5 ppm based on the type of functional used. The chemical shifts of protons attached to the sp^3 carbon atoms of the bridges are always shifted downfield from the experimental results, with the exception of those calculated using B3LYP/Huz-IV for **20** and **21**, and those using ωB97X-D/6-311++G(2d,2p) for **7** with the maximum deviation between the experimental and ωB97X-D/cc-pVQZ calculated values of the chemical shifts for H13 of **9** which exceeds 0.6 ppm and H12 in **7** and H13 in **20** which are larger than 0.5 ppm. The effects observed cannot be attributed to the errors in the optimized geometry since the method gave considerably improved calculated bond lengths of the bridge $C_{sp3}C_{sp3}$ bond lengths. In certain cases, such as H12 in **7**, ωB97X-D/cc-pVQZ yielded the worst calculated values of the chemical shifts despite its computational cost.

The calculated and available ^{13}C chemical shifts of **7**, **9**, **20** and **21** are listed in Fig. 16. The calculations gave results that have considerably higher values for the ^{13}C chemical shifts compared to the experimental data. Except for the C17 and C18 chemical shifts in **21**, the results calculated using B3LYP/6-311++G(2d,2p) reproduce experimental data best. With the exception of the close-lying chemical shift values, (for instance, some of those for C1 and C13 in **9** and **20**, and C1 and C4 in **21**), most calculated results reproduce the experimental trends. Except for the saturated bridge carbon atoms, almost all values calculated at the ωB97X-D/cc-pVQZ level have the largest errors compared to ωB97X-D/6-311++G(2d,2p) as it can be seen from Fig. 16.

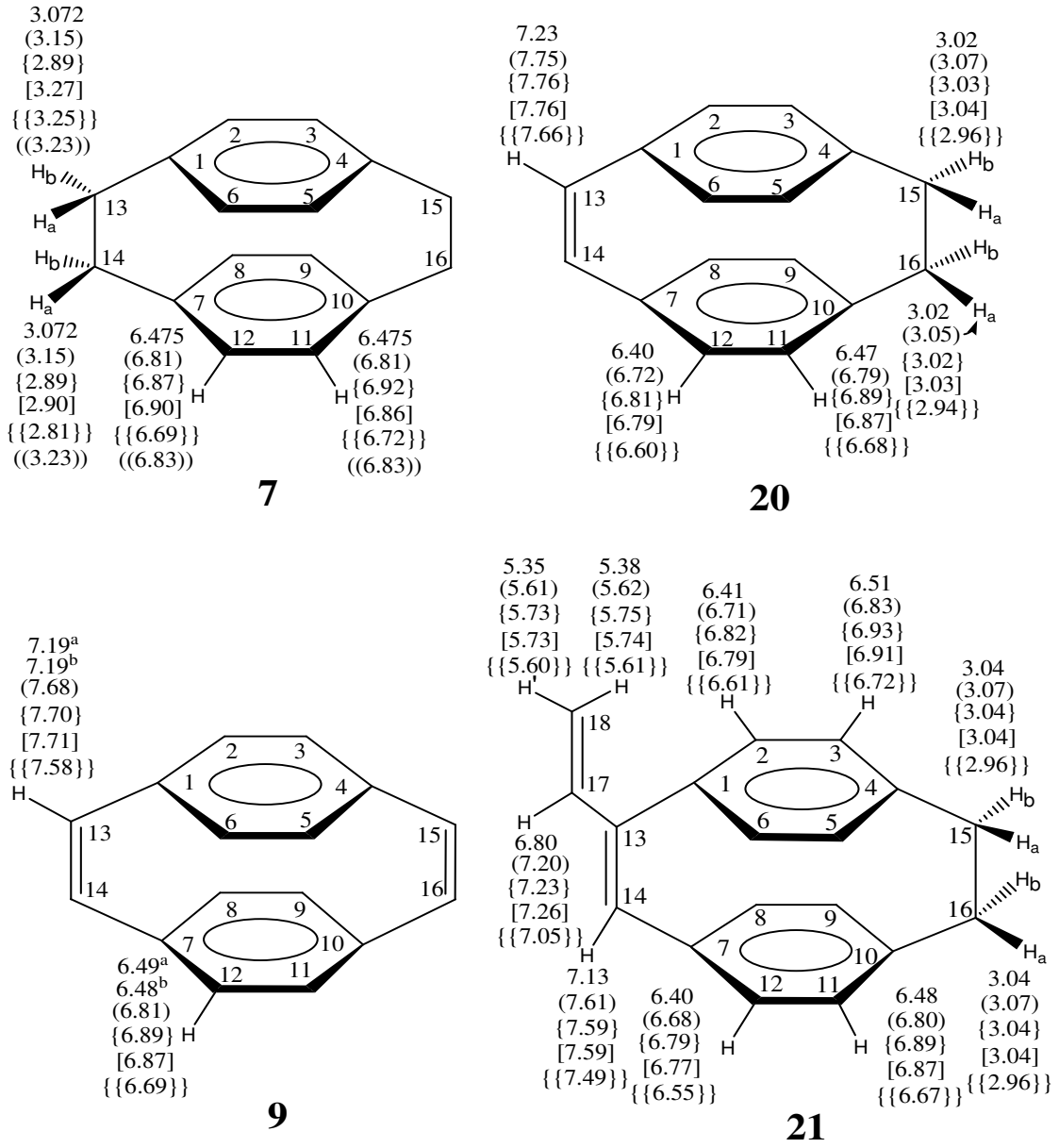

Fig. 15. ^{1}H chemical shifts (in ppm) for **7**, **9**, **20** and **21**: experimental values (this work), no brackets; calculated using B3LYP/6-311++G(2d,2p), in parenthesis; ωB97X-D/6-311++G(2d,2p), in curly brackets; ωB97X-D/cc-pVQZ, in square brackets; B3LYP/6-311G(d,p) on the structure optimized at ωB97X-D/cc-pVQZ, in double curly brackets; and B3LYP/Huz-IV, in double parenthesis (Exp. for **7**, **20**, **21** - this work, for **9** "a" - this work, "b" – Ref[150]). The "a' and "b" subscripts refer to protons pointing out of the plane and inside the plane, respectively.

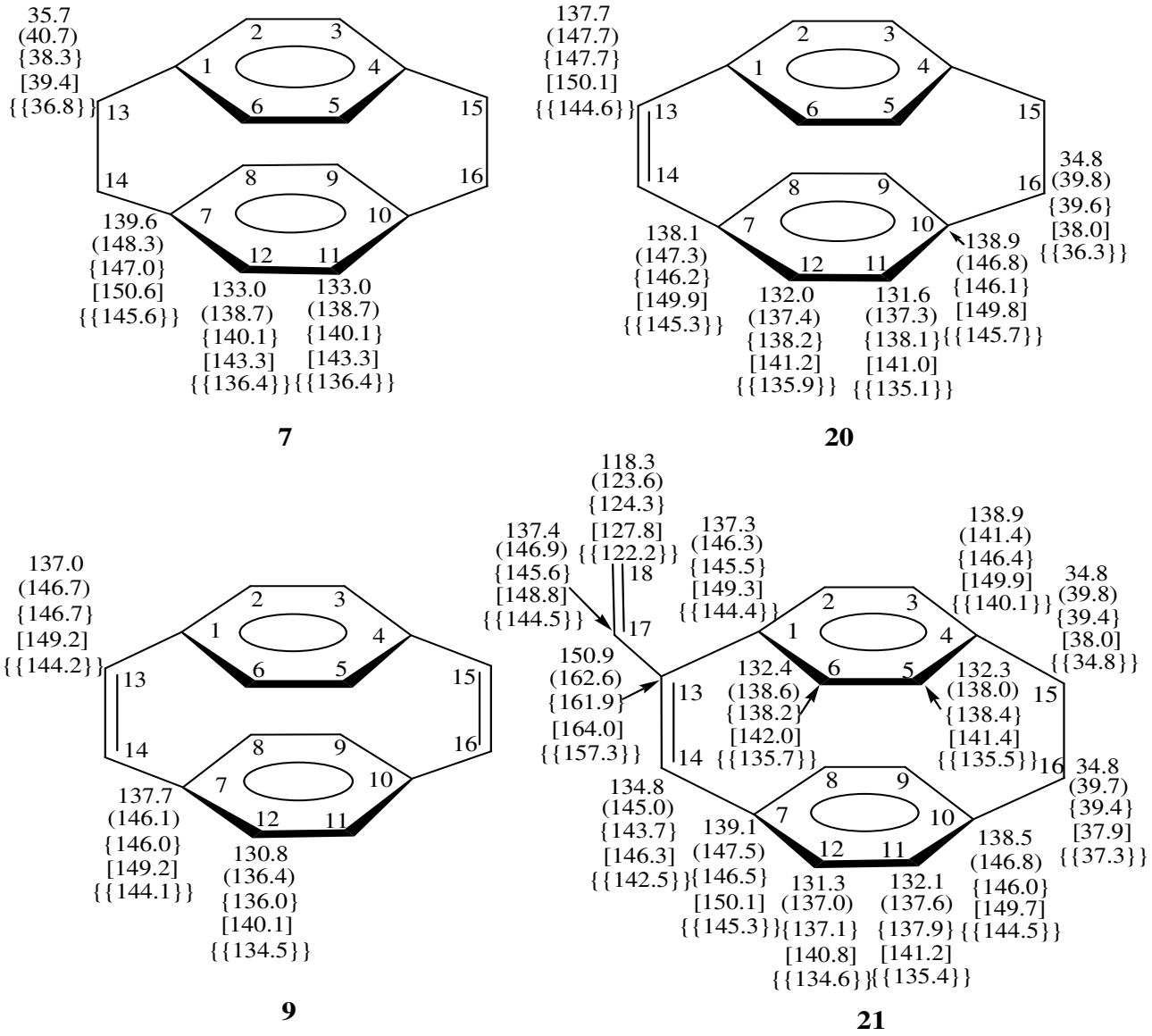

Fig. 16. ^{13}C chemical shifts (in ppm) of **7**, **20** and **21**: experimental values (this work), no brackets; and calculated values using B3LYP/6-311++G(2d,2p), in parenthesis; ωB97X-D/6-311++G(2d,2p), in curly brackets; and ωB97X-D/cc-pVQZ, in square brackets; and B3LYP/6-311G(d,p) on the structure optimized at ωB97X-D/cc-pVQZ, in double curly brackets. (Exp. for **7**, **20**, **21** - this work, for **9** "a" - this work, "b" – Ref[150]).

With the exception of a few very close values for $^{3}J_{H5H6}$ and $^{3}J_{H11H12}$ for **21**, the calculated $^{n}J_{HH}$ coupling constants listed in Annex 4 reproduce the experimentally observed trends. The $^{n}J_{HH}$ values greater than 5 Hz calculated using B3LYP/6-311++G(2d,2p) level gave the largest values, while those obtained using ωB97X-D/cc-pVQZ produced the smallest values, with the B3LYP/6-311G(d,p) NMR calculations on the structure optimized at the ωB97X-D/cc-pVQZ level giving intermediate results between the former two. The ωB97X-D/cc-pVQZ poorly reproduced the experimental $^{n}J_{HH}$ coupling constants compared to ωB97X-D/6-311++G(2d,2p).

$^{1}J_{CH}$ coupling constants of **7**, **9**, **20** and **21** are presented in Fig. 17. All the calculated results for the $^{1}J_{CH}$ coupling constants are lower than the corresponding experimental results. With the exception of the values for $^{1}J_{C13H13}$ and $^{1}J_{C2H2}$ in **7**, the B3LYP/6-311G(d,p) NMR parameter calculations performed on the structure optimized using the ωB97X-D/cc-pVQZ method yielded results that are in best agreement with the experimental ones. Except for the aromatic protons in **21**, all calculated ^{1}J values are smaller than the experimental ones with the ωB97X-D/cc-pVQZ method yielding the most accurate reproduction of the experimental data. Except for the values involving protons connected to C17 and C18 in **21**, all calculated values reproduce the experimental trends. Based on these observations, the few missing experimental values are expected to obey the trends observed in the calculations.

The available experimental and calculated values for $^{1}J_{CC}$ coupling constants are presented in Fig. 18. As mentioned in Chapter 5, only two $^{1}J_{CC}$ coupling constants of **7** have been measured. The results calculated at the different computational levels exhibit considerable differences, even though they reproduce the few available experimental trends. With few exceptions, mainly referring to close values, the results calculated using different functional/basis sets exhibit the same trends. From the calculated results, those obtained at the ωB97X-D/cc-pVQZ level on the geometry optimized at the same level are overall the smallest, while those calculated at the B3LYP/6-311G(d,p) on the structure optimized at the ωB97X-D/cc-pVQZ level are the largest. The $^{1}J_{C1C13}$ coupling constant of **7** calculated using B3LYP/6-311G(d,p) on the geometry optimized at the ωB97X-D/cc-pVQZ level are very close to the experimental result (with less than 1 Hz difference), while the corresponding value for $^{1}J_{C1C2}$ exhibits a significant difference of *ca*. 7 Hz which could be due to vibrational effects.

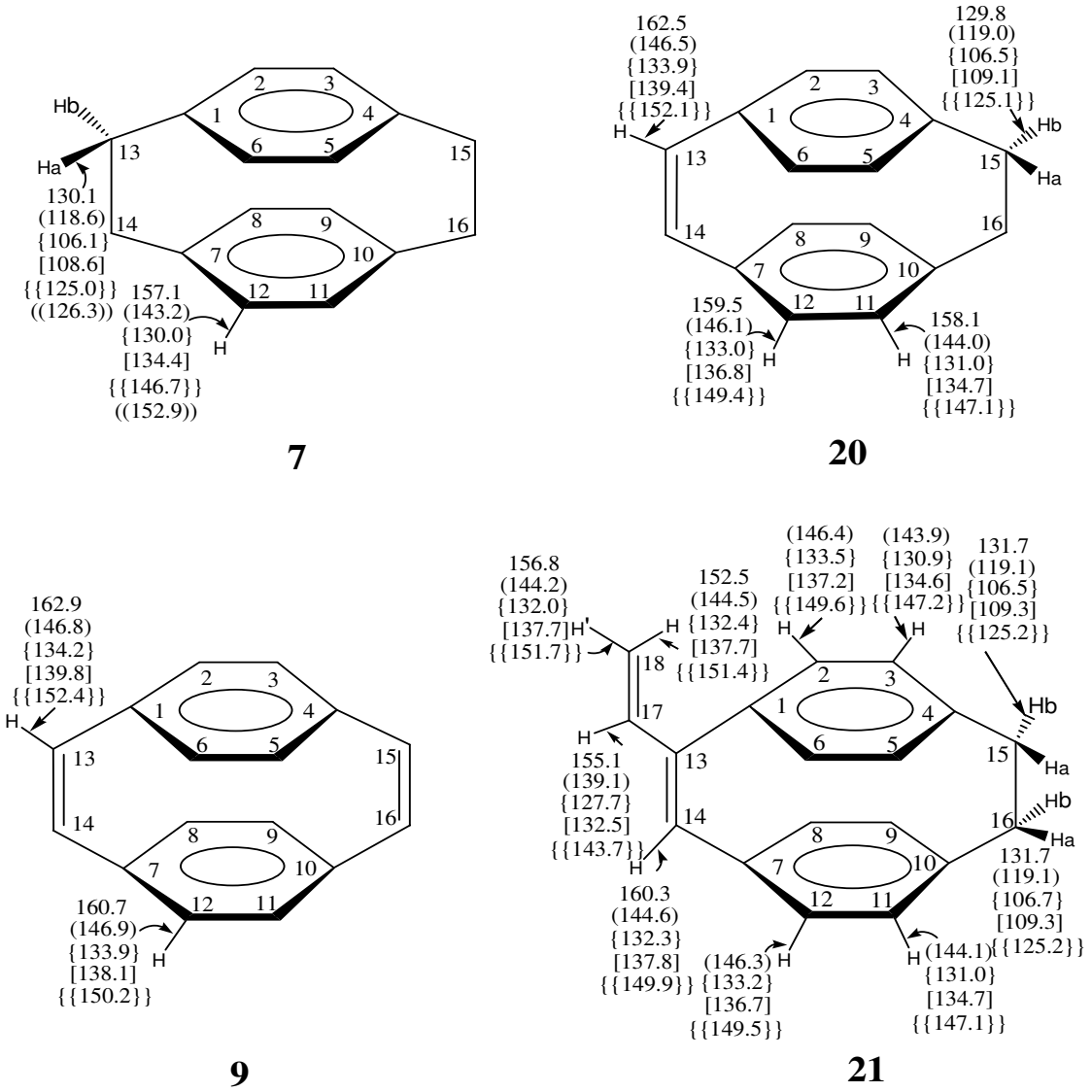

Fig. 17. $^{1}J_{CH}$ coupling constants (in Hz) for **7**, **9**, **20** and **21**: experimental values (this work), no brackets; calculated using B3LYP/6-311++G(2d,2p), in parenthesis; ωB97X-D/6-311++G(2d,2p), in curly brackets; ωB97X-D/cc-pVQZ, in square brackets; B3LYP/6-311G(d,p) on the structure optimized at ωB97X-D/cc-pVQZ, in double curly brackets; and B3LYP/Huz-IV, in double parenthesis (from Chapter 5). The "a' and "b" subscripts refer to protons pointing out of the plane and inside the plane, respectively.

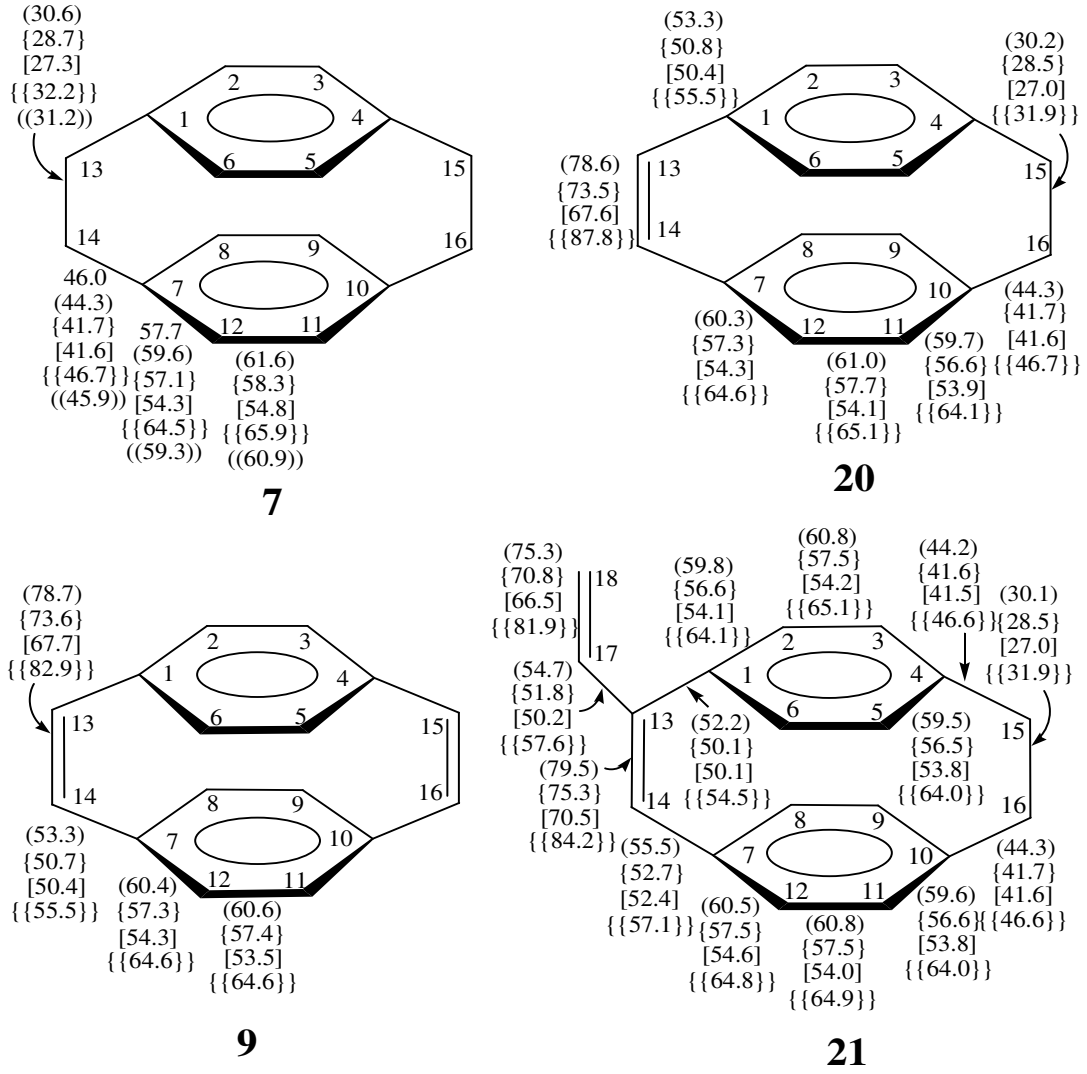

Fig. 18. $^{1}J_{CC}$ coupling constants (in Hz) for **7**, **9**, **20** and **21**: experimental values (this work), no brackets; calculated using B3LYP/6-311++G(2d,2p), in parenthesis; ωB97X-D/6-311++G(2d,2p), in curly brackets; ωB97X-D/cc-pVQZ, in square brackets; B3LYP/6-311G(d,p) on the structure optimized at ωB97X-D/cc-pVQZ, in double curly brackets; and B3LYP/Huz-IV, in double parenthesis (from Chapter 5).

6.6. NMR Parameters of Molecules 22 – 24 and 29

The experimental and calculated results for the proton chemical shifts are collected in Fig. 19. NMR parameters have been measured only for **22**,[151] **23**,[93] and **29**.[33] Except for a few very close values, the experimental and calculated values exhibit the same trends. Therefore, the missing experimental data are assumed to follow the same trend, except for the close-lying values. The majority of the chemical shifts of the aliphatic protons are reproduced much better by the calculations than those of the olefin protons. The chemical shift values for some of the aromatic protons (such as the chemical shifts for H3 and H12 in **22**) have errors exceeding 0.5 ppm. Similar to the molecules discussed in section 6.5, most chemical shifts calculated using B3LYP/6-311G(d,p) on the structure optimized at the ωB97X-D/cc-pVQZ level yield the most accurate values of the proton chemical shifts. For obvious reasons, for the aliphatic protons of the C13C14 and C17C18 bridges in **22** and **29**, the ^{1}H chemical shifts of the neighboring nuclei (H13b, H17a) are considerably larger than the values for H13a and H17b pointing in different directions. Interestingly, the chemical shift for H3 of **23** is 6.23 ppm, which is deshielded compared to **29**, whereas that for **22** is slightly shifted in the opposite direction.

The experimental and calculated results of the carbon chemical shifts are collected in Fig. 20. The results exhibit the same trends with two remarkable exceptions (a) the calculated values for C15 in **29** and (b) the experimental value of 127.6 ppm for C15 in **22** which was reported many years ago. The latter result probably calls for an experimental reinvestigation. Taking into account the above remarks and excluding very close values, the unknown experimental carbon chemical shifts for **24** are assumed to be close to the calculated values. The results for B3LYP/6-311G(d,p) on the structure optimized at ωB97X-D/cc-pVQZ are the best for almost all aromatic protons.

The calculated values for the geminal $^{2}J_{HH}$ coupling constants, listed in Annex 5, are close to the available experimental results, although they are not able to reproduce the experimental trends for $^{2}J_{H15aH15b}$ and $^{2}J_{H18aH18b}$ of **29**. Likewise, the calculated $^{3}J_{HH}$ values do not reproduce the experimental trends for the close-lying values, *e. g.* $^{3}J_{H15aH16a}$ and $^{3}J_{H17aH18b}$ of **29**.

The calculated $^{1}J_{CH}$ coupling constants and the available experimental results for **29** are listed in Fig. 21. The results show that all calculated values for the $^{1}J_{CH}$ coupling constants of **29** are lower than the corresponding experimental values. The best agreement between the values is obtained for the B3LYP/6-311G(d,p) calculations on the structure optimized at the ωB97X-D/cc-

pVQZ. On the other hand, the ωB97X-D/6-311++G(2d,2p) calculations for the structure optimized at the same level gave the poorest agreement with the available experimental results. In most cases, the largest calculated values were obtained using the B3LYP/6-311G(d,p) calculations on the structure optimized at the ωB97X-D/cc-pVQZ level, while the lowest values were obtained using the ωB97X-D/cc-pVQZ calculations for the structure optimized at the same level of calculation. In agreement with expectations, both the available experimental and calculated values for $^{1}J_{Csp3H}$ are the smallest, while those referring to the ethylenic bonds are the largest.

There are no measured $^{1}J_{CC}$ coupling constants for **22** – **24** and **29**. Except for very close values, the calculated values of $^{1}J_{CC}$ presented in Fig. 22 exhibit the same trends as the $^{1}J_{CH}$, *i.e*. the values involving C_{sp2} bridge atoms are the largest whereas those involving saturated carbon atoms are the smallest.

.

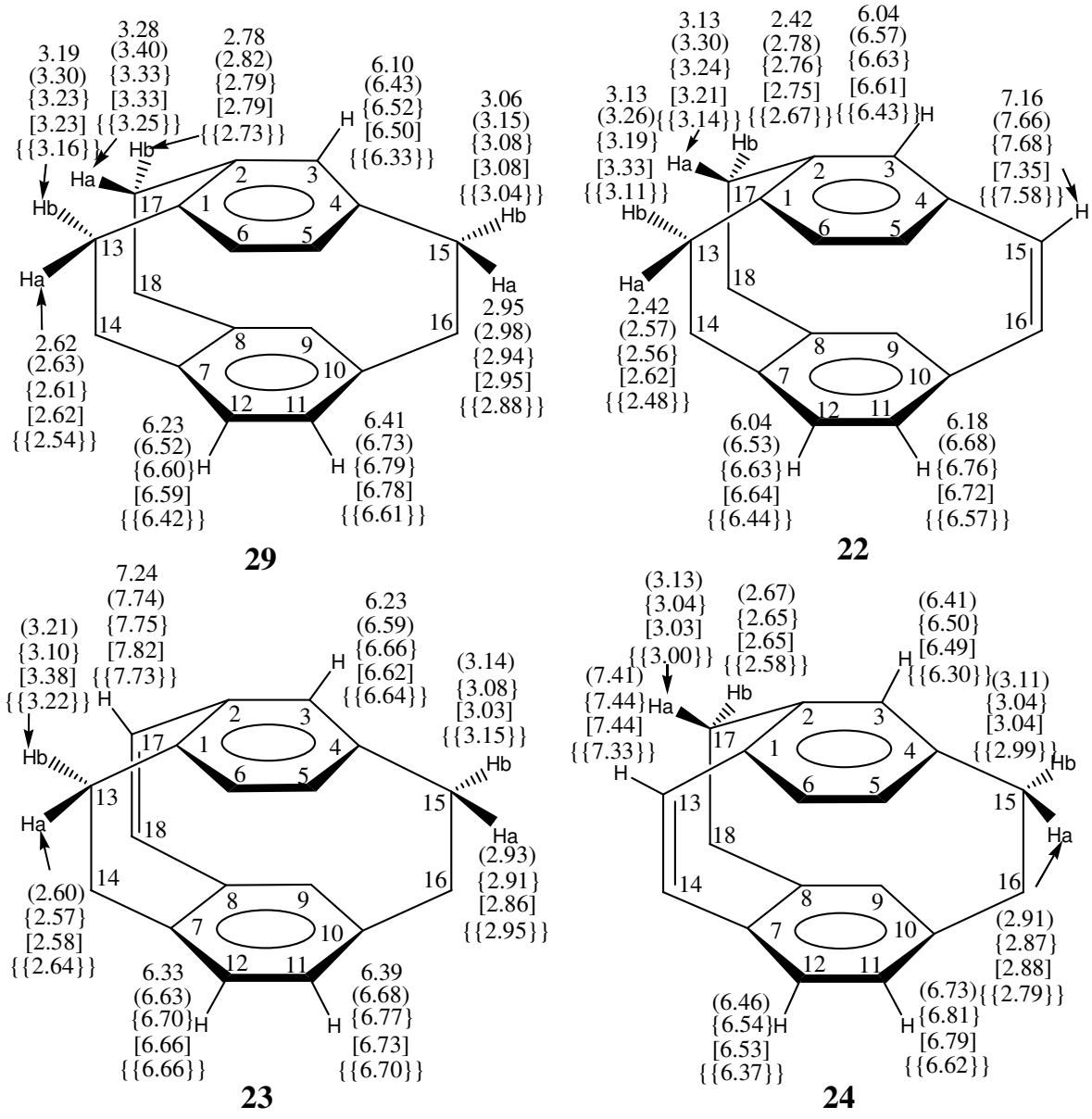

Fig. 19. ^{1}H chemical shifts (in ppm) for **22** – **24** and **29**: experimental values (this work), no brackets; calculated using B3LYP/6-311++G(2d,2p), in parenthesis; ωB97X-D/6-311++G(2d,2p), in curly brackets; ωB97X-D/cc-pVQZ, in square brackets; and B3LYP/6-311G(d,p) on the structure optimized at ωB97X-D/cc-pVQZ, in double curly brackets (Exp. **22**,[151] **23**,[93] **29**[33]). The "a' and "b" subscripts refer to protons pointing out of the plane and inside the plane, respectively.

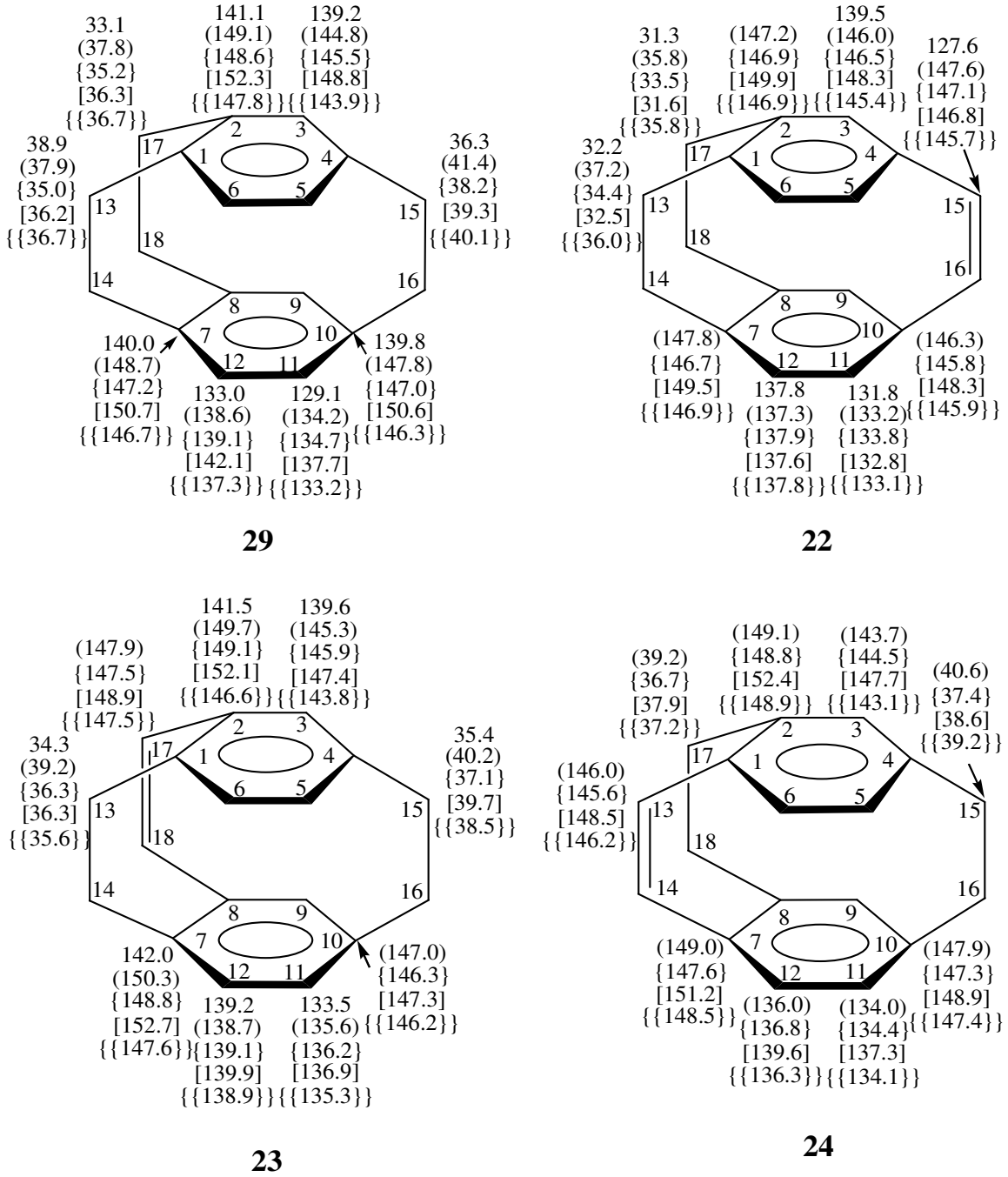

Fig. 20. ^{13}C chemical shifts (in ppm) for **22** – **24** and **29**: experimental values, no brackets; calculated using B3LYP/6-311++G(2d,2p), in parenthesis; ωB97X-D/6-311++G(2d,2p), in curly brackets; ωB97X-D/cc-pVQZ, in square brackets; and B3LYP/6-311G(d,p) on the structure optimized at ωB97X-D/cc-pVQZ, in double curly brackets (Exp. **22**,[151] **23**,[93] **29**[33]).

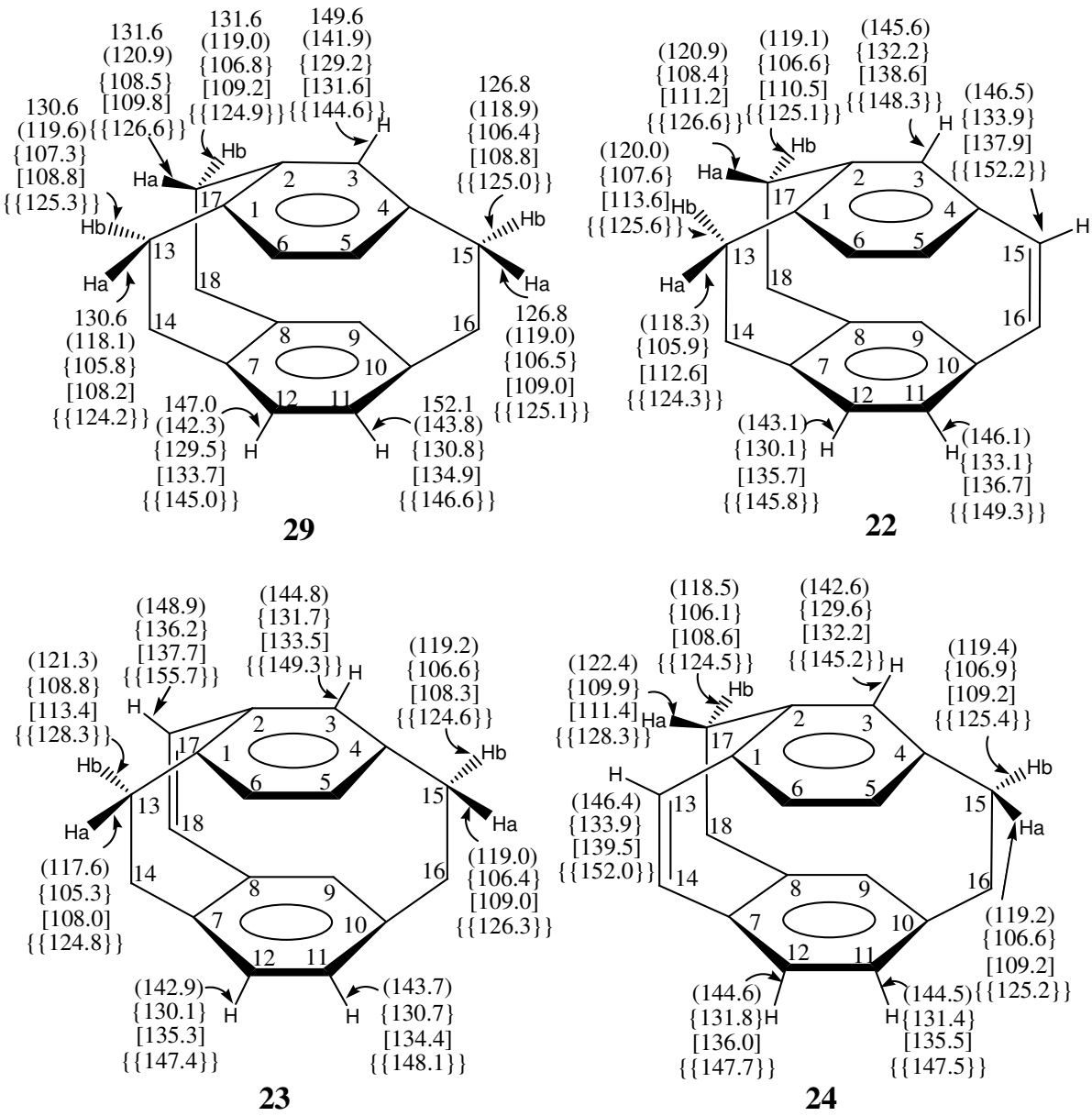

Fig. 21. $^{1}J_{CH}$ coupling constants (in Hz) for **22** – **24** and **29**: experimental values, no brackets; calculated using B3LYP/6-311++G(2d,2p), in parenthesis; ωB97X-D/6-311++G(2d,2p), in curly brackets; ωB97X-D/cc-pVQZ, in square brackets; and B3LYP/6-311G(d,p) on the structure optimized at ωB97X-D/cc-pVQZ, in double curly brackets (Exp. **29**[33]). The "a' and "b" subscripts refer to protons pointing out of the plane and inside the plane, respectively.

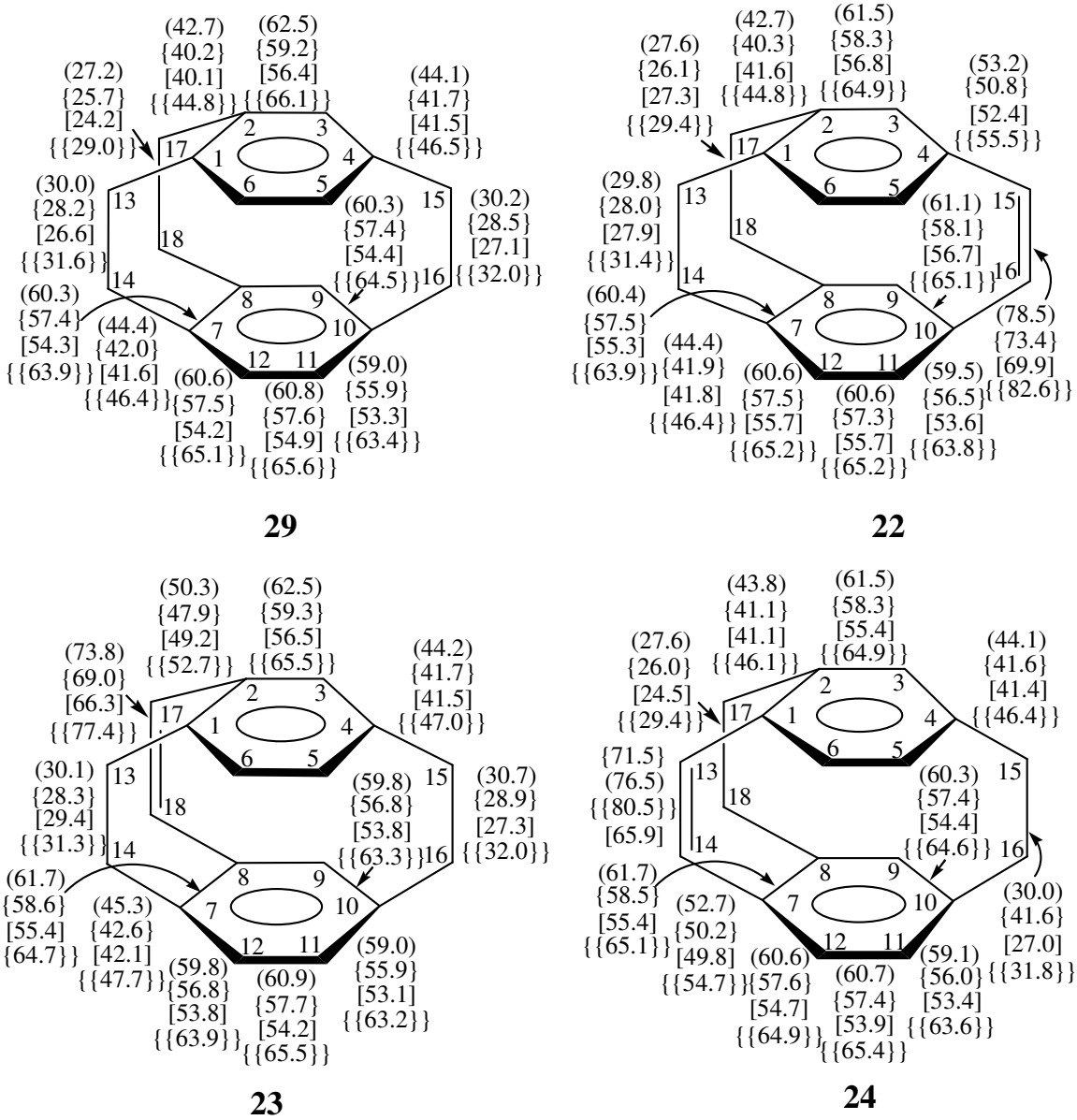

Fig. 22. $^{1}J_{CC}$ (in Hz) for **22** – **24** and **29**: calculated using B3LYP/6-311++G(2d,2p), in parenthesis; ωB97X-D/6-311++G(2d,2p), in curly brackets; ωB97X-D/cc-pVQZ, in square brackets; and B3LYP/6-311G(d,p) on the structure optimized at ωB97X-D/cc-pVQZ, in double curly brackets.

6.7. NMR Parameters of Molecules 25 – 28

Since there are no experimental NMR parameters known for these molecules, only the calculated proton chemical shift values are presented in Fig. 23, while the corresponding values for ^{13}C are presented in Fig. 24. The calculated values of the ^{1}H chemical shifts do not differ considerably among the different computational methods employed. The proton chemical shifts obtained using B3LYP/6-311G(d,p) level on the structures optimized at the ωB97X-D/cc-pVQZ level are the smallest for the whole series. Except for the H17 chemical shift of **27**, the chemical shifts of the aliphatic protons calculated using B3LYP/6-311++G(2d,2p) are the largest, whereas those obtained using ωB97X-D/cc-pVQZ are the largest for the protons bonded to the sp^2 hybridized carbon atoms, with the exception of H15 in **27** and H17 in **28**. The calculated chemical shift values of the aliphatic protons using B3LYP/6-311++G(2d,2p) are the lowest whereas the results obtained using the ωB97X-D functional for two different geometries are very close, except for H17 of **27**. The trends exhibited by the calculated proton chemical shifts are the same as the molecules discussed in section 6.6. With regard to the carbon chemical shifts, the chemical shifts of the sp^2 carbon atoms for the whole series are the smallest for C11 and C12 which could be due to the longer separation distance between these carbon atoms and the corresponding atoms of the second ring.

No experimental results are known for the J_{HH} coupling constants for **25** - **28**. The $^{2}J_{HH}$ coupling constants (Annex 6) obtained at different levels of calculation exhibit the same trends. Hence, the missing experimental results are expected to follow the same trends. The same is not true for the close-lying values of the $^{3}J_{HH}$ coupling constants (Annex 6). The calculated values of $^{1}J_{CH}$ and $^{1}J_{CC}$ are presented in Fig. 25 and Fig. 26, respectively. The $^{1}J_{Csp^3H}$ coupling constants are smaller than the $^{1}J_{Csp^2H}$ coupling constants. On the other hand, in most cases the $^{1}J_{Csp^2H}$ coupling constants of the unsaturated bridges are greater than those of the aromatic $^{1}J_{CH}$ coupling constants for all the molecules. The same is also true for $^{1}J_{CC}$ values. For instance, $^{1}J_{C13C14}$ of **25** calculated using B3LYP/6-311++G(d,p) is 76.8 Hz, whereas that of the aromatic $^{1}J_{C2C3}$ is 60.6 Hz.

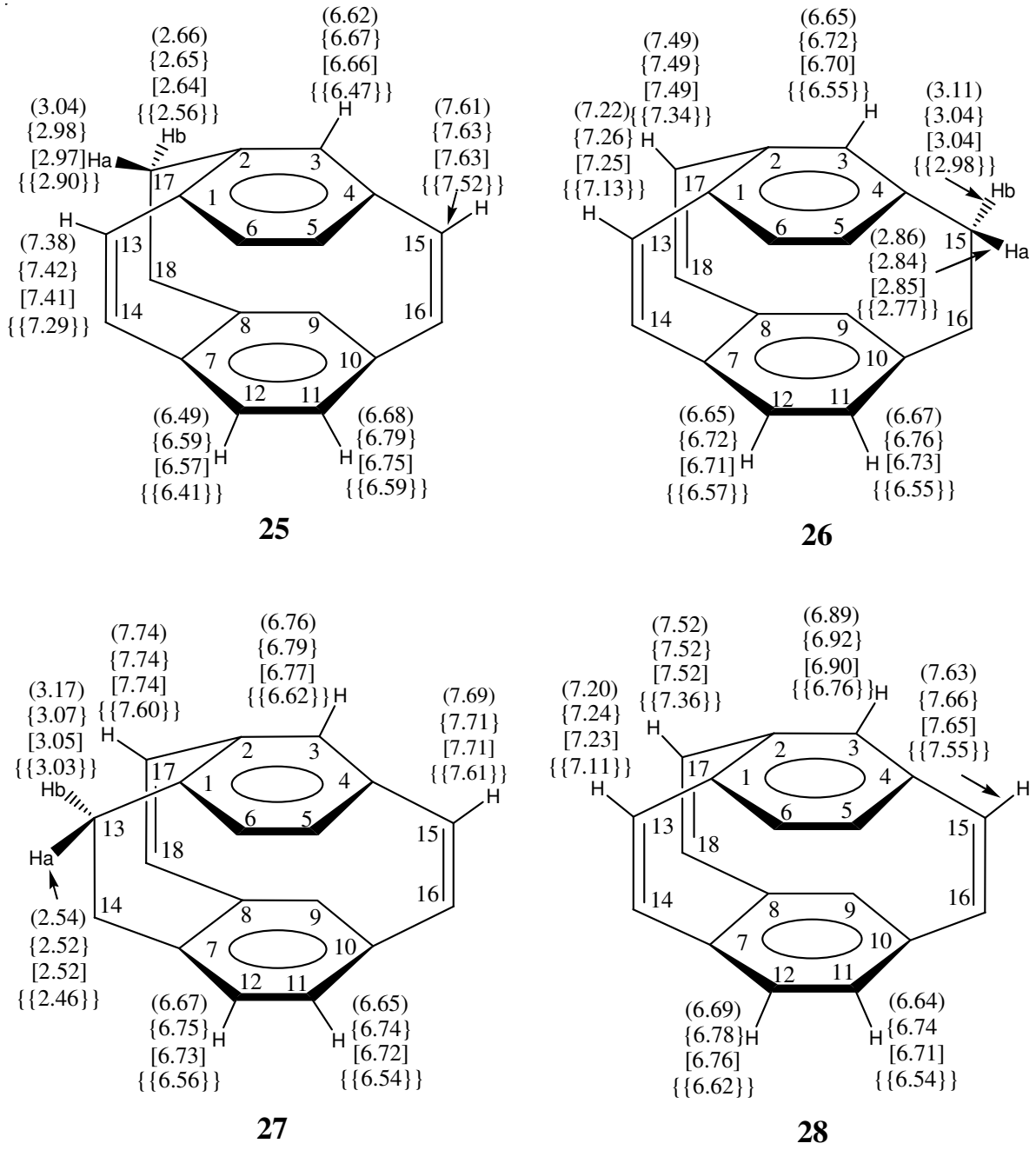

Fig. 23. ^{1}H chemical shifts (in ppm) for **25** - **28**: calculated using B3LYP/6-311++G(2d,2p), in parenthesis; ωB97X-D/6-311++G(2d,2p), in curly brackets; ωB97X-D/cc-pVQZ, in square brackets; and B3LYP/6-311G(d,p) on the structure optimized at ωB97X-D/cc-pVQZ, in double curly brackets. The "a' and "b" subscripts refer to protons pointing out of the plane and inside the plane, respectively.

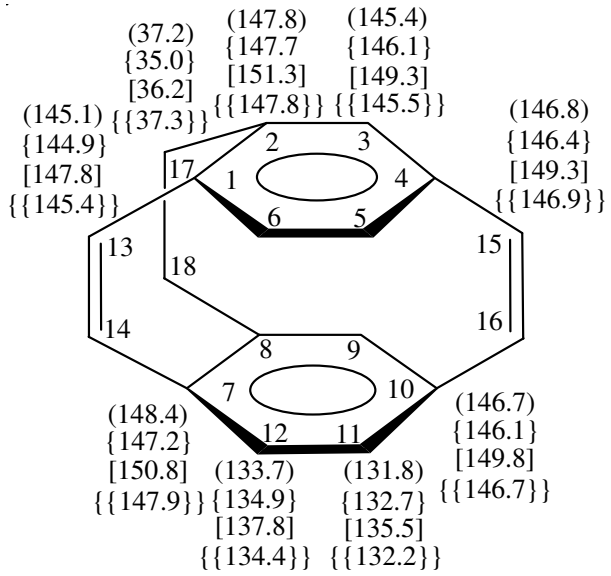

25

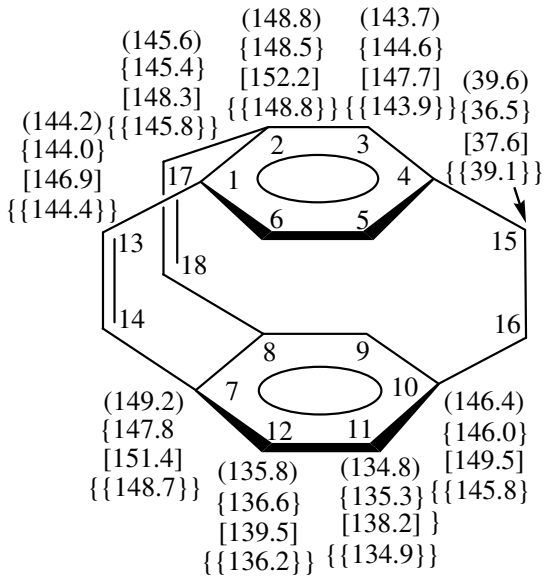

26

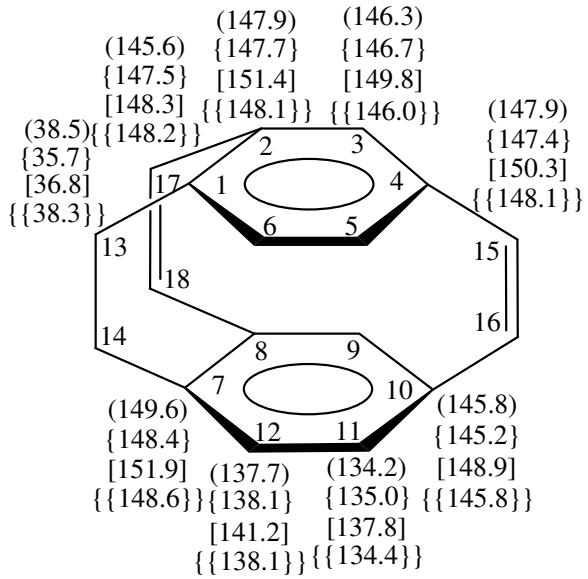

27

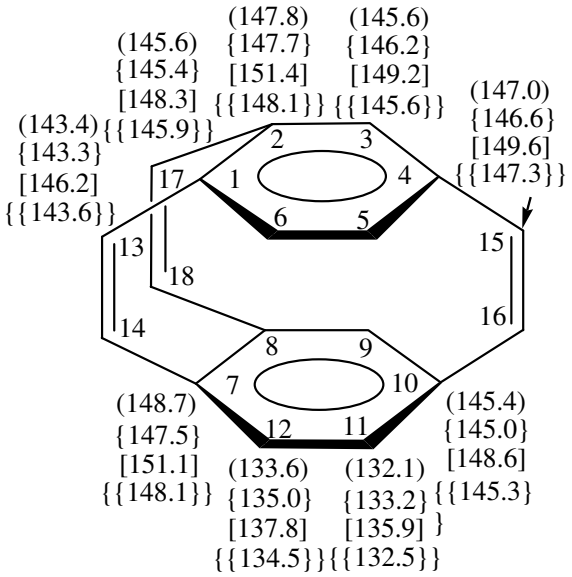

28

Fig. 24. ^{13}C chemical shifts (in ppm) for **25** - **28**: calculated using B3LYP/6-311++G(2d,2p), in parenthesis; ωB97X-D/6-311++G(2d,2p), in curly brackets; ωB97X-D/cc-pVQZ, in square brackets; and B3LYP/6-311G(d,p) on the structure optimized at ωB97X-D/cc-pVQZ, in double curly brackets.

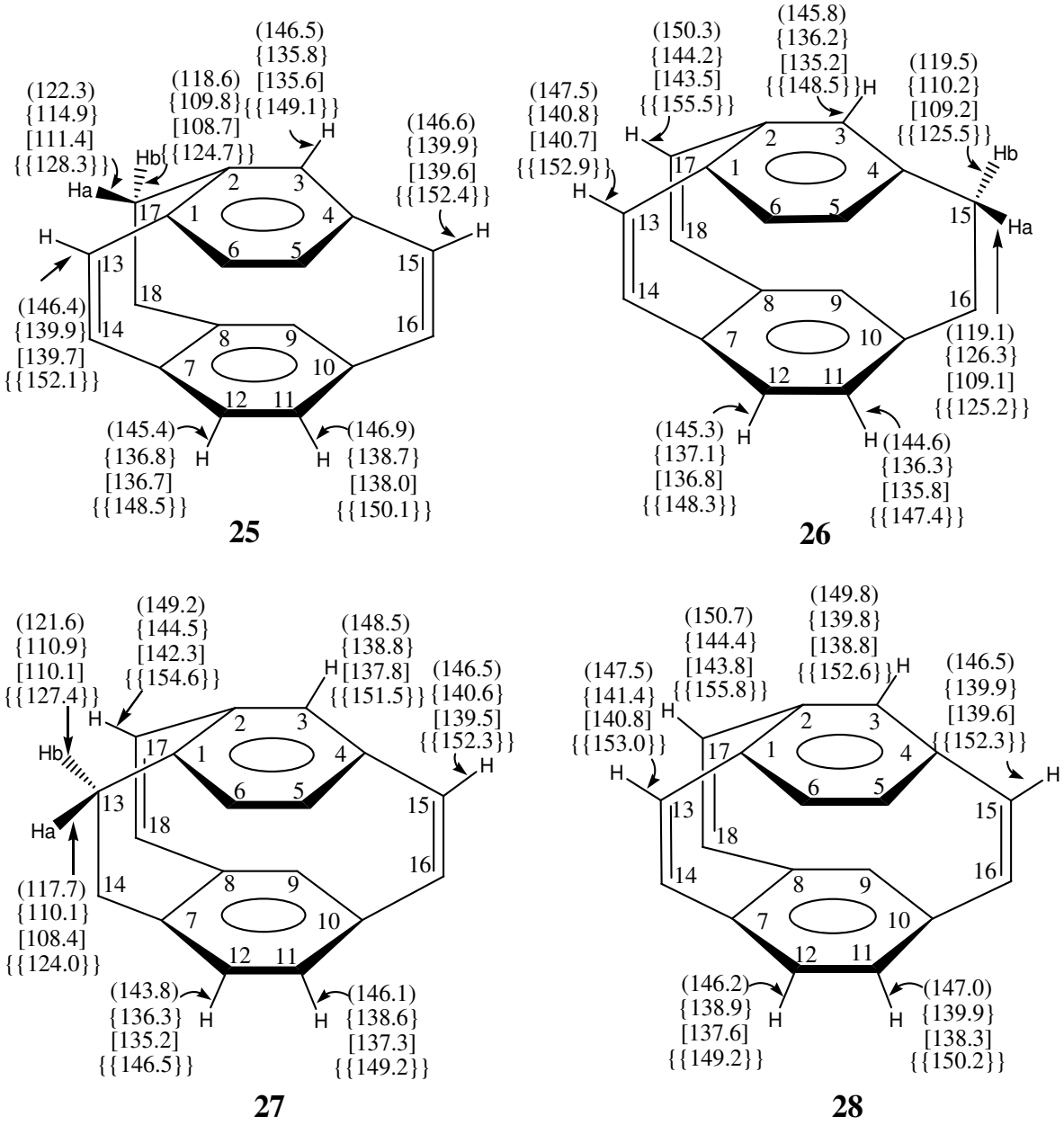

Fig. 25. $^{1}J_{CH}$ coupling constants (in Hz) for **25** - **28**: calculated using B3LYP/6-311++G(2d,2p), in parenthesis; ωB97X-D/6-311++G(2d,2p), in curly brackets; ωB97X-D/cc-pVQZ, in square brackets; and B3LYP/6-311G(d,p) on the structure optimized at ωB97X-D/cc-pVQZ, in double curly brackets. The "a' and "b" subscripts refer to protons pointing out of the plane and inside the plane, respectively.

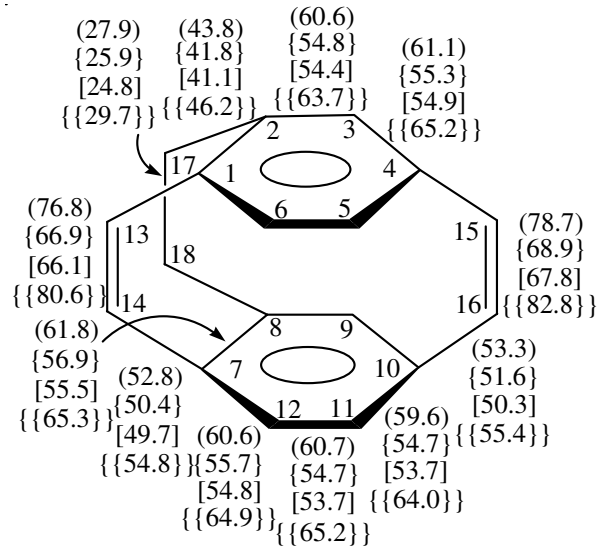

25

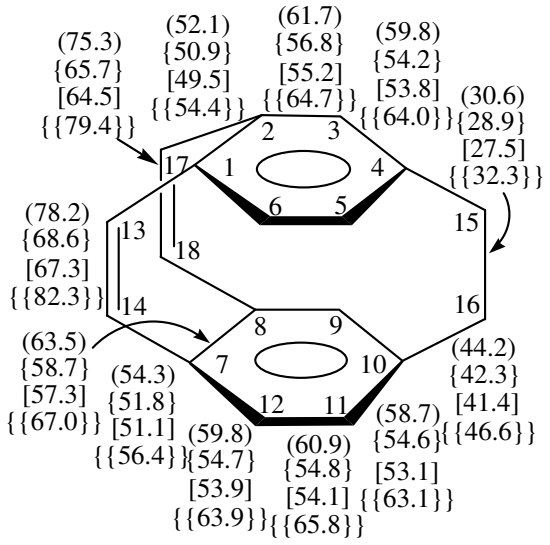

26

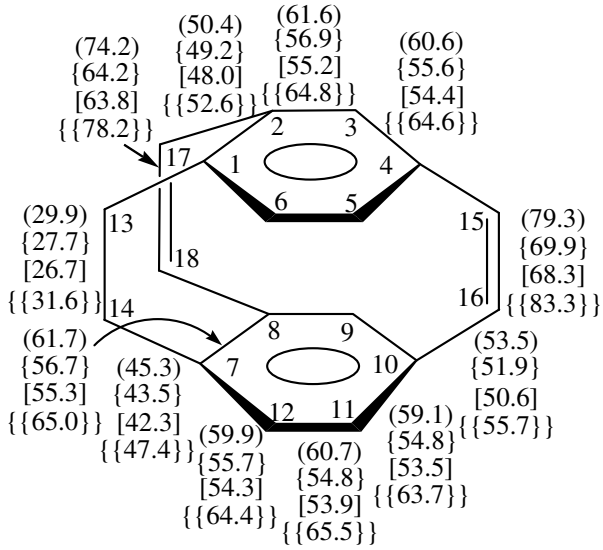

27

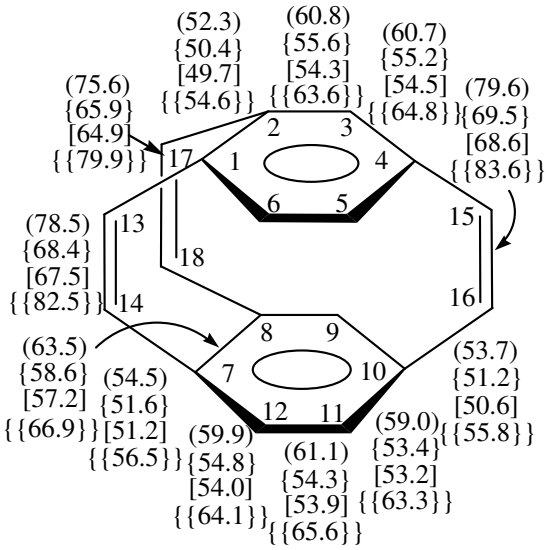

28

Fig. 26. $^{1}J_{CC}$ coupling constants (in Hz) for **25** - **28**: calculated using B3LYP/6-311++G(2d,2p), in parenthesis; ωB97X-D/6-311++G(2d,2p), in curly brackets; ωB97X-D/cc-pVQZ, in square brackets; and B3LYP/6-311G(d,p) on the structure optimized at ωB97X-D/cc-pVQZ, in double curly brackets.

6.8. Conclusion

In this chapter, the molecular geometries of **7**, **9** and **20** - **29** have been optimized using B3LYP/6-311++G(2d,2p), ωB97X-D/6-311++G(2d,2p) and ωB97X-D/cc-pVQZ. The optimized structural parameters are compared with the available experimental data. The most important parameters are the lengths of the central bridge bonds that are sensitive to the computational method applied. The comparison of the results indicated that the ωB97X-D functional provided better estimates for the bonds than the B3LYP functional. The distances between the corresponding atoms of the two aromatic rings are usually considerably larger than the corresponding available experimental data. The comparison of the calculated and experimental results of **29** is blurred by the existence of two molecules in the unit cell. However, the distances are much better reproduced using the ωB97X-D/6-311++G(2d,2p) and ωB97X-D/cc-pVQZ levels of theory than other computational protocols. Moreover, the accuracy of the calculated bond and torsional angles is usually satisfactory.

With the exception of the close-lying signals, the NMR parameters calculated using ωB97X-D/cc-pVQZ, in most cases, reproduce the experimental trends. The results of the chemical shifts from different computational levels usually show the same trends. Hence, the calculated values are assumed to correctly describe the experimental chemical shifts and coupling constants that could not be measured for the known and the hypothetical molecules. Usually, the NMR parameters obtained from B3LYP/6-311G(d,p) calculations on the structure optimized using ωB97X-D/cc-pVQZ are the best. However, in contrast to the geometry optimizations, the agreement between the values of the NMR parameters obtained from the ωB97X-D/cc-pVQZ calculations and the corresponding experimental ones are usually the poorest compared to those obtained from the ωB97X-D/6-311++G(2d,2p) NMR parameter calculations. Of the two functionals used, B3LYP performed poorly compared to ωB97X-D functional for the geometry optimizations, which could be due to the over-repulsive nature of the former functional in the van der Waals region, whereas it gives better NMR parameters at the geometry optimized using the ωB97X-D functional.

Chapter 7

[*m.n*]Paracyclophanes (*m*, *n* = 2 – 4) with Varying Lengths of the Bridges

7.1. Introduction

As discussed in Chapter 1, benzene and its aromatic derivatives are among the most important compounds in organic chemistry. Among these, cyclophanes with short bridges hold a prominent place. For instance, they are important test-beds for the understanding of steric repulsions and π-π electronic interactions.[1-3] Cyclophanes also have interesting conformational properties.[2,15,16,33,136] When the bridge(s) connecting the aromatic ring(s) is/are short, the aromatic rings are fixed in a very close distance relative to each other. This close distance between the rings leads to strain in the aromatic ring moieties which further causes deformation of the rings, potentially breaking their inherent planarity.[2,3,14-20] In addition, there are also considerable electronic interactions between the aromatic rings when they are close to each other. These electronic interactions lead to additional influences on the geometry and electronic structure of the cyclophanes that can be based on their unusual spectroscopic responses.[18]

As discussed in the previous chapters, the experimental data for [2.2]paracyclophane **7** give contradictory results. The X-ray structure obtained at 100 K by Lyssenko *et al*. in 2003[20] yielded an eclipsed D_{2h} symmetry, whereas the earlier measurements by Hope *et al*. in 1970[23] at room temperature showed the D_2 symmetry. The value of the $C_{sp2}C_{sp3}C_{sp3}C_{sp2}$ twist dihedral angle for the latter geometry has also been the subject of controversy in both experimental,[20,23] and theoretical studies.[14,22,26,30] As already pointed out in Chapters 5 and 6, despite the many theoretical studies advocating a large value of the twist angle[14,22,26,28] we believe that the zero value of the aromatic ring twist angle determined by the Lyssenko group[20] or the small values (less than 6^o) are the most reliable. This view is supported from careful analysis of the data stored in the Cambridge Data Base also indicating that the $C_{sp2}C_{sp3}C_{sp3}C_{sp2}$ torsional angles of cyclophanes with multiple ethylene bridges and their derivatives are not larger than 3^o.

The spectroscopic parameters of the molecules are affected due to the proximity of the rings and the structural abnormalities. Among these spectroscopic parameters, NMR chemical shifts and spin-spin coupling constants, as well as UV/Vis spectral parameters are known to be very sensitive to the molecular structure. The bridge length variation and deformation of the aromatic rings alter not only the chemical shifts and coupling constants but also the excitation and emission spectra of the [*m.n*]paracyclophanes.

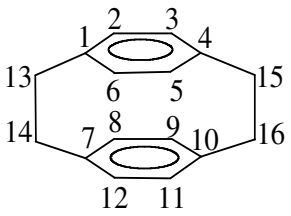

7

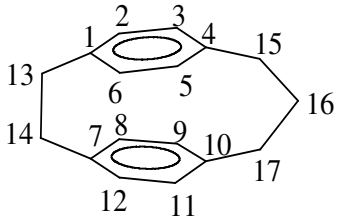

16

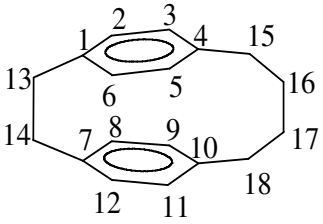

30

The synthesis[88] and a few static NMR[53,54,88,133] spectra for the [*m.n*]paracyclophanes (*m*, *n* = 2 – 4) have been reported. However, no detailed structural and spectroscopic studies have been reported for these molecules. Moreover, there are no reported theoretical studies of the geometry and NMR parameters for **16**, **30**, and **31**. Bachrach[14] reported a computational stability analysis of **7**, **15** and **32** focusing on conformational analysis and strain energies. He also obtained a twist angle of 10^{o} – 18^{o} for **7** using different functionals.[14] The results reported by Grimme[22] also showed that the calculated twist angle of **7** is dependent on the type of functional used, where only the B3LYP functional results of the C1C13C14C7 twist angle for the D_{2h} structure agree with the latest experimental result reported by Lyssenko *et al.*[20] Dodziuk *et al.*[15] studied the structure and dynamics of **15** and showed that in solution it exists as a mixture of *cis*- and *trans*-isomers,[15,152] with the *trans* prevailing, whereas in the solid state only the *trans*-isomer exists due to favorable crystal packing forces.[17] Dodziuk *et al.*[15] also determined an interconversion barrier of 12.29 ± 0.08 kcal/mol and preexponential factor Log (*A*) = 12.99±0.07 s^{-1} between the *cis* and *trans* conformations of **15** using line-shape analysis of the NMR spectra in solution combined with B3LYP computed chemical shifts and coupling constants. Szymański *et al.*,[153] analyzed the dynamics of **16** using temperature-dependent NMR measurements which resulted in the Arrhenius activation energy E_a = 11.57±0.08

kcal/mol, and preexponential factor Log (A) = 12.92±0.07 s^{-1} for the propano-bridge inversion of **16**. On the other hand, two separate sets of Arrhenius activation energies, E_a = 11.2±0.5 kcal/mol and Log (A) = 13.6±0.5 s^{-1} for the propano-bridge inversion, and E_a = 9.7±0.4 kcal/mol and Log (A) = 13.2±0.4 s^{-1} for the butano-bridge inversion were determined for **31** by Szymański *et al.*[153]

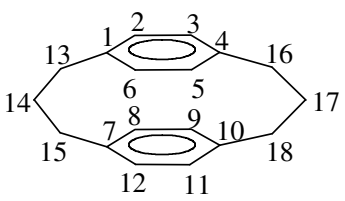

15

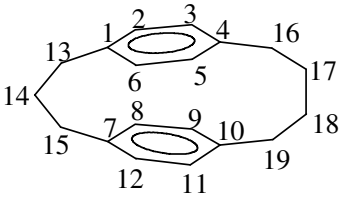

31

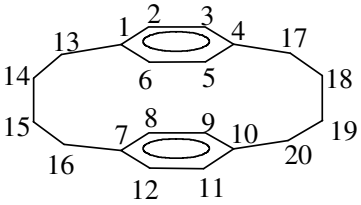

32

The absorption and emission spectroscopic studies of **7** and **15** have been reported.[36,37,118,119,121,122,154] Among these, Shen *et al.*[36] reported the absorption spectrum for the first excited state transition of **7** in the region between 307 and 326 nm. On the other hand, Melzer *et al.*[119] found the maximum emission wavelength for **7** and **15** to lie between 475 and 485 nm. Fuke *et al.*[31] has also reported the two-photon absorption spectrum of crystalline **7** and assigned the two absorption bands in the region between 288.2 and 273.97 nm to the two even-parity allowed $^1B_{1g} \leftarrow {}^1A_{1g}$ and $^1B_{2g} \leftarrow {}^1A_{1g}$ transitions. Recently Shirai *et al.*[28] reported an *ab initio* molecular orbital study on the excited states of **7** and **15**. According to their study, the first excited state equilibrium distances between the benzene rings are shorter than those in the corresponding ground state.

A detailed structural and spectroscopic analysis of the [*m.n*]paracyclophanes (*m*, *n* = 2 – 4) is of value, since they have interesting properties and promising prospective applications as discussed in Chapter 1. Therefore, in this chapter, a study of the structure, NMR, absorption and emission properties of these molecules has been undertaken to explore the influence of the nonparallel arrangement of the aromatic rings and the bridge lengths on their properties. As was presented in Chapters 5 and 6, a combination of experimental and computational techniques was used for the study.

7.2. Symmetry, Torsional Angles of the Bridges and Conformations

The structural analysis of **7** has been presented in the previous two chapters. However, it is reconsidered briefly for the sake of comparison with the other molecules studied in this chapter. The X-ray structural measurement at 297 K and analysis of **7** by Hope *et al*. from 1970,[23] gave a disordered structure with D_2 symmetry. On the other hand, the recent X-ray structural study by Lyssenko *et al*.,[20] measured at 100 K, resulted in the D_{2h} structure without any disorder. As discussed in the previous chapters as well as by Grimme[22] and Bachrach,[14] the optimized geometry of **7** also strongly depends on the type of functional used in theoretical studies. The dispersion corrected ωB97X-D functional gives a structure with D_2 symmetry, whereas B3LYP gives a D_{2h} geometry. As shown in Fig. 3, the energy barrier between the two conformers obtained from the calculations using the ωB97X-D functional is only 0.2 kcal/mol. The angle that defines the twist of the aromatic rings of **7** (C1C13C14C7) calculated using the B3LYP functional is -0.5°, which is close to the D_{2h} symmetry and using the ωB97X-D functional it is 14.9° with D_2 symmetry.

It is evident that the experimental geometries are determined in the solid state, whereas those of the calculations refer to isolated molecules in the gas phase. With this in mind, the comparison of experimental and computed geometries is often very difficult and hence, the functional that correctly reproduces the interring separations (*vide infra*) does not necessarily give reliable values of the bridge torsional angles. For example, the results discussed in Chapter 6 showed that the bond lengths and bond angles of **7** calculated using ωB97X-D are in excellent agreement with the experimental geometry obtained by Lyssenko *et al*.[20] However, the C1C13C14C7 twist angle of **7** obtained from the optimization of the same functional is 14.9° (Table 11) whereas the experimental twist angle from the study by Lyssenko *et al*. at 100 K is 0.0°,[20] and that by Hope *et al*. is 6.4° at room temperature.[23,128] In a study by Shirai *et al.*[28] and Bachrach,[14] on the basis of MP2 and ωB97X-D calculations, unreliably high values of 21.8° and 15.4°, respectively, for the C1C13C14C7 twist angle have been reported. However, the inspection of the data collected in the Cambridge Structural Database, CSD,[155,156] for **7** and its derivatives shows that (i) at room temperature, there is considerable disorder in the observed structures and (ii) the $C_{sp2}C_{sp3}C_{sp3}C_{sp2}$ torsional angles are less than 6°. Therefore, we believe that torsional angles less than 6° are most representative for the structure of **7**. Moreover, the large differences between the torsional

angles obtained using the two functionals demonstrate the complexity of the problem of finding appropriate functionals that describe the special structure of the highly strained molecules such as **7**.

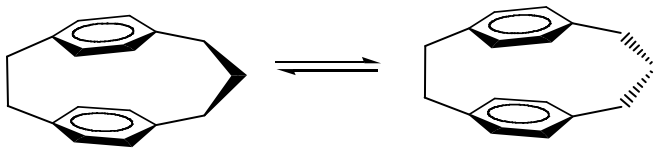

16a **16b**

The C1C13C14C7 and C4C1C7C10 twist angles of the molecules studied in this chapter are collected in Table 11. When the bridge length of the [*m.n*]paracylophanes increases, there is a possibility for the existence of conformational isomerism. **16** and **30** have two enantiomers of C_s and C_2 symmetries, respectively. The results in Table 11 show that the C1C13C14C7 twist angle obtained from the ωB97X-D optimization of **16** is 0^o, while that of **30** is 28.5^o. There are no available experimental data of this angle, and hence there are no results to which we can compare our calculations and decide on which functional performs the best. However, it is noted that the geometries optimized using the B3LYP functional show that the two aromatic rings of **7** and **16** are eclipsed, in contrast to **30**, whereas only those of **16** are eclipsed in the ωB97X-D calculations.

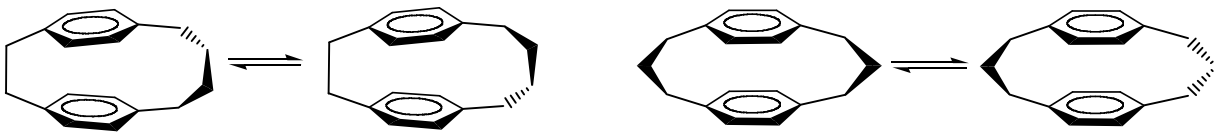

30a **30b** ***cis*-15** ***trans*-15**

15 exists as a mixture of the more stable C_{2v} (*cis*) and C_{2h} (*trans*) conformers in solution. However, in the solid state, it crystalizes in its *trans* form due to favorable crystal packing. The X-ray structure of **15** has S_2 symmetry (with a C1C13C15C7 torsional angle of 2.8^o),[17] whereas all calculations in our study lead to a structure with C_{2h} symmetry (with this angle equal to 0^o).

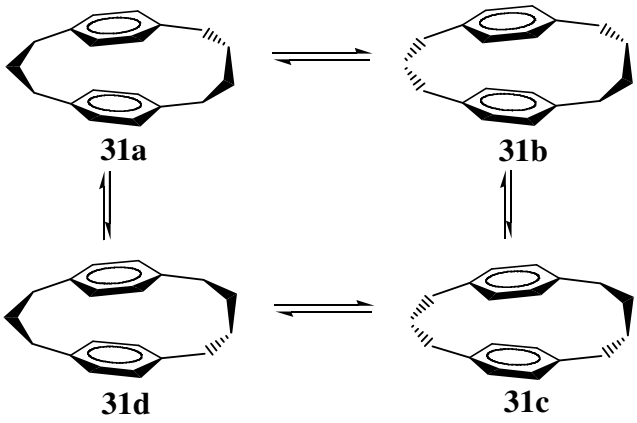

All the calculations performed for **31** resulted in a structure with C_1 symmetry. In the case of **32**, rotations of the rings, as well as conformational motion of the bridges, give four conformational isomers of which only the two lowest ones have significant population at room temperature. Rotating one of the bridges of **32** while keeping the rings parallel, gives rise to two conformers with D_2 and C_{2h} (1.61 kcal/mol higher than D_2) symmetries, with 94% population of the D_2 structure. This result is in agreement with the experimental result reported by Jones *et al.*[42]

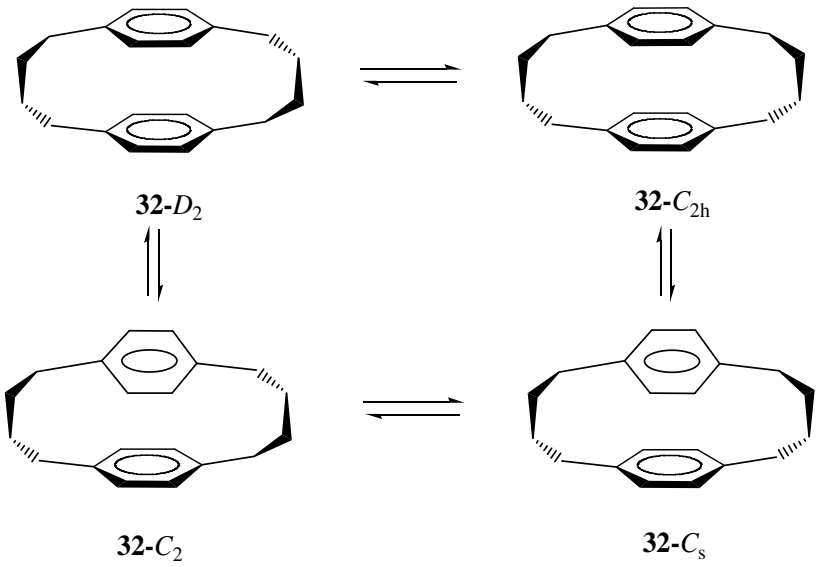

7.3. Separation Distances Between the Aromatic Rings

The available experimental and calculated non-bonding distances between the corresponding carbon atoms of the aromatic rings and ring deformation as well as twist angles are presented in Table 11. In **16**, **30** and **31**, the average planes of the rings are not parallel unlike those of **7**, **15** and **32**. Unlike that of **32**, the C1…C7 interring separation distance of **7**, **15**, **16**, **30** and **31** is shorter than the sum of the van der Waals radii between two stacked carbon atoms (*ca.* 3.4 Å). The C4…C10 distances of **30**, **31** and **32** are longer than 3.4 Å, which is not the case for those of **7**, **15** and **16**. The analysis of the distances obtained from the different functionals in this dissertation as well as from the study by Grimme *et al*.[25] shows that the dispersion-uncorrected B3LYP functional overestimates the interring separation distance, as well as the $C_{sp^3}C_{sp^3}$ bond length, which is due to the over-repulsive nature of the functional in the van der Waals region. In contrast, the dispersion-corrected functionals (*e. g.* ωB97X-D) give results considerably closer to the experimental values.[14,22,52] However, as discussed above, the twist angle determined by these dispersion-corrected functionals is significantly larger than the available experimental values.[20,23]

Table 11. Distances (in Å) between the corresponding non-bonded carbon atoms, ring deformation and twist angles (in degrees) of the two aromatic rings: experimental values, no brackets; and calculated values using B3LYP/ccJ-pVTZ, in parenthesis; and ωB97X-D/ccJ-pVTZ, in square brackets.

	7	**16**	**30**	***trans*-15**	***cis*-15**	**31**	**32**-C_{2h}	**32**-D_2
	2.786[a]	-	-	-	-	-	-	-
C1C7	2.782[b]	-	2.79	3.137	-	-	-	3.96
	(2.826)	(2.831)	(2.847)	(3.238)	(3.242)	(3.274)	(4.156)	(4.160)
	[2.797]	[2.785]	[2.798]	[3.205]	[3.209]	[3.168]	[3.891]	[4.046]
	3.099[a]	-	-	-	-	-	-	-
C2C8	3.097[b]	-	-	3.289	-	-	-	-
	(3.156)	(3.156)	(3.303)	(3.410)	(3.328)	(3.489)	(4.216)	(4.229)
	[3.112]	[3.094]	[3.223]	[3.372]	[3.294	[3.355]	[3.892]	[4.080]
	3.099[a]	-	-	-	-	-	-	-
C3C9	3.097[b]	-	-	3.310	-	-	-	-
	(3.156)	(3.357)	(3.847)	(3.427)	(3.328)	(3.817)	(4.216)	(4.229)
	[3.112]	[3.283]	[3.751]	[3.387]	[3.294]	[3.674]	[3.892]	[4.080]
	2.786[a]	-	-	-	-	-	-	-
C4C10	2.782[b]	-	3.86	3.137	-	-	-	3.99
	(2.826)	(3.256)	(3.959)	(3.238)	(3.242)	(3.936)	(4.156)	(4.160)
	[2.797]	[3.186]	[3.878]	[3.205]	[3.209]	[3.814]	[3.891]	[4.046]
	3.099[a]	-	-	-	-	-	-	-
C5C11	3.097[b]	-	-	3.289	-	-	-	-
	(2.826)	(3.444)	(3.847)	(3.409)	(3.512)	(3.921)	(4.216)	(4.229)
	[2.797]	[3.351]	[3.751]	[3.372]	[3.469]	[3.765]	[3.892]	[4.080]
	3.099[a]	-	-	-	-	-	-	-
C6C12	3.097[b]	-	-	3.310	-	-	-	-
	(3.156)	(3.222)	(3.303)	(3.426)	(3.512)	(3.606)	(4.216)	(4.229)
	[3.112]	[3.140]	[3.223]	[3.387]	[3.469]	[3.458]	[3.892]	[4.080]
	-14.4[a]	-	-	-	-	-	-	-
C2C1C6C5[f]	12.6[b]	-	-	-8.2	-	-	-	-
	(-14.9)	(-10.9)	(-7.7)	(-8.7)	(-8.2)	(-4.5)	(-2.8)	(-3.3)
	[-14.8]	[-11.7]	[-7.9]	[-8.5]	[-8.0]	[-4.9]	[-3.1]	[-3.4]
	0.0[a]	-	-					
C1C13C14C7	6.4[b]	-	-	-	-	-	-	-
	(-0.4)	(0.0)	(25.9)					
	[-14.9]	[0.0]	[28.5]					
	0.0[a]	-	-	0.0	-	-	-	-
C4C1C7C10	(-1.0)	(0.0)	(11.5)	(0.0)	(0.0)	(5.4)	(13.8)	(0.0)
	[-5.2]	[0.0]	[12.9]	[0.0]	[0.0]	[5.2]	[14.0]	[0.0]

[a]Ref.[20] [b]Ref.[23] [c]Ref.[95] [d]Ref.[17] [e]Ref.[42] [f]The difference in sign is inconsequential.

7.4. Bond Lengths and Angles

The available experimental and calculated bond lengths are collected in Annex 7 while the bond and torsional angles are listed in Annex 8. An inspection of the results shows that the calculated bond lengths reproduce the experimental trends. The calculations using ωB97X-D/Huz-IV give in most cases the best agreement with the available experimental values, although they still are not fully satisfactory. Unsurprisingly, the largest deviations from a standard geometry are those of the $C_{sp3}C_{sp3}$ bond lengths of the shorter bridge of **7**, **16** and **30**, which are longer than the usual $C_{sp3}C_{sp3}$ bond length of 1.540 Å.[157] In the other case, the $C_{sp2}C_{sp3}$ bonds of **7**, **16** and **30** along the bridges are slightly longer than the standard exocyclic bond length of 1.478 Å. However, the $C_{sp2}C_{sp2}$ bond lengths are close to that of benzene.

The bridge $C_{sp3}C_{sp3}C_{sp3}$ bond angles are larger than the regular tetrahedral bond angle of 109.5°, with a considerably larger values for **16**, close to 120°. On the other hand, the $C_{sp2}C_{sp3}C_{sp3}$ and $C_{sp2}C_{sp2}C_{sp3}$ bond angles are near to the corresponding regular bond angles of standard molecules. With the exception of those at the bridgeheads that are less than 120° due to the ring strain, the same has also been observed for the $C_{sp2}C_{sp2}C_{sp2}$ bond angles. In agreement with expectations and available experimental results, the $C_{sp2}C_{sp2}C_{sp3}$ angles that describe the deviation of the C_{sp3} atom from the approximate plane of the aromatic rings, such as C1C4C15 in **7** and the analogous ones in the other molecules, are less than 160° in **7** and increasing up to 177° for **32**-C_{2h}. The C2C1C6C5 torsional angle, that characterizes the non-planar distortions of the aromatic rings, decreases with increase in bridge length. For the paracyclophanes with non-parallel rings, **16**, **30** and **31**, this torsional angle is smaller on the side of the shorter bridge. This difference from the two bridge sides suggests that the influence of the π-π electron repulsion between the two aromatic rings is stronger than the energy gained by increasing the length of the bridges.

7.5. ^{1}H Chemical Shifts

The proton chemical shifts are presented in Figs. 27 - 32. As mentioned in Chapter 4, the experimental results were measured either by inversion freezing at 223 K or by line-shape analysis of VT NMR spectra, where the latter treatment yielded very accurate proton chemical

shifts. However, such a procedure was not possible for the complicated spectrum of **31** which has not been resolved into the composite spectra of the conformers. Hence, these results will not be discussed when the trends within the series are analyzed. In all of the following discussion, the differences that are smaller than 0.03 ppm have not been taken into consideration. With the exception of the H2 and H12 protons of **16**, and H11 and H12 proton of **31** calculated using B3LYP/Huz-IV, the calculated chemical shifts values for most of the aromatic protons are larger than the experimental ones. However, except the chemical shifts of H2 and H12 of **16** calculated using B3LYP/Huz-IV and of H3, H8 and H9 of **30** calculated using ωB97X-D/ccJ-pVTZ, the other calculated aromatic proton chemical shifts reproduce the experimental trends.

Logically, the aliphatic bridge proton positions with respect to the aromatic rings are more sensitive compared to those of the aromatic protons. Hence, it is difficult to find a simple relation between the experimental and calculated chemical shift values. Considering the complicated spectra of coupled dynamic spin systems that are highly sensitive to the position of the protons with respect to the aromatic rings, the reproduction of the experimental trends by the calculations is in most cases satisfactory. However, the differences between the calculated and experimental values in three cases are greater than or equal to 0.9 ppm, see for instance H15b of **16** calculated using ωB97X-D/Huz-IV, and H13a and H17o of **30**, both calculated using B3LYP/ccJ-pVTZ. The lengthening of the bridges affects the chemical shifts of the aliphatic protons in a complicated way and hence, no clear conclusion on the performance of the two basis sets could be reached. In most cases, when the bridge length increases the chemical shifts of the bridge protons that are neighboring the aromatic rings are larger than those further away from the aromatic rings. The exceptions are some calculated values for H16o of **30**, and some of those for H17o and H18o of **31**. The results of **16** and **30** show that the ethano-bridge proton chemical shifts decrease with decrease in temperature from 303 K to 223 K.

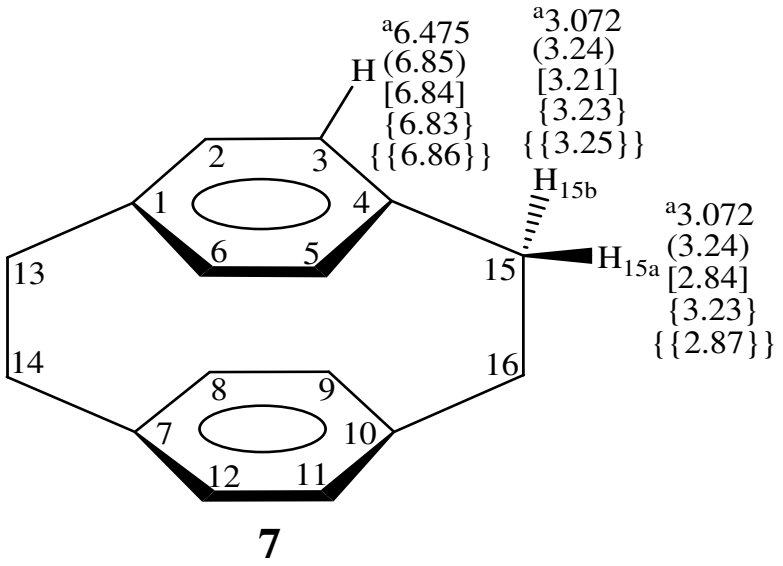

7

Fig. 27. ^{1}H chemical shifts (in ppm) of **7**: experimental values (this work, Chapter 5), no brackets; and calculated values using B3LYP/ccJ-pVTZ, in parenthesis; ωB97X-D/ccJ-pVTZ, in square brackets; B3LYP/Huz-IV, in curly brackets; and ωB97X-D/Huz-IV, in double curly brackets. The "a" superscripts represent experimental results measured at room temperature. The "a' and "b" subscripts refer to protons pointing out of the plane and inside the plane, respectively.

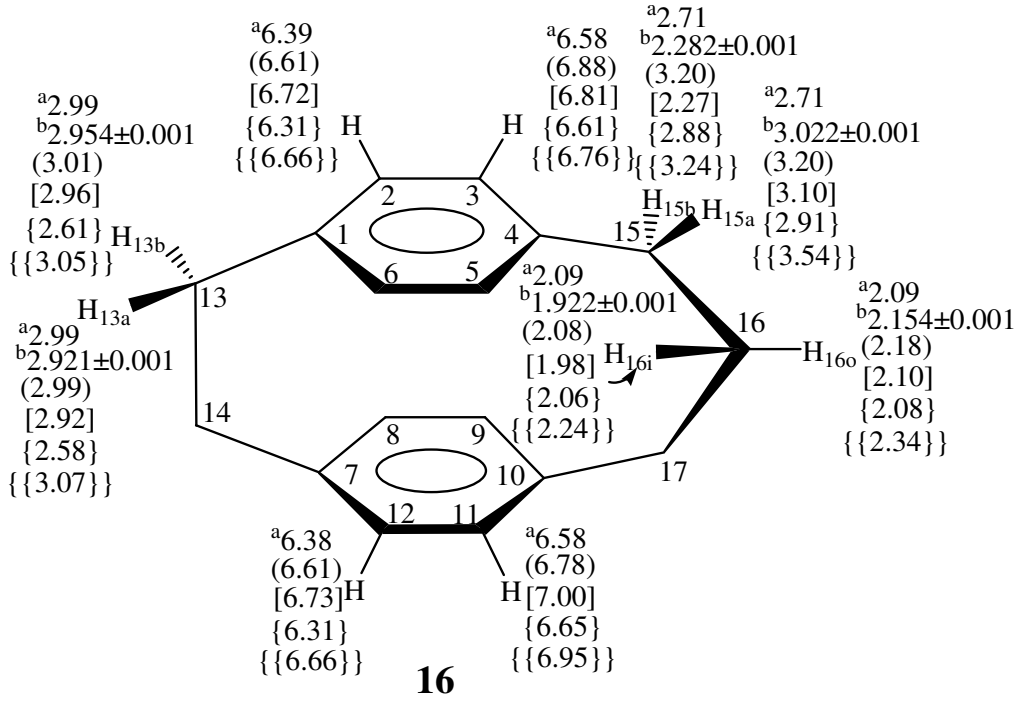

16

Fig. 28. ^{1}H chemical shifts (in ppm) of **16**: experimental values (this work), no brackets; and calculated values using B3LYP/ccJ-pVTZ, in parenthesis; ωB97X-D/ccJ-pVTZ, in square brackets; B3LYP/Huz-IV, in curly brackets; and ωB97X-D/Huz-IV, in double curly brackets. The "a" and "b" superscripts represent experimental results measured at 303 K and 233 K, respectively. The "a' and "b" subscripts refer to protons pointing out of the plane and inside the plane, respectively, whereas the "i' and "o" subscripts refer to protons pointing inside and outside of the aromatic rings, respectively.

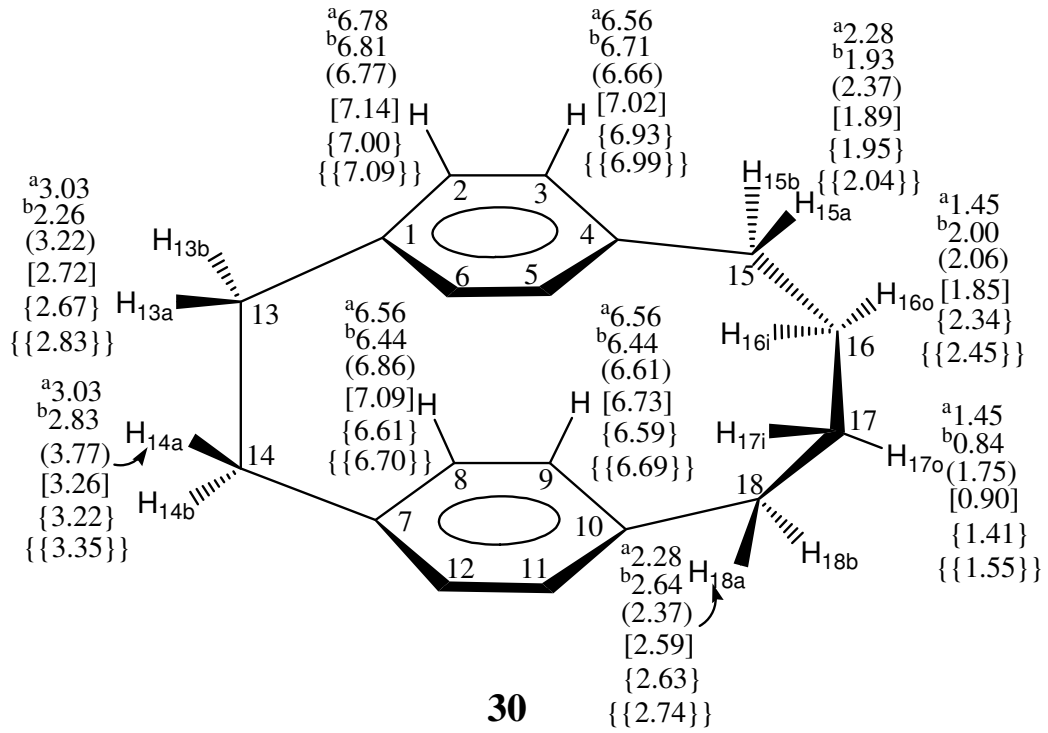

30

Fig. 29. ^{1}H chemical shifts (in ppm) of **30**: experimental values (this work), no brackets; and calculated values using B3LYP/ccJ-pVTZ, in parenthesis; ωB97X-D/ccJ-pVTZ, in square brackets; B3LYP/Huz-IV, in curly brackets; and ωB97X-D/Huz-IV, in double curly brackets. The "a" and "b" superscripts represent experimental results measured at 303 K and 233 K, respectively. The "a' and "b" subscripts refer to protons pointing out of the plane and inside the plane, respectively, whereas the "i' and "o" subscripts refer to protons pointing inside and outside of the aromatic rings, respectively. By symmetry, the chemical shifts of H16i are equal to those of H17o, and those of H17i are equal to those of H16o, whereas those of H15b are equal to those of H18a, and those of H18b are equal to those of H15a.

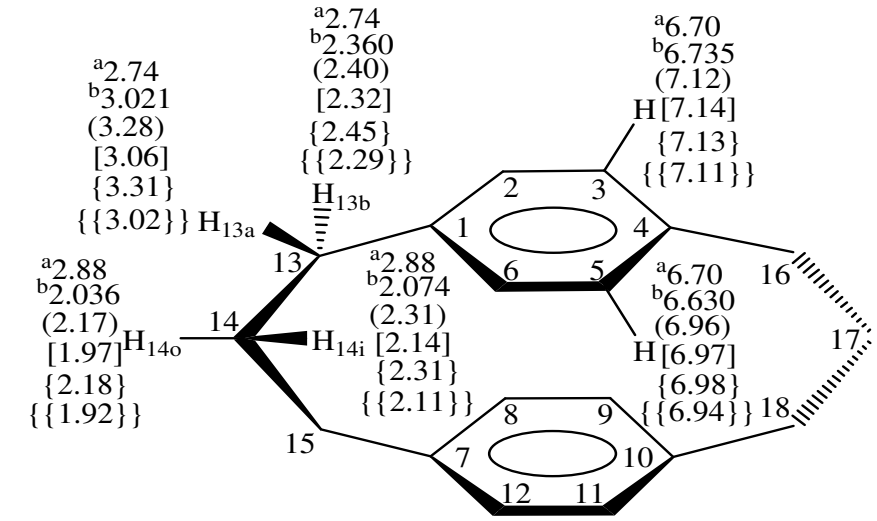

trans-**15**

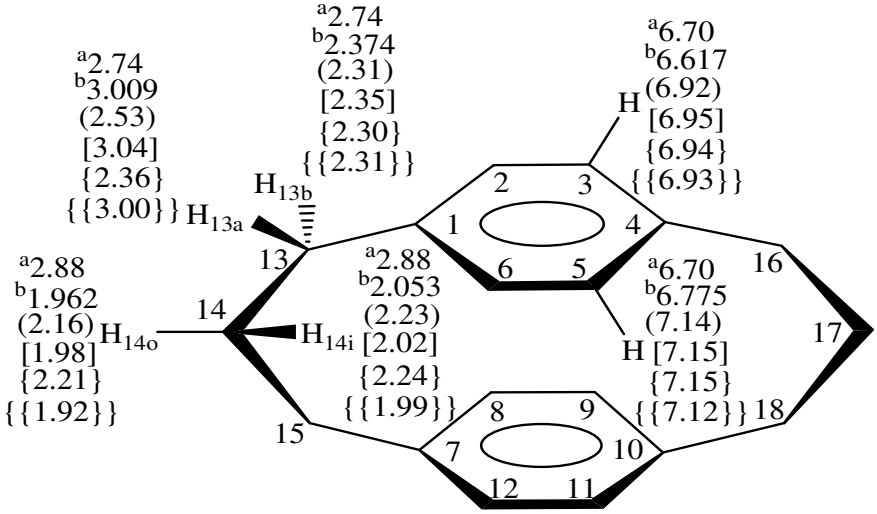

cis-**15**

Fig. 30. ^{1}H chemical shifts (in ppm) of **15**: experimental values,[15] no brackets; and calculated values using B3LYP/ccJ-pVTZ, in parenthesis; ωB97X-D/ccJ-pVTZ, in square brackets; B3LYP/Huz-IV, in curly brackets; and ωB97X-D/Huz-IV, in double curly brackets. The "a" and "b" superscripts represent experimental results measured at 303 K and 210 K,[15] respectively. The chemical shifts represented by "a" are averages of the *cis* and *trans* conformers at 303 K. The "a' and "b" subscripts refer to protons pointing out of the plane and inside the plane, respectively, whereas the "i' and "o" subscripts refer to protons pointing inside and outside of the aromatic rings, respectively.

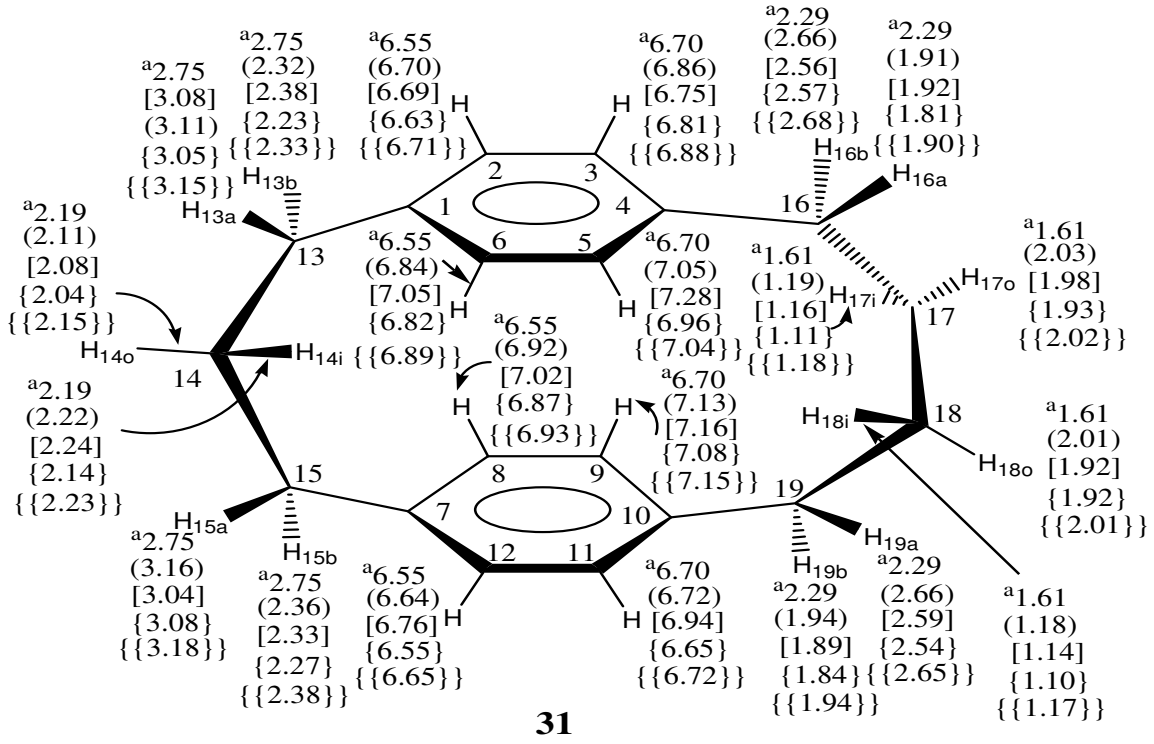

31

Fig. 31. ^{1}H chemical shifts (in ppm) of **31**: experimental values (this work), no brackets; and calculated values using B3LYP/ccJ-pVTZ, in parenthesis; ωB97X-D/ccJ-pVTZ, in square brackets; B3LYP/Huz-IV, in curly brackets; and ωB97X-D/Huz-IV, in double curly brackets. The "a" superscripts represent experimental results measured at 303 K and 223 K, respectively. The "a' and "b" subscripts refer to protons pointing out of the plane and inside the plane, respectively, whereas the "i' and "o" subscripts refer to protons pointing inside and outside of the aromatic rings, respectively.

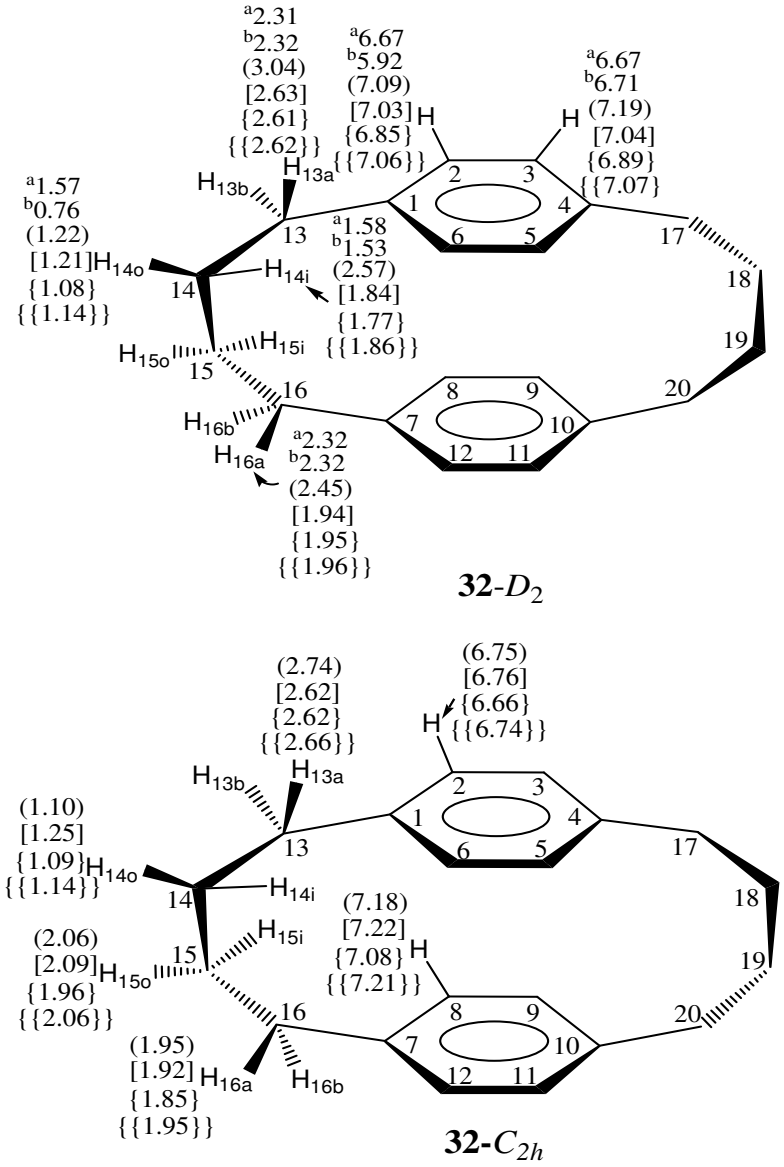

Fig. 32. ^{1}H chemical shifts (in ppm) of **32**-D_2 and **32**-C_{2h}: experimental values (this work), no brackets; and calculated values using B3LYP/ccJ-pVTZ, in parenthesis; ωB97X-D/ccJ-pVTZ, in square brackets; B3LYP/Huz-IV, in curly brackets; and ωB97X-D/Huz-IV, in double curly brackets. The "a" and "b" superscripts represent experimental results measured at 303 K and 223 K, respectively. The "a' and "b" subscripts refer to protons pointing out of the plane and inside the plane, respectively, whereas the "i' and "o" subscripts refer to protons pointing inside and outside of the aromatic rings, respectively. For **32**-D_2, by symmetry the chemical shifts of H15i are equal to those of H14o, and those of H15o are equal to those of H14i.

7.6. ^{13}C Chemical Shifts

The experimental and calculated ^{13}C chemical shifts are presented in Annex 9. All the calculated values reproduce the experimental trends, with the exception of δ(C13) for **16** calculated using B3LYP/ccJ-pVTZ and ωB97X-D/ccJ-pVTZ, δ(C5) for **30** calculated using B3LYP/ccJ-pVTZ, δ(C4) for *cis*-**15** calculated using ωB97X-D/ ccJ-pVTZ, and δ(C6) for **31** calculated using B3LYP/ccJ-pVTZ, ωB97X-D/ccJ-pVTZ, and B3LYP/Huz-IV. In both experimental and calculated (with one exception) values of the chemical shifts of the non-bridgehead aromatic carbon atoms are less than those of the aromatic bridgehead carbon atoms. The calculated values of the chemical shifts for the aromatic carbon atoms are always larger than the experimental ones, while for those of the aliphatic C14 carbon atoms of both isomers of **15** calculated using the B3LYP functional and both basis sets used are smaller than the experimental values. Remarkably, very small errors of less than 1 ppm for the calculated chemical shifts of C14 in *cis*-**15** were obtained using B3LYP/Huz-IV and for C6 of **30** using B3LYP/ccJ-pVTZ. On the other hand, most values of the aromatic carbon atom chemical shifts differ by more than 10 ppm and reach 18.5 ppm for C6 of **32**-D_2, for which the experimental spectrum of **32** with the freezed conformations could not be obtained. The inspection of the overall chemical shifts shows that no basis set or functional used in this work reproduces the experimental values significantly better than the others.

As expected, the chemical shifts of the bridge carbon atoms bonded to the aromatic rings are larger by *ca.* 5 ppm than the chemical shifts of other aliphatic carbon atoms. In addition, in agreement with expectation, the influence of the length of the second bridge on the chemical shifts of the ethano-bridge is small. For example, the calculated values of δ(C1) of **7**, **16** and **30** using ωB97XD/ccJ-pVTZ are 153.1, 150.4, and 150.5 ppm, respectively. For the central atom of the propano-bridge, slightly larger differences were observed (*e.g.* 32.6 ppm, 29.2 pm, 29.7 ppm, and 30.3 ppm were observed for C16 in **30**, C14 in *trans*- and *cis*-**15**, and C14 in **31**, respectively). Both the experimental and calculated chemical shifts of the non-bridgehead carbon atoms of **16** and **30**, C5 and C6 for example, decrease with an increase in the neighboring bridge length.

7.7. $^{n}J_{HH}$ Coupling Constants, n = 2 – 3

Selected $^{3}J_{HH}$ coupling constants of the bridges are listed in Table 12, whereas complete lists of $^{n}J_{HH}$ values are presented in Annex 10. The calculated values of most of the $^{3}J_{HH}$ coupling constants satisfactorily reproduced the experimental trends, except for **31** (for which the low temperature spectra with frozen conformational dynamics could not be interpreted). As expected, the $^{2}J_{HH}$ values are negative while those of $^{3}J_{HH}$ and $^{4}J_{HH}$ are positive. From the functionals/basis sets used, ωB97X-D/ccJ-pVTZ best reproduced the experimental $^{2}J_{HH}$ results, even though it failed for **31** for which the experimental data refer to the averaged spectrum. As it is clear from the structure of the molecules, the $^{3}J_{HH}$ coupling constants are of two types (a) those involving the aromatic protons, and (b) those involving the aliphatic protons. For the former ones, the coupling constants (*e.g.* for H2H3) are *ca*. 8 Hz. The $^{3}J_{HH}$ coupling constants involving the aliphatic carbon atoms are largest (*ca*. 12 Hz) for the torsional angle θ values close to zero or 180^{o} which is in agreement with the cosinusoidal Karplus relation.[158] On the other hand, the smallest $^{3}J_{HH}$ values less than 2 Hz are obtained for the calculated θ values of ±75^{o}. Many calculated values of $^{3}J_{HH}$ using ωB97X-D/ccJ-pVTZ are close to the experimental ones; however, its superiority is smaller than that found for the $^{2}J_{HH}$ value.

Table 12. $^{3}J_{HH}$ (in Hz): experimental values (**7**, **16**, **30**, **31** and **32** this work), no brackets; calculated values using B3LYP/ccJ-pVTZ in parenthesis; and ωB97X-D/ccJ-pVTZ in square brackets. Torsional angles θ (in degrees) are extracted from the ωB97X-D/ccJ-pVTZ optimized structures.

	7		**16**		**30**		*trans*-**15**[15]		*cis*-**15**[15]		**31**		**32**-D_2	
	$^{3}J_{HH}$	θ	$^{3}J_{HH}$	θ	$^{3}J_{HH}$	θ	$^{3}J_{HH}$	θ	$^{3}J_{HH}$	θ	$^{3}J_{HH}$	θ	$^{3}J_{HH}$	θ
H13aH14a	10.65 (10.22) [11.09]	[17.2]	12.31 (10.35) [12.12]	[0.0]	nm (9.11) [9.54]	[31.9]	-	-	-	-	-	-	-	-
H13aH14b	4.15 (2.33) [2.89]	[98.2]	3.51 (2.22) [2.89]	[-117.0]	nm (7.98) [9.85]	[147.8]	-	-	-	-	-	-	-	-
H13bH14a	4.15 (2.81) [6.34]	[132.0]	5.03 (4.73) [5.24]	[117.0]	nm (7.98) [9.85]	[147.8]	-	-	-	-	-	-	-	-
H13bH14b	10.65 (10.22) [11.09]	[17.2]	2.61 (2.81) [2.62]	[66.2]	nm (9.11) [9.54]	[31.9]	-	-	-	-	-	-	-	-
H13aH14i	-	-	-	-	-	-	3.24 (2.80) [3.08]	[-65.6]	2.94 (2.62) [2.89]	[-65.9]	3.10(5) (2.89) [2.99]	[-64.4]	1.83 (1.31) [1.59]	[-75.8]
H13aH14o	-	-	-	-	-	-	4.36 (4.65) [5.09]	[48.5]	4.81 (4.83) [5.28]	[48.2]	3.90(5) (4.68) [4.84]	[50.5]	5.14 (6.64) [6.78]	[37.6]
H13bH14i	-	-	-	-	-	-	12.77 (11.84) [12.82]	[179.7]	13.13 (11.73) [12.71]	[179.3]	13.32(5) (11.23) [12.36]	[179.0]	12.67 (10.36) [12.09]	[166.0]
H13bH14o	-	-	-	-	-	-	2.42 (2.46) [2.69]	[-66.2]	2.64 (2.31) [2.53]	[-66.6]	2.69(5) (2.69) [2.93]	[-64.4]	1.63 (1.54) [1.55]	[-75.8]

θ is the dihedral angle between the protons. For **31** and **32** 'a' refers to protons close to the region between the rings, and 'b' to those outside of the rings. For details of the orientation of the protons and all $^{n}J_{HH}$ values, see Annex 10.

7.8. $^{n}J_{CH}$ Coupling Constants, n = 2 – 3

The available experimental and calculated values of the $^{1}J_{CH}$ coupling constants are listed in Annex 11. Except for $^{1}J_{C2H2}$ calculated at the B3LYP/Huz-IV level, the calculated $^{1}J_{CH}$ values are always smaller than the corresponding experimental ones; however, in most cases they reproduce the experimental trends. The deviations from the experimental values are largest for the ωB97X-D/Huz-IV calculations. Remarkably, B3LYP/Huz-IV reproduced the values with the smallest errors. Since the experimental values of $^{n}J_{CH}$ for n>1 could not be measured, the trends of the calculated values, listed in Annex 12, will be discussed only briefly. In agreement with expectations, all the calculated $^{2}J_{CH}$ values are negative and those involving C_{sp2} atoms are larger than the others by *ca*. 2 Hz. On the other hand, all the calculated $^{3}J_{CH}$ values are positive. In most cases, the values calculated using different functionals/basis sets differ by less than 1 Hz. As earlier, the $^{3}J_{CH}$ values involving the bridge protons are highly directional. Some of them have the highest values while others are the lowest.

7.9. $^{n}J_{CC}$ Coupling Constants, n = 2 – 3

The available experimental and calculated values of the $^{1}J_{CC}$ coupling constants are collected in Annex 13. Most calculated values of $^{1}J_{CC}$ reproduce the experimental trends. However, none of the combinations of functionals and basis sets yields considerably better results than the others in spite of the fact that the ccJ-pVTZ basis set has been especially designed for the calculation of coupling constants. The calculated values of the $^{1}J_{CC}$ and $^{3}J_{CC}$ coupling constants are positive, whereas most of the $^{2}J_{CC}$ and $^{4}J_{CC}$ coupling constants are negative (Annex 14). Comparing the $^{1}J_{CC}$ values involving C_{sp2} and C_{sp3} carbon atoms shows that those on the side of the ethano-bridge are larger than those on the side of the propano- and butano-bridges of **16** and **30**, respectively. In the same way, the values of the $^{1}J_{CC}$ coupling constants of $C_{sp2}C_{sp3}$ in **31** from the side of the shorter propano-bridge are larger than those from the side of the butano-bridge. For example, the experimental value for $^{1}J_{C7C15}$ is 43.8 Hz, whereas $^{1}J_{C10C19}$ is 38.1 Hz. The $^{1}J_{CC}$ values between the bridgehead carbon atoms and the bridge sp^3 hybridized carbon atoms have larger values compared to the aromatic ring $^{1}J_{CC}$ coupling constants. For instance, the ωB97X-D/ccJ-pVTZ calculated value of $^{1}J_{C2C3}$ of **31** is 57.2 Hz, whereas its $^{1}J_{C7C15}$ is 42.5 Hz.

The experimental $^2J_{CC}$ and $^3J_{CC}$ coupling constants could not be measured, and hence, only the trends in the calculated values will be discussed briefly. The $^2J_{CC}$ values involving $C_{sp2}C_{sp2}C_{sp3}$ carbon atoms are positive and slightly larger in absolute values than the other $^2J_{CC}$ values, while the others are negative. The $^3J_{CC}$ values, which are all positive, fall into three groups (a) *ca*. 9 Hz between the $C_{sp2}C_{sp2}C_{sp2}C_{sp2}$ carbon atoms (b) *ca.* 3.5 Hz between the $C_{sp2}C_{sp2}C_{sp2}C_{sp3}$ carbon atoms and (c) smaller than 2 Hz between the $C_{sp2}C_{sp2}C_{sp3}C_{sp3}$ carbon atoms. In the first group, one can approximately differentiate between the smaller coupling constants between the bridgehead carbon atoms and the other.

7.10. Absorption and Emission Spectra and Excited State Structures

Absorption and emission spectroscopic studies of **7** and **15** have been reported.[36,37,118,119,121,122,154] Among these reports, Shen *et al.*[36] published the absorption spectrum for the transition to the first excited state of **7** in the region between 307 and 326 nm. Melzer *et al.*[119] studied the excited triplet state of **7** and **15** and found the maximum emission wavelength for both molecules to be between 475 and 485 nm. The two-photon absorption spectrum of crystalline **7** has been reported by Fuke *et al.,*[31] who assigned the two absorption bands in the region between 288.2 and 273.97 nm to the two even-parity allowed $^1B_{1g} \leftarrow {}^1A_{lg}$ and $^1B_{2g} \leftarrow {}^1A_{1g}$ transitions. Recently Shirai *et al*.[28] reported an *ab initio* molecular orbital study in the excited states of **7** and **15**. The authors showed that the equilibrium distances between the benzene rings in the first excited states were shorter than those in the ground states.

7.10.1. Interring Separation, Ring Deformation and Twist Angle in the Excited State

The interring separation distances, ring deformation and twist angles in the excited state are collected in Table 13. The results show that the separation distances between the aromatic bridgehead carbon atoms of all the molecules decrease in the excited state compared to the ground-state geometries by *ca.* 0.2 - 0.9 Å, in which the largest change is observed for **32**. The trends of C2C1C6C5 ring deformation angles observed for the ground state are also observed in

the excited state. For **16**, the same torsional angle calculated using ωB97X-D decreases to -9.5°, while it is -11.7° in the ground state structure. The same deformation angle obtained using the same functional for **30** in the excited state is -6.3°. For **31** the ring deformation angle in the excited state decreases to -1.2° compared to the ground state (-4.9°). Remarkably, the rings of both conformers of **32** are bent in opposite directions, which is not the case of the other molecules. The C2C1C6C5 torsional angle of the two conformers of **32** is positive, while those of **7**, **15**, **16**, **30** and **31** have negative values. The twist angle (C1C13C14C7) of the aromatic rings of **7** obtained from ωB97X-D optimization decreases to -11.6° compared to the ground-state geometry (-14.9°), whereas that of **16** remains unchanged (0°). Unlike in **7** and **16**, the C1C13C14C7 twist angle of **30** is much larger, being 28.5° in the ground state and 15° in the excited state. Comparable values have been obtained for the C4C1C7C10 angle in the first excited state of **15** and **32**-D_2 and also to a smaller extent in **31**. However, **32**-C_{2h} is exceptional with considerably larger value.

Table 13. Calculated distances (in Å) between the corresponding non-bonded carbon atoms, ring deformation angle, and twist angles (in degrees) of the two aromatic rings in the excited state calculated using B3LYP/ccJ-pVTZ, in parentheses; and ωB97X-D/ccJ-pVTZ, in square brackets.

	7	**16**	**30**	*trans*-**15**	*cis*-**15**	**31**	**32**-C_{2h}	**32**-D_2
C1C7	(2.643)	(2.636)	(2.600)	(2.891)	(2.956)	(2.875)	(3.212)	(3.170)
	[2.615]	[2.604]	[2.573]	[2.839]	[2.861]	[2.821]	[3.186]	[3.132]
C2C8	(2.943)	(2.945)	(2.927)	(3.130)	(3.069)	(3.053)	(3.142)	(3.136)
	[2.906]	[2.900]	[2.907]	[2.989]	[3.018]	[2.963]	[3.108]	[3.101]
C3C9	(2.943)	(3.077)	(3.311)	(3.138)	(3.069)	(3.272)	(3.142)	(3.136)
	[2.906]	[3.030]	[3.293]	[3.003]	[3.018]	[3.173]	[3.108]	[3.101]
C4C10	(2.643)	(2.980)	(3.412)	(2.891)	(2.956)	(3.365)	(3.212)	(3.170)
	[2.615]	[2.931]	[3.394]	[2.939]	[2.861]	[3.289]	[3.186]	[3.132]
C5C11	(2.943)	(3.135)	(3.310)	(3.130)	(3.108)	(3.272)	(3.142)	(3.136)
	[2.906]	[3.061]	[3.220]	[2.989]	[3.102]	[3.172]	[3.108]	[3.101]
C6C12	(2.943)	(2.944)	(2.926)	(3.138)	(3.108)	(3.020)	(3.142)	(3.136)
	[2.906]	[2.887]	[2.903]	[3.003]	[3.102]	[2.954]	[3.108]	[3.101]
C2C1C6C5	(-13.9)	(-9.9)	(-6.5)	(-6.1)	(-6.1)	(-1.8)	(3.2)	(2.1)
	[-13.6]	[-9.5]	[-6.3]	[-6.2]	[-6.2]	[-1.2]	[3.1]	[2.1]
C1C13C14C7	(0.0)	(0.0)	(-15.1)	-	-	-	-	-
	[-11.6]	[0.0]	[-17.6]					
C4C1C7C10	(0.0)	(0.0)	(7.1)	(0.0)	(0.0)	(-0.9)	(-12.6)	(0.0)
	[-4.9]	[0.0]	[10.7]	[0.0]	[0.0]	[-0.4]	[-13.3]	[0.0]

7.10.2. Absorption Spectra

The experimental absorption spectra of the paracyclophanes studied in this chapter are plotted in Fig. 33, while the calculated and observed absorption bands (labeled using Roman numbers) are collected in Table 14. In molecules **7**, **16** and **30**, the absorption spectra calculated using both functionals show the presence of multiple transitions in the region inaccessible to our spectrometer below 200 nm. There are five absorption bands for **7**. However, Iwata *et al.*[118] observed an additional sixth band at 188.7 nm. From the calculations, six bands are predicted for **7**, one below 200 nm which could not be observed experimentally (band VI of the highest calculated intensity) since its calculated excitation energy is outside the range of our

spectrophotometer. The shoulder on the low-energy side of band IV corresponds to band III. Band V is a lower-energy shoulder to band VI. As discussed above, because of the D_{2h} symmetry in the optimized geometry of **7** using the CAM-B3LYP functional, only B_{1u}, B_{2u}, and B_{3u} transitions are allowed, whereas for the D_2 symmetry, which is obtained from wB97X-D optimization, also B_1, B_2 and B_3 transitions are symmetry-allowed and can show non-zero intensity.

The experimental spectrum of **16** shows the presence of five electronic transitions in the frequency range of the spectrophotometer. Band V is the most intense transition located at 216 ± 2 nm. On the other hand, band I observed at 303 ± 2 nm is the weakest. The calculations predict that the low-energy transition is the least intense one, whereas the most intense transition should be lying outside the experimentally accessible frequency range, the higher-energy transition band labeled as VII, located at 177 nm. The most intense absorption band above 200 nm of the calculated spectrum using the ωB97X-D is located at 217 nm, in agreement with the experimental result. With regard to the absorption spectrum of **30,** the experimental results display four electronic transitions, of which band III at 215 ± 2 nm is the most intense transition above 200 nm. The calculated results obtained from CAM-B3LYP and ωB97X-D functionals are reliable, albeit they differ somewhat in the high-energy region. The intense transition in the experiment is well reproduced by both functionals (214 nm and 215 nm using CAM-B3LYP and ωB97X-D, respectively).

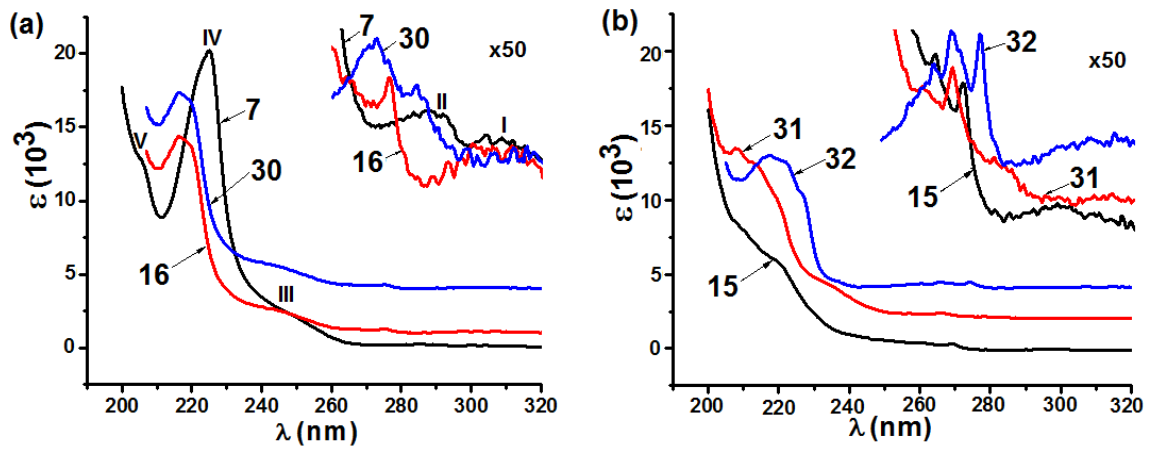

Fig. 33. Absorption spectra: (a) of **7**, **16**, and **30**, (b) of **15**, **31** and **32** measured in n-hexane (this work). The Roman numbers refer to the transitions in **7**. For the sake of clarity, the absorption spectra of **16** and **30** are shifted up with respect to that of **7** by $1x10^3$ and $4x10^3$, respectively; and similarly those of **31** and **32** are shifted up with respect to that of **15** by $2x10^3$ and $4x10^3$, respectively.

As highlighted in the Introduction, **15** has two non-equivalent conformers, one with C_{2h} symmetry (*trans*-**15**) and another with C_{2v} symmetry (*cis*-**15**). The *cis* conformer is dominant in solution.[15] Computationally, both conformers were analyzed and comparisons made between the calculated spectra of each conformer with the experimental spectrum. The experimental absorption spectrum of **15** shows that there are two bands located at 269 ± 2 nm and 261 ± 2 nm. On the basis of the calculations, these two absorption bands are assigned to a single electronic transition. However, this allowed transition of **15** does not exist in the calculated spectrum of *trans*-**15**, but appears in *cis*-**15** which supports the existence of the *cis*-**15** conformer as the dominant conformer in solution.[15] The most intense transition observed experimentally at 220 ± 2 nm is reproduced by the calculated results for the *cis*-**15** case, 217 nm, which is not allowed in the case of *trans*-**15**. There are also two other allowed transitions in the calculated spectra of both conformers which are not observed in the experimental spectrum since they lie in the high-energy region below 200 nm inaccessible for our apparatus. These transitions are predicted to lie

between 175 nm and 200 nm, of which those located at 177 nm for both conformers are the most intense in this high-energy region. The overall comparison of the experimental and calculated spectra shows that the calculated absorption spectrum obtained for *cis*-**15** is in a good agreement with the experimental spectrum.

As pointed out above, **31** has two energetically equivalent conformers, thus identical calculated absorption spectra were obtained. Its experimental spectrum in Fig. 33 shows a maximum absorption wavelength at 213 ± 2 nm. This agrees well with the calculated absorption spectra using the CAM-B3LYP functional, where the most intense peak is found at 214 nm. The calculated spectrum using the ωB97X-D functional gave a maximum absorption at 210 nm. The other intense absorption peak is observed at 208 ± 2 nm in the experimental spectrum, 211 nm and 208 nm using CAM-B3LYP and ωB97X-D functionals, respectively. At the region below 200 nm, the calculated spectrum using CAM-B3LYP shows an intense transition at 178 nm whereas the one using ωB97X-D appears at 176 nm. For **15**, the intense absorption band is located at 220 ± 2 nm, whereas it is blue-shifted to 208 ± 2 nm for **31**.

The measured spectrum of **32** shows an absorption maximum at 217 ± 2 nm. The calculated absorption maximum for the C_{2h} conformer using the CAM-B3LYP functional is 213 nm (A_u) to be compared to 214 nm (B_3) for the D_2 conformer. From these calculated bands of the two conformers, the one for the C_{2h} structure is more intense than that of the D_2 conformer. There are two additional allowed absorption bands for the D_2 conformer, whereas they are not allowed for the C_{2h} conformer. In the experimental spectrum, band IV is located at 226 ± 2 nm. This absorption band (A_g) is forbidden for the C_{2h} conformer but allowed for the D_2 conformer (B_3). These results indicate that in solution, the D_2 conformer is dominant. This observation is in excellent agreement with the optimized geometry obtained in this work, as well as with the X-ray structure reported by Jones *et al.*[42] The experimental as well as the calculated spectra highlight the effects of the bridge lengths on the absorption spectra of the molecules. As can be seen from Table 14, both functionals reproduce the absorption wavelengths of all the paracyclophanes studied fairly well.

Table 14. Observed and calculated electronic transitions (in nm), and oscillator strengths 'f' of **7**, **15**, **16** and **30** - **32**: experimental results, no brackets; calculated values using CAM-B3LYP/aug-cc-pVTZ, in parenthesis; and ωB97X-D/aug-cc-pVTZ in square brackets.

Band	**7**	**16**	**30**	*trans*-**15**	*cis*-**15**	**31**	**32**-C_{2h}	**32**-D_2
	300 ± 2	303 ± 2	302 ± 2	-	294 ± 2	312 ± 2	-	306 ± 2
I	-	-	-	-	-	-	-	-
	-	-	-	-	-	-	-	-
	285 ± 2	275 ± 2	271 ± 2	-	269 ± 2	266 ± 2	-	274 ± 2
	(B_{1u} 268.8	(A" 268.0	(A 246.9	(B_g 268.1	(B_1 266.8	(A 250.9	-	-
II	f=0.0009)	f=0.0006)	f=0.0004)	f=0.0000)	f=0.0011)	f=0.0003)	-	-
	[B_3 272.3	[A" 269.2	[A 247.6	[B_g 269.8	[B_1 265.9	[A 249.3	-	-
	f=0.0009]	f=0.0001]	f=0.0004]	f=0.0000]	f=0.0010]	f=0.0003]		
	257 ± 2	244 ± 2	-	-	-	220 ± 2	-	265 ± 2
	(B_{1u} 251.9	(A" 239.7	(B 239.0	(B_u 234.0	(A_1 233.5	(A 231.2	-	-
III	f=0.0022)	f=0.0035)	f=0.0043)	f=0.0070)	f=0.0026)	f=0.0060)	-	-
	[B_1 254.7	[A' 239.0	[B 237.9	[B_u 236.2	[A_1 235.8	[A 232.5	-	-
	f=0.0014]	f=0.0040]	f=0.0048]	f=0.0071]	f=0.0028]	f=0.0046]		
	225 ± 2	216 ± 2	215 ± 2	-	220 ± 2	214 ± 2	-	226 ± 2
	(B_{3u} 222.5	(A' 216.6	(A 214.3	(B_u 217.4	(B_1 222.9	(A 214.0	(A_g 234.0	(B_3 234.2
IV	f=0.1198)	f=0.1031)	f=0.1010)	f=0.0614)	f=0.0010)	f=0.0638)	f=0.0000)	f=0.0011)
	[B_1 244.3	[A' 213.0	[A 214.6	[B_u 218.1	[B_1 224.9	-	[A_g 236.1	[B_3 234.1
	f=0.0023]	f=0.1072]	f=0.1031]	f=0.0612]	f=0.0011]		f=0.0000]	f=0.0009]
	206 ± 2	207 ± 2	206 ± 2	-	208 ± 2	208 ± 2	-	222 ± 2
	(B_{1u} 211.0	(A" 208.4	(B 211.5	(B_u 203.0	(B_2 202.0	(A 210.8	(B_u 232.9	(B_1 233.4
V	f=0.1474)	f=0.008)	f=0.0196)	f=0.0309)	f=0.0280)	f=0.0110)	f=0.0056)	f=0.0047)
	[B_3 218.1	-	[B 211.1	[B_u 202.9	[B_2 202.6	[A 210.4	[B_u 232.1	[B_1 232.9
	f=0.1272]		f=0.0946]	f=0.0310]	f=0.0281]	f=0.0627]	f=0.0053]	f=0.0051]
	188.7[118]	-	-	-	-	-	-	217 ± 2
	(B_{2u} 196.3	(A' 201.3	(B 203.7	(B_u 195.9	(A_1 197.1	(A 200.9	(A_u 213.8	(B_3 212.0
VI	f=0.0302)	f=0.1269)	f=0.0095)	f=0.0702)	f=0.0975)	f=0.0131)	f=0.1111)	f=0.1081)
	[B_2 197.0	[A' 198.3	[B 209.7	[B_u 198.7	[A_1 199.1	[A 203.9	[A_u 208.8	[B_3 210.4
	f=0.0356]	f=0.1112]	f=0.0945]	f=0.0611]	f=0.0980]	f=0.0044]	f=0.1035]	f=0.0958]
	-	-	-	-	-	-	-	-
	-	(A' 196.0	(B 197.6	(B_u 176.8	(B_2 176.5	(A 178.0	(B_g 202.0	(B_1 201.2
VII	-	f=0.0386)	f=0.1341)	f=0.6624)	f=0.7072)	f=0.5101)	f=0.0000)	f=0.0020)
	-	[A' 192.2	[B 198.7	[B_u 177.9	[B_2 176.9	[A 175.7	[B_g 194.2	[B_1 195.8
		f=0.0990]	f=0.0032]	f=0.6544]	f=0.7070]	f=0.6311]	f=0.0001]	f=0.0017]
	-	-	-	-	-	-	-	-
	-	(A' 177.1	(A 180.2	-	-	-	(A_u 178.9	(B_3 177.2
VIII	-	f=0.7874)	f=0.3687)	-	-	-	f=1.0303)	f=0.7342)
	-	[A' 175.2	[A 176.7	-	-	-	[A_u 177.2	[B_3 176.5
		f=0.7119]	f=0.4536]				f=1.1610]	f=0.9711]

7.10.3. Emission Spectra

The emission spectra of **7**, **16**, **30**, **15**, **31**, and **32** are plotted in Fig. 34 and emission wavelengths listed in Table 15. The results show that the experimental emission band of **7** is located at 351 ± 2 nm, whereas the corresponding calculated value using the ωB97X-D functional is 314 nm. For **16** it is located at 355 ± 2 nm in the experimental emission spectrum, whereas the calculated value using the ωB97X-D functional is 313 nm. The measured emission wavelength of **30** is 330 ± 2 nm, which is blue-shifted compared to **7** and **16**. The corresponding calculated emission wavelength of **30** using the ωB97X-D functional is 286 nm. The measured emission band of **15** is located at 381 ± 2 nm, whereas the ωB97X-D calculated emission wavelength of *trans*-**15** is 324 nm whereas that of *cis*-**15** is 330 nm. Similarly, the experimental emission bands of **31** and **32** are observed at 357 ± 2 nm and 331 ± 2 nm, respectively. The corresponding calculated value using the ωB97X-D functional for **31** is 303 nm, whereas it is 293 nm for **32**-D_2 and 306 nm for **32**-C_{2h}. Except for the very close values for **7** and **16**, both the experimental and calculated emission wavelengths for [2.*n*]- and [*m,n*]paracyclophanes with *m, n* = 3, 4 exhibit the same trend with the bridge(s) lengthening resulting in the lowering of the emission wavelength in both series.

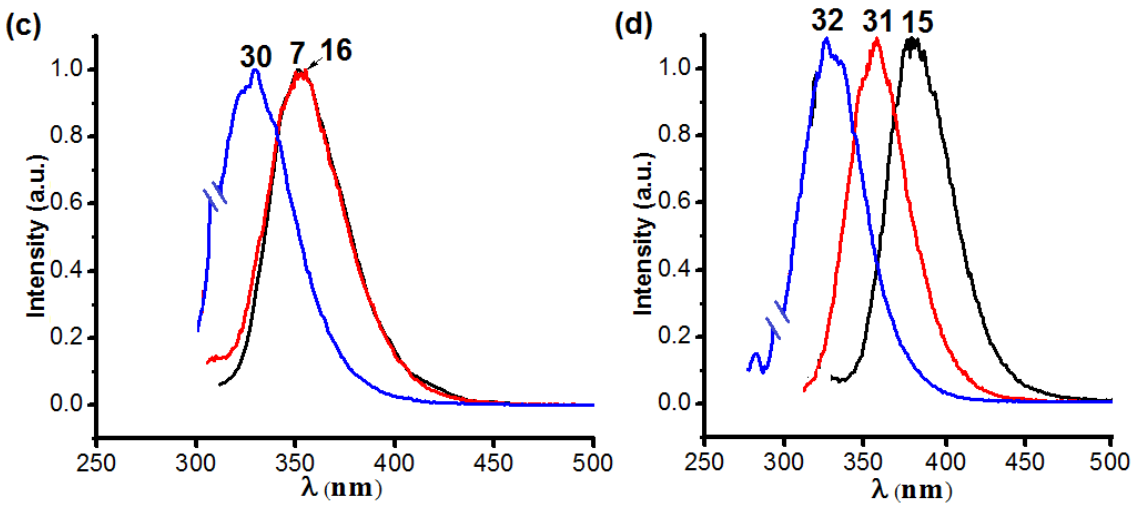

Fig. 34. Emission spectra: (a) of **7**, **16**, and **30**, (b) of **15**, **31** and **32** measured in n-hexane (this work). The emission spectra were measured at λ_{ex}(**7**) = 244 nm, λ_{ex}(**16**) = 275 nm, λ_{ex}(**30**) = 282 nm, λ_{ex}(**15**) = 268 nm, λ_{ex}(**31**) = 265 nm and λ_{ex}(**32**) = 274 nm.

Table 15. Observed and calculated emission wavelengths (in nm) of **7**, **15**, **16** and **30** – **32**: experimental results (this work), no brackets; calculated values using CAM-B3LYP/aug-cc-pVTZ, in parenthesis; and ωB97X-D/aug-cc-pVTZ in square brackets.

7	**16**	**30**	*trans*-**15**	*cis*-**15**	**31**	**32**-C_{2h}	**32**-D_2
351 ± 2	355 ± 2	330 ± 2	-	381 ± 2	357 ± 2	-	331 ± 2
(312.8)	(312.1)	(284.2)	(323.1)	(328.9)	(301.6)	(304.4)	(292.1)
[314.0]	[313.0]	[286.0]	[324.0]	[330.0]	[303.0]	[306.0]	[293.0]

7.11. Conclusion

In this chapter, the geometry of [*m.n*]paracyclophanes (*m*, *n* = 2 – 4) were optimized using a combination of B3LYP and ωB97X-D functionals and ccJ-pVTZ and Huz-IV basis sets. As discussed in detail in the previous chapters, the B3LYP optimized structure of [2.2]paracyclophane has the C1C13C14C7 torsional angle close to 0^o (D_{2h} symmetry). On the other hand, the one obtained from the optimized geometry using the ωB97X-D functional has a

torsional angle of 14.9° (D_2 symmetry). The most recent experimental results reported by Lyssenko *et al.*[20] favor the D_{2h} structure, even though the D_2 structure cannot be disregarded. As has been discussed in the introduction as well as in Chapter 5, the inspection of the data collected in the Cambridge Data Base for numerous closely related cyclophanes indicates torsional angles smaller than 6°. With the exception of the C1C13C14C7 angle, the ωB97X-D functional gave structural parameters that are in fair agreement with the available experimental results. Understandably, unlike those of **7**, **15**, and **32**, the average planes of the rings of **16**, **30**, and **31** are not parallel. The C1…C7 and C4…C10 bridgehead-bridgehead interring separation distances are smaller than the sum of the van der Waals radii of the carbon atoms, that is 3.4 Å for the bridges having less than four carbon atoms.

The calculated values of the chemical shifts and proton-proton coupling constants of all the [*m.n*]paracyclophanes were compared with the very accurate ones obtained from the NMR spectra. The study of the temperature effects on the proton chemical shifts indicated that the chemical shifts of the ethano-bridge protons decrease when the temperature decreases. The comparison between the experimental and calculated values shows that with several exceptions, the calculated values of the chemical shifts and coupling constants reproduce the experimental trends. The results obtained using different basis sets show that no general conclusion on the performance of the two basis sets can be reached for the proton and carbon chemical shifts. On the other hand, the ωB97X-D/ccJ-pVTZ method best estimated the $^2J_{HH}$ coupling constants, however, no general conclusion on the performance functional/basis set in the calculation of coupling constants could be achieved.

Experimental and computational studies of the absorption and emission properties of the [*m.n*]paracyclophanes were also performed. The absorption and emission properties of the paracyclophanes showed a noticeable effect of the bridge lengths on the electronic properties. The excited-state optimized geometries showed that the interring separation distances between the aromatic bridgehead carbon atoms of all the [*m.n*]paracyclophanes in the excited state decrease by *ca.* 0.2 - 0.9 Å compared to the corresponding ground state geometries. There are six absorption bands for **7**. The observation of these bands shows that the bands which are forbidden for the high-symmetry structure (D_{2h}) are allowed in the twisted structure (D_2).

Chapter 8

Summary

8.1. In Chapter 5, the structural and NMR parameters of [2.2]paracyclophane **7** and its derivatives: phenyl-[2.2]paracyclophane **17**, benzene[2.2]paracyclophane **18**, and *trans*-[2.2]naphthalenophane **19** are presented. The optimized geometry of **7** obtained from the B3LYP functional has D_{2h} symmetry with no disorder. Even though the symmetry and the C1C13C14C7 twist angle obtained from the calculations agree with the low-temperature X-ray result measured at 100 K,[20] the other structural parameters, especially the interring separation distances, deviate from the corresponding experimental values. The twist angle obtained from the B3LYP geometry optimization is also in strong disagreement with most published theoretical results.[14,22]

Accurate proton chemical shifts and $^{n}J_{HH}$, n = 2 – 3, coupling constants of the bridges were measured. For the NMR calculations two basis sets, Huz-IV and 6-311G(d,p), combined with B3LYP functional were used. The results reveal that, in most cases, the 6-311G(d,p) basis set reproduces fairly well the proton chemical shifts. However, such a simple conclusion could not be drawn for the carbon chemical shifts. Concerning the coupling constants, Huz-IV accurately reproduced the experimental values compared to 6-311G(d,p) with the exception of $^{1}J_{C13H13a}$, $^{1}J_{C14H14a}$ and $^{1}J_{C16H16a}$ of **17**. The nonplanar benzene ring distortions and the proximity of the rings have effects on the carbon and aliphatic proton chemical shifts. The vicinal coupling constants in the aliphatic bridges of **7**, **17** and **18** were found to be temperature-dependent indicating the presence of a low-frequency twisting/rocking mode in these compounds.

8.2. In Chapter 6, the molecular geometries of [2.2]paracyclophan-13-ene **20**, [2.2]paracyclophan-13,15-diene **9**, 13-vinyl-[2.2]paracyclophan-13-ene **21**, [2.2.2](1,2,4)-cyclophan-15-ene **22**, [2.2.2](1,2,4)-cyclophan-17-ene **23**, [2.2.2](1,2,4)cyclophan-13-ene **24**, [2.2.2](1,2,4)cyclophan-13,15-diene **25**, [2.2.2](1,2,4)cyclophan-13,17-diene **26**, [2.2.2](1,2,4)cyclophan-15,17-diene **27**, [2.2.2](1,2,4)cyclophan-13,15,17-triene **28**, with [2.2]paracyclophane **7** and [2.2.2](1,2,4)cyclophane **29** added for the sake of comparison, were

optimized using B3LYP/6-311++G(2d,2p), ωB97X-D/6-311++G(2d,2p) and ωB97X-D/cc-pVQZ methods. The optimized structural parameters are compared with the available experimental results. The results show that the central bridge bonds are sensitive to the computational methods applied. These bonds are better reproduced using the ωB97X-D functional than B3LYP irrespective of the basis set used. The distances between the corresponding atoms of the two aromatic rings are much better reproduced using ωB97X-D/6-311++G(2d,2p) and ωB97X-D/cc-pVQZ than the other methods. Satisfactory results were also obtained for the bond and torsional angles.

The results of the chemical shifts from different computational levels usually show the same trends. Hence, the calculated values are believed to correctly describe the experimental chemical shifts and coupling constants that could not be measured for the known and the hypothetical molecules. Among the different computational methods employed for the NMR parameter calculations, the B3LYP/6-311G(d,p) NMR calculations on the structure optimized using ωB97X-D/cc-pVQZ are the best. However, in contrast to the geometry optimizations, the agreement between the values of the NMR parameters obtained from the ωB97X-D/cc-pVQZ calculations and the corresponding experimental ones are usually the poorest compared to those obtained from the ωB97X-D/6-311++G(2d,2p) NMR parameter calculations. Of the two functionals used, B3LYP performed poorly for the geometry optimizations compared to ωB97X-D functional, which can be due to the over-repulsive nature of the former functional in the van der Waals region, whereas it gives better NMR parameters if the geometry is optimized using the ωB97X-D functional.

8.3. In Chapter 7, the geometry of [2.2]paracyclophane **7**, [2.3]paracyclophane **16**, [2.4]paracyclophane **30**, [3.3]paracyclophane **15**, [3.4]paracyclophane **31**, and [4.4]paracyclophane **32** were optimized using the B3LYP and ωB97X-D functionals combined with ccJ-pVTZ and Huz-IV basis sets. The B3LYP optimized structure of **7** has the C1C13C14C7 torsional angle close to 0^o (D_{2h} symmetry) which agrees with the experimental torsional angle reported by Lyssenko *et al.*,[20] whereas the one obtained from the ωB97X-D functional has a torsional angle of 14.9^o (D_2 symmetry). With the exception of the C1C13C14C7 twist angle, ωB97X-D functional gave structural parameters of **7** that are in better, though only

fair, agreement with the available experimental results than B3LYP. Unlike those of **7**, **15**, and **32**, the average planes of the rings of **16**, **30**, and **31** are not parallel. With the exception of **32**, the C1…C7 interring separation distance is shorter than the sum of van der Waals radii between two stacked carbon atoms, *ca*. 3.4 Å. The C4…C10 interring separation distance of only **7**, **15**, and **16** are shorter than 3.4 Å.

Very accurate values of the chemical shifts and proton-proton coupling constants were determined from the NMR spectra measurements. The study of the temperature effects on the proton chemical shifts indicated that the chemical shifts of the ethano-bridge protons of **16** and **30** decrease when the temperature decreases. With several exceptions, the calculated values of the chemical shifts and coupling constants reproduce the experimental trends. No general conclusion on the performance of the two basis sets can be reached for the proton and carbon chemical shifts. However, the ωB97X-D/ccJ-pVTZ method best estimated the $^{2}J_{HH}$ coupling constants.

The absorption and emission properties of the paracyclophanes are affected by their bridge lengths. The geometry optimizations performed in the first excited state showed that the interring separation distances between the aromatic bridgehead carbon atoms of all the [*m.n*]paracyclophanes in the excited state decrease by *ca.* 0.2 - 0.9 Å compared to the corresponding ground-state geometries. The calculations satisfactorily reproduced the absorption wavelengths. For **7**, six absorption bands exist. The observation of these bands shows that the bands which are forbidden for the high-symmetry structure (D_{2h}) are allowed in the twisted structure (D_2).

In summary, the results obtained from this PhD dissertation indicated that for geometry optimizations of strained molecules, such as paracyclophanes with small bridges, dispersion corrected GGA functionals combined with triple-ζ and quadruple-ζ type basis sets give reasonably satisfactory results. After optimizing the geometries using such methods, the NMR and electronic properties can fairly be determined using hybrid functionals combined with medium-sized basis sets, like triple-ζ type basis sets.

References

(1) Cram, D. J.; Cram, J. M. *Acc. Chem. Res.* **1971**, *4*, 204-213.

(2) Gleiter, R.; Hopf, H. *Modern Cyclophane Chemistry*; Wiley-VCH: Weinheim, 2004.

(3) Hopf, H. In *Strained Hydrocarbons, Beyond van't Hoff and Le Bel Hypothesis, Chapt. 4.2*; Dodziuk, H., Ed.; Wiley-VCH: Weinheim, 2009.

(4) McGlinchey, M. J.; Milosevic , S. *Isr. J. Chem.* **2012**, *52*, 30-40.

(5) Grealis, J. P.; Müller-Bunz, H.; Casey, M.; McGlinchey, M. J. *Tetrahedron Lett.* **2008**, *49*, 1527-1530.

(6) Cannizzaro, S. *Justus Liebigs Annalen der Chemie* **1854**, *90*, 252-254.

(7) Pellegrin, M. M. *Rec. Trav. Chim. Pays-Bas* **1899**, *18*, 457.

(8) Brown, C. J.; Farthing, A. C. *Nature* **1949**, *164*, 915.

(9) Sekine, Y.; Brown, M.; Boekelheide, V. *J. Am. Chem. Soc.* **1979**, *101*, 3126-3127.

(10) Cram, D. J.; Montgomery, C. S.; Knox, G. R. *J. Am. Chem. Soc.* **1966**, *88*, 515-525.

(11) Shieh, C.-F.; McNally, D.; Boyd, R. H. *Tetrahedron* **1969**, *25*, 3653-3665.

(12) Lonsdale, K.; Milledge, H. J.; Rao, K. V. K. *Proc. R. Soc. London A* **1960,**, *255*, 82-100.

(13) Vögtle, F.; Neumann, P. *Stereochemistry II: Topics in Current Chemistry* **1974**, *48*, 67-129.

(14) Bachrach, S. M. *J. Phys. Chem. A* **2011**, *115*, 2396-2401.

(15) Dodziuk, H.; Szymański, S.; Jaźwiński, J.; Marchwiany, M. E.; Hopf, H. *J. Phys. Chem. A* **2010**, *114*, 10467-10473.

(16) Dodziuk, H.; Szymański, S.; Jaźwiński, J.; Ostrowski, M.; Demissie, T. B.; Ruud, K.; Kuś, P.; Hopf, H.; Lin, S.-T. *J. Phys. Chem. A* **2011**, *115*, 10638-10649.

(17) Gantzel, P. K.; Trueblood, K. N. *Acta Cryst. B* **1965**, *18*, 958-968.

(18) Gleiter, R. *Tetrahedron Lett.* **1969**, *10*, 4453-4456.

(19) Hopf, H.; Raulfs, F.-W.; Schomburg, D. *Tetrahedron* **1986**, *42*, 1655-1663.

(20) Lyssenko, K. A.; Antipin, M. Y.; Antonov, D. Y. *ChemPhysChem* **2003**, *4*, 817-823.

(21) Brown, C. J. *J. Chem. Soc.* **1953**, 3265-3270.

(22) Grimme, S. *Chem. Eur. J.* **2004**, *10*, 3423-3429.

(23) Hope, H.; Bernstein, J.; Trueblood, K. N. *Acta Cryst. B* **1972**, *28*, 1733-1743.

(24) Caramori, G. F.; Galembeck, S. E. *J. Phys. Chem. A* **2007**, *111*, 1705-1712.

(25) Grimme, S.; Mück-Lichtenfeld, C. *Isr. J. Chem.* **2012**, *52*, 180-192.

(26) Henseler, D.; Hohlneicher, G. *J. Phys. Chem. A* **1998**, *102*, 10828-10833.

(27) Henseler, D.; Hohlneicher, G. *J. Phys. Chem. A* **1999**, *103*, 1160-1161.

(28) Shirai, S.; Iwata, S.; Maegawa, Y.; Tani, T.; Inagaki, S. *J. Phys.Chem. A* **2012**, *116*, 10194-10202.

(29) Rodgers, D. L.; E. F. Westrum, J.; Andrews, J. T. S. *J. Chem. Thermodynamics* **1973**, *5*, 733-739.

(30) Walden, S. E.; Glatzhofer, D. T. *J. Phys. Chem. A* **1997**, *101*, 8233-8241.

(31) Fuke, K.; Nagakura, S.; Kobayashi, T. *Chem. Phys. Lett.* **1975**, *31*, 205-207.

(32) Dodziuk, H.; Ostrowski, M. *Eur. J. Org. Chem.* **2006**, 5231-5237.

(33) Dodziuk, H.; Ostrowski, M.; Ruud, K.; Jaźwiński, J.; Hopf, H.; Koźmiński, W. *Magn. Reson. Chem.* **2009**, *47*, 407-414.

(34) Bifulco, G.; Mangoni, A. *Magn. Reson. Chem.* **2008**, *46*, 199-201.

(35) Canuto, S.; Zerner, M. C. *J. Am. Chem. Soc.* **1990**, *112*, 2114-2120.

(36) Shen, T. L.; Jackson, J. E.; Yeh, J. H.; Nocera, D. G.; Leroi, G. E. *Chem. Phys. Lett.* **1992**, *191*, 149-156.

(37) Dodziuk, H.; Vetokhina, V.; Hopf, H.; Luboradzki, R.; Gawel, P.; Waluk, J. *J. Chem. Phys.* **2012**, *136*, 074201.

(38) Cram, D. J.; Bauer, R. H. *J. Am. Chem. Soc.* **1959**, *81*, 5971-5977.

(39) Bartholomew, G. P.; Bazan, G. C. *Acc. Chem. Res.* **2001**, *34*, 30-39.

(40) Galindo, F.; Becerril, J.; Burguete, M. I.; Luis, S. V.; Vigara, L. *Tetrahedron Lett.* **2004**, *45*, 1655-1657.

(41) Hopf, H. *Angew. Chem. Int. Ed.* **2008**, *47*, 9808-9812.

(42) Jones, P. G.; Hopf, H.; Pechlivanidis, Z.; Boese, R. *Z. Kristallogr.* **1994**, *209*, 673-676.

(43) Pelter, A.; Mootoo, B.; Maxwell, A.; Reid, A. *Tetrahedron Lett.* **2001**, *42*, 8391-8394.

(44) J. Jones, C. *Chem. Soc. Rev.* **1998**, *27*, 289-300.

(45) Hopf, H. *Tetrahedron* **2008**, *64*, 11504-11516.

(46) Morisaki, Y.; Hifumi, R.; Lin, L.; Inoshita, K.; Chujo, Y. *Polym. Chem.* **2012**, *3*, 2727-2730.

(47) Rajakumar, P.; Padmanabhan, R. *Aust. J. Chem.* **2012**, *65*, 186.

(48) Ettmayer, P.; Billich, A.; Hecht, P.; Rosenwirth, B.; Gstach, H. *J. Med. Chem.,* **1996**, *39*, 3291–3299.

(49) Das, B.; Abe, S. *J. Phys. Chem. B* **2006**, *110*, 23806-23811.

(50) Fürstner, A.; Alcarazo, M.; Krause, H.; Lehmann, C. W. *J. Am. Chem. Soc.* **2007**, *129*, 12676-12677.

(51) Halling, M. D.; Unikela, K. S.; Bodwell, G. J.; Grant, D. M.; Pugmire, R. J. *J. Phys. Chem. A* **2012**, *116*, 5193-5198.

(52) Dodziuk, H.; Demissie, T. B.; Ruud, K.; Szymański, S.; Jaźwiński, J.; Hopf, H. *Magn. Reson. Chem.* **2012**, *50*, 449-457.

(53) Ernst, L. *Prog. Nucl. Magn. Reson. Spectrosc.* **2000**, *37*, 47-190.

(54) Ernst, L. *ChemInform* **2008**, *39*, No. 10.1002/chin.200821278.

(55) Helgaker, T.; Jaszuński, M.; Ruud, K. *Chem. Rev.* **1998**, *99*, 293-352.

(56) Kaupp, M.; Buhl, M.; Malkin, V. G. *Calculation of NMR and EPR Parameters*; John Wiley & Sons, Inc: Weinheim, 2004.

(57) Helgaker, T.; Jaszuński, M.; Pecul, M. *Progress in Nuclear Magnetic Resonance Spectroscopy* **2008**, *53*, 249-268.

(58) McWeeny, R. *Methods of Molecular Quantum Mechanics*; 2nd ed.; Academic Press: New York, 1989.

(59) Szabo, A.; Ostlund, N. S. *Modern Quantum Chemistry:Introduction to Advanced Electronic Structure Theory*; McGraw-Hill New York, 1989

(60) Ramsey, N. F. *Phys. Rev.* **1950**, *78*, 699.

(61) Ramsey, N. F. *Phys. Rev.* **1953**, *91*, 303.

(62) Rusakov, Y. Y.; Krivdin, L. B. *Russ. Chem. Rev.* **2013**, *82* 99-130.

(63) Burke, K. *J. Chem. Phys.* **2012**, *136*, 150901-150909.

(64) Kaduk, B.; Kowalczyk, T.; Van Voorhis, T. *Chem. Rev.* **2011**, *112*, 321-370.

(65) Cohen, A. J.; Mori-Sánchez, P.; Yang, W. *Chem. Rev.* **2011**, *112*, 289-320.

(66) Pyykkö, P.; Stanton, J. F. *Chem. Rev.* **2012**, *112*, 1-3.

(67) Geerlings, P.; De Proft, F.; Langenaeker, W. *Chem. Rev.* **2003**, *103*, 1793-1874.

(68) Lewars G., E. *Computational Chemistry: Introduction to the Theory and Applications of Molecular and Quantum Mechanics*; 2nd ed.; Springer: New York, 2011.

(69) Koch, W.; Holthausen, M. *A chemist's guide to density functional theory*; Wiley-VCH: New York, 2000.

(70) Parr, R. G.; Yang, W. *Density-functional theory of atoms and molecules*; Oxford University Press New York, 1989.

(71) Born, M.; Oppenheimer, R. *Annalen der Physik* **1927**, *389*, 457-484.

(72) Schrödinger, E. *Phys. Rev.* **1926**, *28*, 1049-1070.

(73) Hohenberg, P.; Kohn, W. *Phys. Rev.* **1964**, *136*, B864-B871.

(74) Kohn, W.; Sham, L. J. *Phys. Rev.* **1965**, *140*, A1133-A1138.

(75) Becke, A. D. *Phys. Rev. A* **1988**, *38*, 3098-3100.

(76) Lee, C.; Yang, W.; Parr, R. G. *Phys. Rev. B* **1988**, *57*, 785-789.

(77) Perdew, J. P. *Phys. Rev. B* **1986**, *33*, 8822-8824.

(78) Becke, A. D. *J. Chem. Phys.* **1993**, *98*, 5648-5652.

(79) Stephens, P. J.; Devlin, F. J.; Chabalowski, C. F.; Frisch, M. J. *J. Phys. Chem.* **1994** *98*, 11623-11627.

(80) Runge, E.; Gross, E. K. U. *Phys. Rev. Lett.* **1984**, *52*, 997-1000.

(81) Hohenberg, P.; Kohn, W. *Phys. Rev.* **1964**, *136*, B864-B871.

(82) Gross, E. K. U.; Kohn, W. *Phys. Rev. Lett.* **1985**, *55*, 2850-2852.

(83) Kozłowska, J.; Wielgus, M.; Bartkowiak, W. *Comp. Theor. Chem.* **2013**, *1014*, 49-55.

(84) Burke, K. *J. Chem. Phys.* **2012**, *136*, 150901.

(85) Tempel, D. G.; Watson, M. A.; Olivares-Amaya, R.; Aspuru-Guzik, A. *J. Chem. Phys.* **2011**, *134*, 074116.

(86) Stobbe, M.; Reiser, O.; Nader, R.; Meijere., A. d. *Chem. Ber.* **1987**, *120*, 1667-1674.

(87) Longone, D. T.; Kusefoglu, S. H.; Gladysz, J. A. *J. Org. Chem.* **1977**, *42*, 2787-2788.

(88) Pechlivanidis, Z.; Hopf, H.; Ernst, L. *Eur. J. Org. Chem.* **2009**, 223-237.

(89) Kus, P.; Dalley, N. K.; Kuo, X.; Rogers, R. D.; Bartsch, R. A. *Pol. J. Chem.* **2001**, *75*, 1351-1360.

(90) Cram, D. J.; Dalton, C. K.; Knox, G. R. *J. Am. Chem. Soc.* **1963**, *85*, 1088-1093.

(91) Hopf, H.; Savinsky, R.; Jones, P. G.; J. Dix, B. A. *Liebigs Ann. Recl.* **1997**, 1499-1504.

(92) Aalbersberg, W. G. L.; Vollhardt, K. P. C. *Tetrahedron Lett.* **1979**, *20*, 1939-1942.

(93) Broschinski, K.; Kannan, A.; Jones, P. G.; Dix, I.; Hopf, H. *Act. Cryst. Sec. C* **2007**, *63*, o711-o713.

(94) Truesdale, E. A.; Cram, D. J. *J. Am. Chem. Soc.* **1973**, *95*, 5825-5827.

(95) Jones, P. G.; Pechlivanidis, Z.; Hopf, Z. *Z. Naturforsch.* **1989**, *44b*, 860-862.

(96) Anderson, W. A.; Freeman, R. *J. Chem. Phys.* **1962**, *37*, 85-103.

(97) Martin, G. E.; Zekter, A. S. *Two-Dimensional NMR Methods for Establishing Molecular Connectivity*; VCH Publishers, Inc: New York, 1988.

(98) Bodenhausen, G.; Ruben, D. J. *Chem. Phys. Lett.* **1980**, *69*, 185-189.

(99) Keeler, J. *Understanding NMR Spectroscopy*; John Wiley & Sons: Chichester, 2005.

(100) Geet, A. L. V. *Anal. Chem.* **1970**, *42*, 679-680.

(101) Liouville, J. *J. Math. Pures Appl.* **1838**, *3*, 342-349.

(102) Frisch, M. J. G.; Trucks, W.; Schlegel, H. B.; Scuseria, G. E.; Robb, M. A.; Cheeseman, J. R.; Scalmani, G.; Barone, V.; Mennucci, B. G.; Petersson, A.; Nakatsuji, H.; Caricato, M.; Li, X.; Hratchian, H. P.; Izmaylov, A. F.; Bloino, J.; Zheng, G.; Sonnenberg, J. L.; Hada, M. E., M.; Toyota, K.; Fukuda, R.; Hasegawa, J.; Ishida, M.; Nakajima, T.; Honda, Y.; Kitao, O.; Nakai, H.; Vreven, T.; Montgomery, J. A.; Peralta, J. E.; Ogliaro, F.; Bearpark, M.; Heyd, J. J.; Brothers, E.; Kudin, K. N.; Staroverov, V. N.; Kobayashi, R.; Normand, J.;

Raghavachari, K.; Rendell, A.; Burant, J. C.; Iyengar, S. S.; Tomasi, J.; Cossi, M.; Rega, N.; Millam, J. M.; Klene, M.; Knox, J. E.; Cross, J. B.; Bakken, V.; Adamo, C.; Jaramillo, J.; Gomperts, R.; Stratmann, R. E.; Yazyev, O.; Austin, A. J.; Cammi, R.; Pomelli, C.; Ochterski, J. W.; Martin, R. L.; Morokuma, K.; Zakrzewski, V. G.; Voth, G. A.; Salvador, P.; Dannenberg, J. J.; Dapprich, S.; Daniels, A. D.; Farkas, O.; Foresman, J. B.; Ortiz, J. V.; Cioslowski, J.; Fox, D. J. *Gaussian 09 Revision A.02, Gaussian, Inc., Wallingford CT* **2009**.

(103) Dalton; an ab initio electronic structure program, Release 2.0: 2005, http://daltonprogram.org/.

(104) Dunning, T. H. *J. Chem. Phys.* **1989**, *90*, 1007-1023.

(105) McLean, A. D.; Chandler, G. S. *J. Chem. Phys.* **1980**, *72*, 5639-5648.

(106) Huzinaga, S. *Approximate atomic functions*; University of Alberta: Edmonton, Alberta, Canada, 1971.

(107) Bakken, V.; Helgaker, T. *J. Chem. Phys.* **2002**, *117*, 9160-9174.

(108) Schindler, M.; Kutzelnigg, W. *J. Chem. Phys.* **1982**, *76*, 1919-1933.

(109) London, F. *J. Phys. Radium* **1937**, *8*, 397-409.

(110) Ruud, K.; Helgaker, T.; Kobayashi, R.; Jorgensen, P.; Bak, K. L.; Jensen, H. J. *J. Chem. Phys.* **1994**, *100*, 8178-8185.

(111) Vahtras, O.; Agren, H.; Jorgensen, P.; Jensen, H. J. A.; Padkjaer, S. B.; Helgaker, T. *J. Chem. Phys.* **1992**, *96*, 6120-6125.

(112) Chai, J. D.; Head-Gordon, M. *Phys. Chem. Chem. Phys.* **2008**, *10*, 6615-6620.

(113) Benedikt, U.; Auer, A. A.; Jensen, F. *J. Chem. Phys.* **2008**, *129*, 064111, doi: 064110.061063/064111.2962973.

(114) Yanai, T.; Tew, D.; Handy, N. *Chem. Phys. Lett.* **2004**, *393*, 51-57.

(115) Kendall, R. A.; Dunning, T. H.; Harrison, R. J. *J. Chem. Phys.* **1992**, *96*, 6796-6806.

(116) Bickelhaupt, F. *Pure Appl. Chem.* **1990**, *62*, 373-382.

(117) Dodziuk, H. *Strained Hydrocarbons: Beyond the van't Hoff and Le Bel Hypothesis*; Wiley-VCH Verlag GmbH & Co. KGaA: Weinheim, 2009.

(118) Iwata, S.; Fuke, K.; Sasaki, M.; Nagakura, S.; Otsubo, T.; Misumi, S. *J. Mol. Spectrosc.* **1973**, *46*, 1-15.

(119) Melzer, G.; Schweitzer, D.; Hausser, K. H.; Colpa, J. P.; Haenel, M. W. *Chem. Phys.* **1979**, *39*, 229-235.

(120) Ramm, S. M.; Hopf, H.; Jones, P. G.; Bubenitschek, P.; Ahrens, B.; Ernst, L. *Eur. J. Org. Chem.* **2008**, 2948-2959.

(121) Ron, A.; Noble, M.; Lee, E. K. C. *Chem. Phys.* **1984**, *83*, 215-219.

(122) Ron, A.; Schnepp, O. *J. Chem. Phys.* **1966**, *44*, 19-22.

(123) Singer, L. A.; Cram, D. J. *J. Am. Chem. Soc.* **1963**, *85*, 1080-1084.

(124) de Meijere, A.; Kozhushkov, S. I.; Rauch, K.; Schill, H.; Verevkin, S. P.; Kummerlin, M.; Beckhaus, H.-D.; Ruchardt, C.; Yufit, D. S. *J. Am. Chem. Soc.* **2003**, *125*, 15110-15113.

(125) Nishiyama, K.; Sakiyama, N.; Seki, S.; Horita, H.; Otsubo, T.; Misumi, S. *Bull. Chem. Soc. Jpn.* **1980**, *53*, 869-877.

(126) Pelloni, S.; Lazzeretti, P.; Zanasi, R. *J. Phys. Chem. A* **2007**, *111*, 3110-3123.

(127) In *Citation Cited in Chem. Eur. J.* ***2004****, 10, 3423-3429, but the experimental results by Stalke D. have never been published* .

(128) Demissie, T. B., personal communication with Prof. Hakon Hope about the twist angle of [2.2]paracyclophane published in *Acta Cryst. B* **1972**, 28, 1733.

(129) Roy, D.; Marianski, M.; Maitra, N. T.; Dannenberg, J. J. *J. Chem. Phys.* **2012**, *137*, 134109 (doi.org/134110.131063/134101.4755990)

(130) Perez-Jimenez, A. J.; Sancho-Garcia, J. C.; Perez-Jorda, J. M. *J. Chem. Phys.* **2005**, *123*, 134309 (doi.org/134310.131063/134301.2043107).

(131) He, X.; Fusti-Molnar, L.; Cui, G.; Merz, K. M. *J. Phys. Chem. B* **2009**, *113*, 5290-5300.

(132) Kamya, P. R. N.; Muchall, H. M. *J. Phys. Chem. A* **2008**, *112*, 13691-13698.

(133) Ernst, L. *Annu. Rep. NMR Spectrosc.* **2006**, *60*, 77-143.

(134) Andrews, J. T. S.; Westrum, E. F. *J. Phys. Chem.* **1970**, *74*, 2170-2174.

(135) Schmidbaur, H.; Bublak, W.; Huber, B.; Muller, G. Z. *Naturforsch. B* **1987**, *42*, 147-150.

(136) Fratini, A. V.; Chabinyc, M. L.; Perko, T. J.; Adams, W. W. *Act. Cryst. Sect. C* **1995**, *51*, 904-908.

(137) Ernst, L.; Boekelheide, V.; Hopf, H. *Magn. Reson. Chem.* **1993**, *31*, 669-676.

(138) Karplus, M. *J. Am. Chem. Soc.* **1963**, *85*, 2870-2871.

(139) Haasnoot, C. A. G.; de Leeuw, F. A. A. M.; Altona, C. *Tetrahedron* **1980**, *36*, 2783-2792.

(140) Boekelheide, V.; Hollins, R. A. *J. Am. Chem. Soc.* **1973**, *95*, 3201-3208.

(141) Otsubo, T.; Boekelheide, V. *J. Org. Chem.* **1977**, *42*, 1085-1087.

(142) Otsubo, T.; Boekelheide, V. *Tetrahedron Lett.* **1975**, *16*, 3881-3884.

(143) Mitchell, R. H.; Carruthers, R. J.; Mazuch, L.; Dingle, T. W. *J. Am. Chem. Soc.* **1982**, *104*, 2544-2551.

(144) Hanson, A. W. *Cryst. Struct. Comm.* **1980**, *9*, 1243-1247.

(145) Dewhirst, K.; Cram, D. J. *J. Am. Chem. Soc.* **1958**, *80*, 3115-3125.

(146) Heilbronner, E., Yang, Z.-Z., *Top. Curr. Chem.* **1983**, *115*, 1-55.

(147) Allen, F. H.; Kennard, O.; Watson, D. G.; Brammer, L.; Orpen, A. G.; Taylor, R. *J. Chem. Soc., Perkin Trans. II* **1987**, *0*, S1-S19.

(148) Narten, A. H. *J. Chem. Phys.* **1977**, *67*, 2102-2108.

(149) Mourad, A. F.; Kleinschroth, J.; Hopf, H. *Isr. J. Chem.* **1980**, *20*, 291-293.

(150) Buchholz, H. A.; Höfer, J.; Noltemeyer, M. *Eur. J. Org. Chem.* **1998**, 1763–1770.

(151) Aalbersberg, W. G. L.; Vollhardt, K. P. C. *Tetrahedron Lett.* **1979**, *20*, 1939-1942.

(152) Anet, F. A. L.; Brown, M. A. *J. Am. Chem. Soc.* **1969**, *91*, 2389-2391.

(153) Szymański, S.; Dodziuk, H.; Pietrzak, M.; Jaźwiński, J.; Demissie, T. B.; Hopf, H. *J. Phys. Org. Chem.* **2013**, *26*, 596-600.

(154) Ron, A.; Schnepp, O. *J. Chem. Phys.* **1962**, *37*, 2540-2546.

(155) Thomas, I. R.; Bruno, I. J.; Cole, J. C.; Macrae, C. F.; Pidcock, E.; Wood, P. A. *J. Appl. Cryst.* **2010**, *43*, 362-366.

(156) *Cambridge Structural Database System,* Cambridge: UK, **2003**.

(157) Burdett, J. K. *Chemical Bonding in Solids*; Oxford University Press: New York, **1995**.

(158) Karplus, M. *J. Chem. Phys.* **1959**, *30*, 11-15.

Annex

Supplementary information for this PhD dissertation is provided at the end of the .pdf file (S1-S69) of the online version of the dissertation via www.ichf.edu.pl., and in a CD attached to the hard copy of the dissertation.